UNIVERSITY OF CALIFORNIA
RIVERSIDE

Understanding Surface Chemistry of the $BaTiO_{2.5}H_{0.5}$ Perovskite Oxyhydride from First Principles

A Dissertation submitted in partial satisfaction
of the requirements for the degree of

Doctor of Philosophy

in

Chemistry

by

Kristen Wang Romero

June 2022

Dissertation Committee:
Dr. De-en Jiang, Chairperson
Dr. Gregory Beran
Dr. Ludwig Bartels

The Dissertation of Kristen Wang Romero is approved:

Committee Chairperson

University of California, Riverside

COPYRIGHT ACKNOWLEDGEMENT

ACKNOWLEDGEMENTS

Graduate school was challenging, and I would not be where I am today without the help and encouragement from numerous amazing individuals.

First off, I would like to thank my PhD advisor, Dr. De-en Jiang, for his mentorship, guidance, and support throughout this journey. It certainly helped make my grad school experience more manageable and further instilled confidence in myself that I *can* do this.

Next, I would like to thank Dr. Zili Wu, Dr. Aditya (Ashi) Savara, and Dr. Felipe Polo-Garzon over at Oak Ridge National Laboratory for the valuable feedback and suggestions you all have provided me. I would like to further thank Dr. Savara for all the times you have helped me in understanding microkinetic modeling. I would not have been a more well-rounded scientist without the help from you all.

I would also like to thank my dissertation committee members, Dr. Gregory Beran and Dr. Ludwig Bartels, as well as my qualifying exam committee members, Dr. Matthew Conley and Dr. Sinisia Coh, for the helpful comments and suggestions. I would like to especially thank Dr. Beran for the helpful advice that encouraged me to continue with the graduate program.

I would like to thank Ms. Christina Youhas for always being there for students and for lending an ear when students need it the most. I would like to thank past Jiang group members, Dr. Chad Priest, Dr. Victor Fung, Dr. Lihua (Libby) Xu, Dr. Yangyunli Sun, and Ms. Nicole Feider (M.Sc.) along with my current group members, Tongyu Liu, Yuqing Fu, Chuanye Xiong, Haohong Song, Yujing Tong, Dr. Dhileep Reddy, Hyuna Kwon, Shicheng Li, and Dr. Lu Wang for creating such a welcoming environment at the office and for being

there whenever I had a question about my project. Being in an office with no windows could get depressing sometimes but seeing all of your friendly faces brightens up the room every time.

I would like to thank my friend Ting Ting Wu for all the wonderful conversations we had during lunch. I would like to thank my friend, Nicole Chiang, for listening when I needed someone to vent to and for all the fun times.

I would like to thank all my high school friends, Anny Lee, Chippy Yan, Claire Chin, Junyoung Park, Kathleen Chang, and Sherry Carrington, for reminding me that some things really never change, and for the lasting friendship that still lives on today.

Next, I would like to thank my Momma and Dad for all the support, love, and kind words you have given me since I was a kid. I would like to thank my sister, Kathleen (Jie), for always being my role model since I was little. I would like to thank my brother, Kevin (Kai), for all the shenanigans we have done when we were younger and for being such a nonjudgmental little bro.

I would like to thank my Mom, Pops, and older bro (Todd) for providing me a home away from home especially during a time when I had feelings of not-belonging at Riverside. I'm so thankful and happy to also call you my family.

And last, but not least, I would like to thank the love of my life, Professor Erik Anthony Romero. There are no words in the dictionary that can begin to describe how tremendously thankful I am for you. And so, I have resorted to writing a very short story to show you how much you have helped me in my growth/journey of finding myself.

In the middle of a vast dirt field was one lone yellow sprout peeping out of the surface and it was happy. To the sprout, Earth was home, and it was happy. One day, as the little sprout was gazing over across the gray sky, it noticed what appeared to be gold dust falling from above. The dust jingled like the bells from Christmas carolers. Curious as to what this gold dust was, the little sprout reached its leaves as far out as possible until the very tip touched one of the dust particle's aura. The little sprout's leaves started to transform from a dull yellow to a bright green and as the little sprout reached for more and more gold dust, the gold dust seemed to morph into one large, bright, and yellow pool of happiness. However, the little sprout also noticed that it was growing further and further away from Earth, its home, and it was confused; it was scared. The pool of happiness saw this, and it reached out its hand to the little sprout in a way that looked like a curling ocean wave. It bent the shrubbery and turned over the large leaves of other plants that were shading the little sprout and lifted the sprout higher and higher and higher. The sprout looked to its left and looked to its right and saw the beauty that the pool of happiness saw every day. Although the sprout could no longer see Earth, it could feel that it was still there, and the sprout felt complete.

As cheesy as it may sound, I was completely and utterly lost without you. I just didn't know it yet when I was still trapped in the before time. Thank you for being my sunshine when all I saw was gray. Thank you for showing me all things that are good in life even when life sucked. And most importantly, thank you for pulling me up, when all I could see is down. I thank you today, tomorrow, forever, and always Erik Anthony Romero.

DEDICATION

This thesis is dedicated to my family: my Momma and Dad, Jie and Kai,

my Mom and Pops and my big Bro, Todd. And last, but not least, my Boo.

Thank you all for always believing in me.

ABSTRACT OF THE DISSERTATION

Understanding Surface Chemistry of the $BaTiO_{2.5}H_{0.5}$ Perovskite Oxyhydride from First Principles

by

Kristen Wang Romero

Doctor of Philosophy, Graduate Program in Chemistry
University of California, Riverside, June 2022
Dr. De-en Jiang, Chairperson

With global energy consumption on the rise, it is crucial to design new heterogeneous catalysts that can efficiently produce desired products at a lower energy input. A way to control a catalyst's activity and selectivity is by tuning the local environment around the catalytic active site. The $BaTiO_{3-x}H_x$ perovskite oxyhydride is an example of an anion-tuned ABO_3 perovskite where some lattice O^{2-} are replaced by H^-. The presence of these lattice hydrides in $BaTiO_{3-x}H_x$ not only make the material a more efficient catalyst support for CO_2 methanation and ammonia synthesis than $BaTiO_3$, but $BaTiO_{3-x}H_x$ (with $x = 0.5$) is also active for ammonia synthesis. Hence, in this thesis, we aim to study the surface chemistry of a prototypical perovskite oxyhydride, $BaTiO_{2.5}H_{0.5}$ (BTOH), to understand the role BTOH lattice hydrides play in hydrogenation reactions.

We begin by identifying stable terminations of BTOH surfaces under catalytically relevant conditions from first principles density functional theory (DFT). Our results show that the (010)-Ba_2O_2, (210)-Ti_2O_2, and (211)-Ba_2O_4H surface terminations are the most stable under relevant catalytic conditions.

Next, we employ DFT methods for the mechanistic investigation of ammonia synthesis, acetylene semi-hydrogenation, and selective hydrogenation of crotonaldehyde over stable BTOH terminations. From these studies, we find that the lattice hydrides can: 1) be directly incorporated in the catalytic reaction, and 2) have an influence on the BTOH surface structure to favor the formation of surface vacancies under specific conditions which in turn are beneficial in reaction activity and selectivity. In ammonia synthesis, these vacancies are key in assisting N-N bond cleavage while in the acetylene semi-hydrogenation reaction, they help stabilize the vinyl intermediate. Additionally, surface vacancies offer a site for facile heterolytic H_2 dissociation and in crotonaldehyde selective hydrogenation, the resulting surface hydride and proton that form are found to drive the hydrogenation of crotonaldehyde at the C=O bond rather than at the C=C bond.

Overall, the results presented in this work shed light on the role of BTOH lattice hydrides and vacancies in various hydrogenation reactions and suggest the potential use of BTOH and other perovskite oxyhydride materials as catalysts for general hydrogenation reactions.

Table of Contents

List of Figures

List of Tables

CHAPTER 1
Introduction

With the advancement of technology comes an increase demand in energy. In the year 2018 alone, over 400 quadrillion (400×10^{15}) British thermal units (Btu) of energy were used with 37% of that energy ($\sim 149 \times 10^{15}$ Btu) devoted to industrial sectors such as chemicals, iron and steel, cement, paper, and aluminum.[1] To give an idea of a Btu, the average wattage of a typical microwave found in a household kitchen is around 1000 Watts or 1 kilowatt (kW). If the leftover pizza from last night was heated in the microwave for 1 min, about 0.017 kWh (or 57 Btu) of energy is consumed. Now imagine how long you can heat your pizza up with 400 quadrillion Btu! It is projected an additional ~170 quadrillion Btu of energy is necessary by the year 2050 to keep up with the world's growing energy consumption.[2] As energy is so ubiquitous in our everyday lives, conserving such energy resources is pertinent not only to cut costs but to also limit climate change. There are many different ways to conserve our global energy resources. At the individual household level, many take upon themselves to turn the lights off when they leave a room or use fans instead of air conditioners during a hot summer day. At the industrial level, turning towards more renewable energy resources such as solar, wind, and hydroelectric energy has been on the rise, however, our economy still heavily relies on nonrenewable resources such as oil, natural gas, and coal.[3,4]

Another strategy for energy conservation is to lower the energy input required for chemical reactions to occur by using efficient catalysts. There are many different chemical reactions performed at the industrial scale that are relevant in our everyday lives. For

example, the synthesis of ammonia is an important industrial reaction as ammonia is a precursor to fertilizers and has applications in the pharmaceutical, textile, and explosives industries.[5] Currently, the production of ammonia via the Haber-Bosch process consumes ~1% of global energy output annually.[6] This is due to the large input of energy needed to achieve the harsh conditions (350-525 ^{o}C and 10-30 MPa) necessary for operation with an iron-based catalyst.[6] For this reason, it is highly desirable to design more efficient and active catalysts for this process.

The ideal catalyst for any chemical reaction is a cheap and naturally abundant substance that can completely convert all substrate and selectively produce the desired product under ambient conditions. However, designing such a catalyst is a challenge given the vastness of chemical and material space. Therefore, initial understanding of a material's interaction with reactant, intermediate, and product species of a chemical reaction can ultimately guide researchers to tune a material's reactivity and selectivity to an optimum.

When it comes to choosing a material to investigate for catalytic properties, complex oxides have been of interest in the catalysis community. These materials are composed of at least two metallic elements and have applications in thermal catalysis,[7] electrocatalysis,[8] and photocatalysis.[9] Complex oxides can take on numerous surface configurations due to the different combinations of metal cations and anions that can be exposed. Thus, these materials contain a higher diversity of local chemical environments that can potentially serve as different active sites for chemical reactions and offer greater tunability in surface chemistry for catalysis than binary oxides.

The ABO_3-type perovskite is an example of a tunable complex oxide that is made up of A-cations (i.e., typically alkali, alkaline earth, or rare earth cations), B-cations (i.e., typically transition metal cations), and oxygen anions.[10] Because of its complex composition, the material can be A-cation, B-cation, or anion tuned to achieve a more active and selective catalyst. For example, upon substituting some Pr^{3+} in $PrNiO_3$ for Sr^{2+}, the new A-cation-tuned perovskite, $Pr_{0.95}Sr_{0.05}NiO_3$, is more active in CO oxidation than its parent oxide.[11] This is because when Sr^{2+} is incorporated into the $PrNiO_3$ lattice framework, an oxygen vacancy is generated to compensate the charge difference between Sr^{2+} and Pr^{3+}. As a result, the vacancy is used to activate O_2, leading to facile oxidation of CO to CO_2.

In another case, upon substituting the B-cation in $LaBO_3$ for either Co, Mn, or Fe, the NO oxidation activity increases in the following order: (lowest activity) $LaFeO_3$ < $LaMnO_3$ < $LaCoO_3$ (highest).[12] Highest NO oxidation activity is seen when B = Co because Co is more reducible than Fe and Mn. Therefore, the oxygen vacancy formation energy in $LaCoO_3$ is lower than $LaMnO_3$ or $LaFeO_3$ and a lattice oxygen can be easily incorporated into the catalytic cycle via a Mars van Krevelen mechanism.

Lastly, the catalytic properties of an ABO_3-type perovskite can also be tuned by anion substitution as exemplified by perovskite oxyhydrides ($ABO_{3-x}H_x$). These hydride-reduced ABO_3 perovskites contain lattice hydrides that randomly occupy the oxygen anion sites of the lattice framework.[13-15] What ultimately paved the way to the discovery of an air- and water- stable $BaTiO_{3-x}H_x$ perovskite oxyhydride, the material of focus in this thesis, were discoveries of the following oxyhydrides described below.

The first mixed oxyhydride was discovered in 1982 with the synthesis of LaHO, a highly hygroscopic material that released hydrogen when in contact with ambient moisture.[16] Sometime after, other oxyhydride materials, including $Ba_3(AlO_4)H$[17] and $Ba_{21}Ge_2O_5H_{24}$,[18] were also synthesized. Although this next generation of oxyhydride materials were more stable, extremely reducing conditions were utilized for synthesis. It was not until 2002 when an oxyhydride of $LaSrCoO_4$ (*i.e.*, $LaSrCoO_3H_{0.7}$) could be synthesized upon reacting the perovskite oxide with CaH_2 using a soft chemistry method.[19] The synthesis of $LaSrCoO_3H_{0.7}$ is intriguing as it requires low reaction temperatures, and the layered-perovskite's structure is preserved.

By 2012, the $BaTiO_{3-x}H_x$ perovskite oxyhydride with the $BaTiO_3$ lattice framework was discovered to be air- and water-stable.[13] Ever since, other perovskite oxyhydrides have been synthesized that contain other elements as B-cations such as Sc,[20] V,[21,22] Cr,[23] or Mn.[24] Although the hydride concentration in $BaTiO_{3-x}H_x$ cannot exceed 0.6,[13] the large impact these lattice hydrides have on the oxyhydride's redox properties and electronic structure is what makes these oxyhydride materials so interesting. For example, enhanced CO_2 methanation and ammonia synthesis activity was observed when the $BaTiO_{3-x}H_x$ perovskite oxyhydride was used as a support instead of $BaTiO_3$.[25,26] This improvement in activity was attributed to: (i) the material's labile hydrides providing a spillover pathway for the incoming H_2, thus preventing the Ru metal catalyst from being poisoned; (ii) the participation of lattice hydrides in the catalytic cycle via a hydride-based Mars–van Krevelen (MvK) mechanism; (iii) the transfer of charges to the metal centers, which assists in N_2 activation.[25,26] To researchers' surprise, $BaTiO_{3-x}H_x$ (when $x = 0.5$) is also active for

ammonia synthesis even in the absence of a metal catalyst and at conditions (i.e. 400 ^{o}C, 5 MPa) comparable to the Haber–Bosch conditions over an iron-based catalyst.[27] However, the role of lattice hydrides in hydrogenation reactions, such as ammonia synthesis, over $BaTiO_{2.5}H_{0.5}$ remain unclear.

In this thesis, we will explore the role of $BaTiO_{2.5}H_{0.5}$ (BTOH) lattice hydrides in hydrogenation reactions including ammonia synthesis, acetylene semi-hydrogenation, and crotonaldehyde selective hydrogenation. Because reactions over a heterogeneous catalyst mainly takes place on the catalytic surface, it is therefore crucial to identify stable surface structures of BTOH since a catalyst's activity and selectivity properties is dependent on the surface structure.[28] In our first work, we aimed to identify stable terminations of BTOH that are the most probable to form under the typical reaction conditions of the above hydrogenation reactions. Our results show that of the 47 BTOH terminations belonging to the (100), (010), (210), (011), and (211) facets that were studied, only three were found to be the most stable under relevant catalytic conditions: the (010)-Ba_2O_2, (210)-Ti_2O_2, and (211)-Ba_2O_4H surface terminations.[29]

From here, we employed first principles density functional theory to investigate the mechanism of ammonia synthesis and the role of lattice hydrides on a stable BTOH surface (chapter 4). Under ammonia synthesis conditions, the (210)-Ti_2O_2 surface termination is found to be the most stable.[29] Our mechanistic investigation shows that the lattice hydrides in BTOH can participate in the catalytic reaction and the hydride-vacancy that forms is key for adsorption of the N-containing intermediate and subsequent N-N bond cleavage.[30]

Next, as there have been no studies yet on the utilization of perovskite oxyhydrides for general alkyne semi-hydrogenation, we investigate the role of lattice hydrides in BTOH for acetylene semi-hydrogenation by first principles density functional theory and microkinetic modeling (chapter 5). Although this investigation shows no direct role of lattice hydrides in the catalytic cycle, the presence of lattice hydrides in BTOH favors a surface that exposes vacancies under the given reaction conditions which in turn facilitates in H_2 dissociation and stabilizes the vinyl intermediate.

Finally, to understand the role BTOH lattice hydrides and surface anion vacancies play in general selective hydrogenation of α,β-unsaturated aldehydes, we investigated the selective hydrogenation of crotonaldehyde (CRAL) over BTOH as a probe reaction. Our findings show that surface anion vacancies on the BTOH surface is pertinent for selectively hydrogenating CRAL to crotyl alcohol (CROL) because the vacancies provide an avenue to form a proton and surface hydride from H_2 heterolytic cleavage. The formation of oppositely charged H species is conducive for CROL formation because of the favorable charge interactions between 1) the surface hydride and the nearby carbonyl carbon in CRAL and 2) between the proton and partially negative O atom in CRAL. The charge interactions between the H species and carbon atoms in CRAL's C=C bond are not as favorable and, therefore, butanal formation is not preferred.

The BTOH perovskite oxyhydride is a unique metal oxide material because its surface terminations can expose hydrides or hydride vacancies which have been proposed to partake in hydrogenation reactions. The work presented in this thesis is a starting point to understanding BTOH structure-activity-selectivity relationships for catalysis and lays a

foundation for future studies of surface chemistry and catalysis on the BTOH perovskite oxyhydride itself as well as on BTOH-supported metal catalysts.

References

(1) IEA. Tracking Industry 2020. https://www.iea.org/reports/tracking-industry-2020 (accessed Apr 26, 2022).

(2) EIA. EIA projects nearly 50% increase in world energy usage by 2050, led by growth in Asia. https://www.eia.gov/todayinenergy/detail.php?id=49876 (accessed Apr 26, 2022).

(3) IEA. Key World Energy Statistics 2020. https://www.iea.org/reports/key-world-energy-statistics-2020 (accessed Apr 26, 2022).

(4) EIA. Electricity explained. https://www.eia.gov/energyexplained/electricity/ (accessed Apr 26, 2022).

(5) *Ammonia: zero-carbon fertilizer, fuel and energy store*; DES5711; The Royal Society: 2020.

(6) Morlanés, N.; Almaksoud, W.; Rai, R. K.; Ould-Chikh, S.; Ali, M. M.; Vidjayacoumar, B.; Al-Sabban, B. E.; Albahily, K.; Basset, J. M. Development of catalysts for ammonia synthesis based on metal phthalocyanine materials. *Catal. Sci. Technol.* **2020**, 10, 844-852.

(7) Grant, J. T.; Venegas, J. M.; McDermott, W. P.; Hermans, I. Aerobic oxidations of light alkanes over solid metal oxide catalysts. *Chem. Rev.*, **2018**, 118, 2769–2815.

(8) Hwang, J.; Rao, R. R.; Giordano, L.; Katayama, Y.; Yu, Y.; Shao-Horn, Y. Perovskites in catalysis and electrocatalysis. *Science*, **2017**, 358, 751–756.

(9) Chen, S.; Takata, T.; Domen, K. Particulate photocatalysts for overall water splitting. *Nat. Rev. Mater*., **2017**, 2, 17050.

(10) Voorhoeve, R. J. H.; Remeika, J. P.; Trimble, L. E. Defect chemistry and catalysis in oxidation and reduction over perovskite-type oxides. *Ann. N.Y. Acad. Sci.* **1976**, 272, 3-21.

(11) Falcón, H.; Martínez-Lope, M. J.; Alonso, J. A.; Fierro, J. L. G. Large enhancement of the catalytic activity for CO oxidation on hole doped (Ln, Sr)NiO_3 (Ln=Pr, Sm, Eu) Perovskites. *Solid State Ion.* **2000**, 237-248.

(12) Chen, J.; Shen, M.; Wang, X.; Wang, J.; Su, Y.; Zhao, Z. Catalytic performance of NO oxidation over $LaMeO_3$ (Me = Mn, Fe, Co) perovskite prepared by the sol-gel method. *Catal. Commun.* **2013**, 105-108.

(13) Kobayashi, Y.; Hernandez, O. J.; Sakaguchi, T.; Yajima, T.; Roisnel, T.; Tsujimoto, Y.; Morita, M.; Noda, Y.; Mogami, Y.; Kitada, A.; Ohkura, M.; Hosokawa, S.; Li, Z.; Hayashi, K.; Kusano, Y.; Kim, J.; Tsuji, N.; Fujiwara, A.; Matsushita, Y.; Yoshimura, K.; Takegoshi, K.; Inoue, M.; Takano, M.; Kageyama, H. An oxyhydride of $BaTiO_3$ exhibiting hydride exchange and electronic conductivity. *Nat. Mater.*, **2012**, 11, 507–511.

(14) Tang, Y.; Kobayashi, Y.; Shitara, K.; Konishi, A.; Kuwabara, A.; Nakashima, T.; Tassel, C.; Yamamoto, T.; Kageyama, H. On hydride diffusion in transition metal perovskite oxyhydrides investigated via deuterium exchange. *Chem. Mater.*, **2017**, 29, 8187–8194.
(15) Sakaguchi, T.; Kobayashi, Y.; Yajima, T.; Ohkura, M.; Tassel, C.; Takeiri, F.; Mitsuoka, S.; Ohkubo, H.; Yamamoto, T.; Kim, J.; Tsuji, N.; Fujihara, A.; Matsushita, Y.; Hester, J.; Avdeev, M.; Ohoyama, K.; Kageyama, H. Oxyhydrides of (Ca, Sr, Ba)TiO_3 Perovskite Solid Solutions. *Inorg. Chem.*, **2012**, 51, 11371–11376.
(16) Brice, J. F.; Moreau, A. Synthese et conductivite anionique des hydruro-oxydes de lanthane de formule LaHO, $LaH_{1+2x}O_{1-x}$ et $LaH_{1+y}O_{1-x}$ (y < 2SC). *Ann. Chim.*, **1982**, 7, 623–634.
(17) Huang, B.; Corbett, J. D. Ba_3AlO_4H: synthesis and structure of a new hydrogen-stabilized phase. *J. Solid State Chem.*, **1998**, 141, 570–575.
(18) Huang, B.; Corbett, J. D. $Ba_{21}Ge_2O_5H_{24}$ and Related Phases. A Corrected Structure Type and Composition for a Zintl Phase Stabilized by Hydrogen. *Inorg. Chem.*, **1998**, 37, 1892–1899.
(19) Hayward, M. A.; Cussen, E. J.; Claridge, J. B.; Bieringer, M.; Rosseinsky, M. J.; Kiely, C. J.; Blundell, S. J.; Marshall, I. M.; Pratt, F. L. The Hydride Anion in an Extended Transition Metal Oxide Array: $LaSrCoO_3H_{0.7}$. *Science*, **2002**, 295, 1882–1884.
(20) Goto, Y.; Tassel, C.; Noda, Y.; Hernandez, O.; Pickard, C. J.; Green, M. A.; Sakaebe, H.; Taguchi, N.; Uchimoto, Y.; Kobayashi, Y.; Kageyama, H. Pressure-Stabilized Cubic Perovskite Oxyhydride $BaScO_2H$. *Inorg. Chem.*, **2017**, 56, 4840–4845.
(21) Bang, J.; Matsuishi, S.; Hiraka, H.; Fujisaki, F.; Otomo, T.; Maki, S.; Yamaura, J.; Kumai, R.; Murakami, Y.; Hosono, H. Hydrogen Ordering and New Polymorph of Layered Perovskite Oxyhydrides: $Sr_2VO_{4-x}H_x$. *J. Am. Chem. Soc.*, **2014**, 136, 7221–7224.
(22) Romero, F. D.; Leach, A.; Möller, J. S.; Foronda, F.; Blundell, S. J.; Hayward, M. A. Strontium Vanadium Oxide-Hydrides: "Square-Planar" Two-Electron Phases. *Angew. Chem., Int. Ed.*, **2014**, 53, 7556–7559.
(23) Tassel, C.; Goto, Y.; Kuno, Y.; Hester, J.; Green, M.; Kobayashi, Y.; Kageyama, H. Direct synthesis of chromium perovskite oxyhydride with a high magnetic-transition temperature. *Angew. Chem.*, **2014**, 126, 10545–10548.
(24) Tassel, C.; Goto, Y.; Watabe, D.; Tang, Y.; Lu, H.; Kuno, Y.; Takeiri, F.; Yamamoto, T.; Brown, C. M.; Hester, J.; Kobayashi, Y.; Kageyama, H. High-pressure synthesis of manganese oxyhydride with partial anion order. *Angew. Chem., Int. Ed.*, **2016**, 55, 9667–9670.
(25) Tang, Y.; Kobayashi, Y.; Tassel, C.; Yamamoto, T.; Kageyama, H. Hydride-Enhanced CO_2 Methanation: Water-Stable $BaTiO_{2.4}H_{0.6}$ as a New Support. *Adv. Energy Mater.*, **2018**, 8, 1800800.
(26) Tang, Y.; Kobayashi, Y.; Masuda, N.; Uchida, Y.; Okamoto, H.; Kageyama, T.; Hosokawa, S.; Loyer, F.; Mitsuhara, K.;Yamanaka, K.; Tamenori, Y.; Tassel, C.;

Yamamoto, T.; Tanaka, T.; Kageyama, H. Metal-Dependent Support Effects of Oxyhydride-Supported Ru, Fe, Co Catalysts for Ammonia Synthesis. *Adv. Energy Mater.*, **2018**, 8, 1801772

(27) Kobayashi, Y.; Tang, Y.; Kageyama, T.; Yamashita, H.; Masuda, N.; Hosokawa, S.; Kageyama, H. Titanium-Based Hydrides as Heterogeneous Catalysts for Ammonia Synthesis. *J. Am. Chem. Soc.* **2017**, 139, 18240-18246.

(28) Chee, Z. W.; Arce-Ramos, J. M.; Li, W.; Genest, A.; Mirsaidov, U. Structural changes in noble metal nanoparticles during CO oxidation and their impact on catalyst activity. *Nat. Commun.* **2020**, 11, 2133.

(29) Wang, K.; Fung, V.; Wu, Z.; Jiang, D.-E. Stable Surface Terminations of a Perovskite Oxyhydride from First-Principles. *J. Phys. Chem. C*, **2020**, 124, 18557–18563.

(30) Wang, K.; Wu, Z.; Jiang, D.-E. Ammonia synthesis on $BaTiO_{2.5}H_{0.5}$:computational insights into the role of hydrides. *Phys. Chem. Chem. Phys.* **2022**, 24, 1496-1502.

CHAPTER 2
Computational Methods

The goal of computational chemistry is to predict the structure, energy, and properties of systems from quantum mechanics. The equation that serves as the key to unlocking such information is the Schrödinger equation. However, solving this equation is not so simple. In this chapter, we review what the Schrödinger equation is, and the methods used to approximate the solutions to this equation. We then discuss methods for transition state search, chemical bond analysis, and microkinetic modeling as approaches to study reaction mechanisms and rates on a heterogeneous catalytic surface.

2.1 The Schrödinger equation

Because atoms and their constituting electrons and nuclei obey laws governed by classical and quantum mechanics, we can use computational methods to predict material properties and behavior. A first principles (or *ab initio*) approach is an example of a computational method based on quantum mechanics and, therefore, excludes the use of empirical parameters. This approach is commonly used to study surface chemistry by capturing bond formation and breaking between a surface and reactant molecules.

Any information about a system can be determined by solving, in our case, the time-independent Schrödinger wave equation:

$$\hat{H}\psi(\vec{r},\vec{R}) = E\psi(\vec{r},\vec{R}) \tag{2.1}$$

where $\hat{H}$ is the Hamiltonian operator, $\psi(\vec{r},\vec{R})$ and E are the wavefunction and the total energy of the system, and $\vec{r}$ and $\vec{R}$ represent the system's electron and nuclei positions,

respectively. Since the wavefunction of a system has 3N dimensions, N being the number of electrons, finding an exact solution for the Schrödinger equation becomes exponentially more difficult to obtain as the number of electrons in a system exceed 1. Thus, approximations such as the Born-Oppenheimer (BO) approximation,[1] have been adopted to find numerical solutions to the wave equation. In the BO approximation, the electronic and nuclear components of the equation can be decoupled since nuclear motion is several orders of magnitude slower than electronic motion. Thus, the electronic structure of a system can be calculated from only the electronic components as so:

$$\hat{H}_{el}\psi_{el}(\vec{r},\vec{R}) = E_{el}\psi_{el}(\vec{r},\vec{R}) \tag{2.2}$$

where $\hat{H}_{el}$, $\psi_{el}(\vec{r},\vec{R})$, and E_{el} are the electronic Hamiltonian, wavefunctions, and energy, respectively.

There are two types of approaches to solving this simplified wave equation:[2] the wave function theory (WFT) and density functional theory (DFT). The most common WFT approximation method is Hartree-Fock (HF) theory which assumes that each electron in a system moves in an average or mean field of all other electrons and nuclei and that the many-electron wavefunction has the form of a determinant of single-electron wavefunctions called a Slater determinant.[3] Slater determinants can approximately describe an antisymmetric wavefunction of a multi-electron atom but neglects electron correlation because of the mean field approximation. Therefore, to account for electron correlation, a post Hartree-Fock method called configuration interaction can be used.[4] In this method, different orbital configurations (i.e., putting electrons in different orbitals) can be described by different Slater determinants and a linear combination of these Slater

determinants can better describe the spatial correlations in electron motion. However, HF theory and configuration interaction is only practical in small systems with tens of atoms and, thus, would not be an appropriate method for material systems. To combat this issue, the DFT method can be used instead as described in the next section.

2.2 Density Functional Theory (DFT)

An alternative to the wave function methods of solving the Schrödinger equation is density functional theory (DFT).[5] Because the dimensionality of a problem increases with the number of electrons in the system, it is therefore more advantageous to use electron density rather than individual electrons as in the case of HF. In pure DFT, the method attempts to compute the energy of interacting electrons as a functional of the density. However, finding accurate approximations for the kinetic energy functional is a challenge. Therefore, instead of finding a kinetic energy functional of an interacting system, the Kohn-Sham approach was used to find a fictitious system of non-interacting electrons with the same electron density as the actual system with interacting electrons. Thus, what used to be a n-electron system can now be decomposed into n one-electron systems and the Kohn-Sham equations, rather than the many-body Schrödinger equation, can be solved:

$$\hat{H}_{KS}\varphi_i(\vec{r}) = \varepsilon_i\varphi_i(\vec{r}) \tag{2.3}$$

Here, $\hat{H}_{KS}$ is the Kohn-Sham (KS) Hamiltonian, $\varphi_i(\vec{r})$ is the KS orbital of the fictitious system with energy ε_i. The KS orbitals are the solutions to the KS equations. Once solved, we can determine the ground state electron density of the actual system and, therefore, other quantities of interest. The total energy of a system can then be calculated as $E_{total} = E_{kin(non)} + E_{nuc\text{-}el} + E_{el\text{-}el} + E_{nuc\text{-}nuc} + E_{XC}$ where $E_{kin(non)}$ is the noninteracting kinetic energy,

$E_{nuc\text{-}el}$ is the energy from nuclear-electron interactions, $E_{el\text{-}el}$ is the energy from electron-electron repulsion, $E_{nuc\text{-}nuc}$ is the energy from nuclear-nuclear repulsion, and E_{XC} is the sum term of all interacting energies including the interacting kinetic energy, electron correlation energy, and electron exchange energy.[6] The first three terms are relatively easy to calculate while the $E_{nuc\text{-}nuc}$ term is a constant. Even though the remaining E_{XC} term makes up only a relatively small portion of the overall energy, it is actively involved in phenomena occurring at the atomic, molecular, or material level. Hence, the accuracy of DFT improves when the appropriate XC functional is used to describe E_{XC} of a system.

2.2.1 DFT functionals. There are many different types of functionals with varying accuracy and computational costs. The three most popular groups of functionals are the local density approximation (LDA), generalized gradient approximation (GGA), and hybrids.[7] The LDA functional is of the lowest level and only includes local information about electron density and its gradient at a given point. It can realistically describe the properties for simple metals with slow-varying charge densities at a low computational cost. However, it overestimates the binding energies of molecules and solids and, therefore, is not accurate enough to describe energetics of chemical reactions (i.e., heats of reaction and activation energy barriers).[8,9] On the other hand, the GGA functionals includes both the local and semi-local information about the electron density and its gradient at a given point and are typically more accurate than LDA. These functionals give more accurate binding energies of molecules and solids and improves the calculated energy barriers at a reasonable computational cost.[10] Although the GGA-level functionals over corrects bond length, resulting in under-estimated adsorption energies, it is a sufficient functional for the

work presented in this thesis.[5] There are many different flavors of GGA functionals including PW91[11] and BLYP.[12,13] But the most popular one is the Perdew-Burke-Ernzerhof (PBE) functional which was used in all DFT calculations performed in this work.[14] Lastly, the hybrid functionals are a mixture of exact (or Hartree-Fock) exchange with GGA and can more accurately calculate the true total energy of a system.[15] However, the computational cost is too high for the purposes of this work.

2.2.2 Pseudopotentials. Recall that in DFT, the KS orbitals are solutions to the KS equations and correspond to the noninteracting electrons of a fictitious system. The DFT method can be an "all-electron" approach in which all electrons of each atom are included in the calculation, however, doing so would be computationally costly. As the chemistry of a solid typically involves only valence electrons, the core electrons can essentially be "removed" and replaced with an effective potential that mimics the impact the core electrons have on the valence electrons.[16] Thus, a smaller set of functions (i.e., a basis set) can be used to represent the valence electrons. The main types of pseudopotentials are the norm-conserving,[17] ultrasoft,[18] and projector-augmented wave (PAW) pseudopotentials.[19] All DFT calculations in our work were performed using the Vienna *ab initio* Simulation Package (VASP) code[20,21] which implements the PAW potentials to describe the electron-core interactions. These potentials are constructed using an atomic orbital basis set to describe the core electrons and a planewaves basis set, giving this hybrid potential a higher accuracy than ultra-soft pseudopotentials.[19]

2.2.3 Periodic DFT and Bloch's theorem. Computational cost grows steeply with system size. Therefore, to treat bulk periodic systems like crystals, it would be

advantageous to model the system as a unit cell with periodic boundary conditions. The unit cell can then be mapped into a reciprocal space, or a k-space made up of k-points. Because the system is periodic, it would make sense that the wavefunction for the system would also be periodic and, hence, Bloch's theorem states that:[5]

$$\psi_k(\vec{r}) = u_k(\vec{r})\exp(ik \cdot \vec{r}) \tag{2.4}$$

where $\psi_k(\vec{r})$ is the wavefunction of an electron, k are the k-points in reciprocal space, and $u_k(\vec{r})$ is a periodic function that has the same periodicity as the potential such that $u_k(\vec{r}) = u_k(\vec{r}+\vec{R})$. As a result, Bloch's theorem greatly simplifies the problem of calculating the wavefunctions of electrons in an infinite system to a finite one.

2.2.4 Dispersion corrections. The exchange-correlation term, E_{XC}, of DFT calculations is assumed to be a functional of the local electron density. As a result, only local contributions to the electron correlation are included and long-range dispersion forces are neglected.[22] A nonempirical approach to correcting these errors is by the vdW-DF method which computes a system's dispersion energy based on its electron density.[23] Other approaches include the DFT+D method by Grimme et al. which is an empirical method, typically cheaper than using the vdW-DF methods, that describes dispersive energy by damped interatomic potentials.[24] The DFT-D3, Grimme's third generation DFT dispersion correction with Becke-Johnson damping, was used in this work.

2.3 Transition state search

On a potential energy surface (PES), the local minima represent reactants, products, and intermediate states while the saddle points bridging between two local minima represent transition states along a minimum-energy path (MEP). Finding these transition states are

crucial in catalytic studies as it provides information on reaction mechanisms and rates. Typically, a Hessian matrix of second derivatives of potential energy can be used to determine if a point along the PES is a transition state. However, as this can become computationally expensive, a number of approaches have been developed to find transition states based on calculating the first derivatives, or the forces, instead. The two methods used in this thesis are the nudged elastic band (NEB) and dimer methods as described below.

2.3.1 Nudged elastic band. In the nudged elastic band (NEB) method, two local minima on a PES (or the initial and final states in a chemical reaction) are connected to each other by a straight band.[25] Intermediate configurations between the initial and final states are represented by evenly spaced points or images that lie on the band. To search for the MEP between the initial and final states, this band will be nudged towards a path until the fictitious spring force applied to each image and parallel to the band is minimized. The climbing image-NEB can be used to ensure that the highest energy image climbs to a saddle point.[26] When running NEB calculations, there are some important points to consider:

1) Ensure that there are no additional local minima along the path between the initial and final states. If there is, the path is more complicated than anticipated and the NEB needs to be restarted.
2) A goldilocks number of images between the initial and final states must be chosen for a sufficient resolution to find the saddle point at a reasonable computational cost.
3) The transition state found is based on the initial and final states decided by the user. To prevent user bias, it is important to test different initial and final states to find the most reasonable path.

2.3.2 Dimer. Unlike the NEB method where initial and final states are used as inputs to find the transition state, the dimer method can be used to find the nearest saddle point from any initial configuration.[27,28] Although, this method works best when a good guess of the transition state, found from a crude NEB run, is used. In the dimer method, two images, or the dimer, are first generated at an equal distant from an initial input geometry. In each optimization cycle, the dimer energy is minimized by rotating about its center to find the lowest curvature mode. The dimer converges towards a saddle point by climbing up the PES along the lowest curvature mode direction while relaxing in all perpendicular directions.[29] The advantage of using the dimer method is that it theoretically has a lower computational cost than NEB because only two images are needed instead of multiple. However, without a set initial and final state as endpoints, the dimer can diverge to another saddle point that is different than anticipated. Hence in this work, the dimer method is only used to refine crude transition state configurations rather than finding transition states.

2.4 Chemical bonding analysis

Understanding the chemical bonding interaction between molecules and a catalytic surface can explain why certain chemical processes, such as adsorption and hydrogenation, occur. In this work, chemical bonding analyses (i.e., density of states and Bader Charge analysis) are used to identify preferential adsorption sites on a catalytic surface and provide insight on the driving force of a reaction.

2.4.1 Density of states. To explain the density of states (DOS) of a solid, it is best to review a simpler case: the atom. An atom contains different energy levels with each

energy level made up of different subshells/orbitals and each orbital holding a maximum of two electrons. When two or more atoms combine, their atomic orbitals also combine to form the molecular orbitals of a molecule. Like atomic orbitals, molecular orbitals also have discrete energy levels and can explain the geometric structure of molecules. A solid can be thought of as a very large molecule containing many atoms on the order of Avogadro's number.[30] Because of the sheer number of atoms in a solid, there is also a sheer number of "molecular orbitals" such that its orbitals can be drawn as a band rather than lines at each discrete energy level. The DOS of a solid is then defined as the number of states or energy levels per unit of energy. In this thesis, DOS was used to understand the interaction between adsorbates and the catalytic surface. This interaction can be seen by the overlapping molecular and surface DOS with a greater overlap indicating a stronger interaction.

2.4.2 Bader charge analysis. Charge transfer between atoms can typically be used to explain the properties of chemicals and materials. The most common method of determining atomic charges from theoretical calculations is the Mulliken population analysis.[31] In this method, after atomic orbital basis sets are used to calculate the electronic wavefunction of the system, the calculated charges obtained are assigned to the atoms in which the basis functions are centered upon. While this method is a fast and useful way in determining partial atomic charges, it has a couple of disadvantages:

1) it's sensitive to the choice of basis set and
2) it's unsuitable for solid-state studies since the plane wave basis set, which functions are not centered on any atom, are used.

Another approach is to divide the charge density amongst atoms at the point where charge density reaches a minimum between atoms. In other words, the Bader charge of an atom is bounded by zero flux surfaces in which charge density is a minimum perpendicular to the surface.[32] Because Bader charge analysis can be used to analyze calculations based on plane wave or atomic basis functions, this is generally a good approach to determine atomic charges of systems.

2.5 Microkinetic modeling

2.5.1 Introduction. To improve on a catalyst's activity and selectivity, it is helpful to know the crucial reaction intermediates and rate-controlling elementary steps. For example, if microkinetic simulations show that a certain intermediate is poisoning the surface of a catalyst, the new and improved catalyst would be designed to prevent the formation of the intermediate. The typical steps necessary for the construction of a microkinetic model of a reaction are as follows:[33]

1) Construct a set of elementary reaction steps
2) Derive rate expressions for each elementary reaction steps
3) Convert the set of rate expressions into a set of ordinary differential equations (ODE)
4) Define any initial values, boundary conditions, and model parameters (ex. initial surface concentrations, partial pressures, temperature)
5) Solve the system of ODEs
6) Interpret results (typical output may include reagent orders, apparent activation energy, surface coverage, degree of rate control, production rate)

2.5.2 Microkinetic Modeling using MKMCXX code. The microkinetic simulations described in this thesis were performed using the MKMCXX[34] code to gain information on the microkinetic[35,36,37] properties for, specifically, the acetylene semi-hydrogenation over a BTOH surface. The reaction rate, rate-controlling step(s), surface coverage and selectivity analysis were investigated to understand BTOH selectivity for ethylene. For surface reactions, the pre-exponential factor is mainly dependent on the k_bT/h term such that the forward and reverse rate constants are calculated according to the equation $k = \frac{k_bT}{h}\exp\left(\frac{-\Delta E_{act}^{ZPE}}{k_bT}\right)$ where k_b is the Boltzmann constant, T is temperature, h is the Planck's constant, and ΔE_{act}^{ZPE} is the ZPE corrected enthalpy difference between the transition state and the initial or final state.

For adsorption reactions, processes are treated as non-activated with the rate constants and rates per site expressed as $k_{ads} = \frac{S}{\sqrt{2\pi m k_bT}} / \sigma_s$ and $r_{ads} = Pk_{ads}(1-\theta)$, where P is the gas pressure (typically in bar), σ_s is the site density (typically in sites per m^2), m is the mass of the molecule (typically in kg), S is the sticking coefficient which has a default value of 1, and θ is the total relative coverage for that site type. S was assumed to be 1 for all adsorption reactions. Each adsorption site surface area, A, was approximated to be 1.41×10^{-19} m^2 which equates to one eighth of the 2×2 BTOH supercell of dimensions 9.87 Å × 11.40 Å. Using the relationship $K_{eq} = k_{ads}/k_{des}$, the rate constant for desorption (k_{des}) can then be described as[38]

$$k_{des} = \frac{k_{ads}}{K_{eq}^{\circ}} * \frac{1/\theta^{\circ}}{(1/(1-\theta^{\circ}))(1/P^{\circ})} = \frac{1-\theta^{\circ}}{\theta^{\circ}}\left(\frac{AP^{\circ}}{\sqrt{2\pi m k_bT}}S\right)\frac{\exp\left(\frac{Sgas^{\circ}}{R}\right)}{q_{ads}}\exp\left(\frac{\Delta H_{ads}{}^{\circ} - H_{gas}^{\circ\,298.15\rightarrow T}}{RT}\right),$$

where S_{gas}° and $H_{gas}^{\circ\,298.15\rightarrow T}$ were calculated from thermodynamic tables[39] using the Shomate equation.[40] The standard states used were as described previously such that the surface standard states cancel in the above expression.[41] The total partition function of an adsorbed reactant molecule (q_{ads}) is a product of each of the individual partition functions from electronic, vibrational, rotational, and translational motion such that $q_{ads} = q_{el}q_{vib}q_{rot}q_{trans}$, where q_{el} is often assumed to be 1. As adsorbates have hindered translational and rotational motions parallel to the surface, hindered motion equations[42] are used to approximate for q_{rot} and q_{trans} in this work while q_{vib} was calculated according to the equation $q_{vib} = \prod_i \frac{1}{1-\exp\left(-\frac{\varepsilon_i}{k_b T}\right)}$.

The degree at which an elementary step controls the overall rate of the reaction is analyzed by the degree of rate control (DRC) method.[43,44] For elementary step *i*, the DRC ($X_{RC,i}$) is calculated accordingly $X_{RC,i} = \frac{k_i}{r}\left(\frac{\partial r}{\partial k_i}\right)_{k_{j\neq i},K_i} = \left(\frac{\partial lnr}{\partial lnk_i}\right)_{k_{j\neq i},K_i}$, where k_i, K_i, and r are the forward rate constant and the equilibrium constant for elementary step *i*, and the reaction rate, respectively. Additionally, the DRCs obey the following sum rule $\sum_i X_{RC,i} = 1$.

2.6 References

(1) Born, M.; Oppenheimer, R. Zur Quantentheorie Der Molekeln. *Annalen der Physik* **1927**, 389, 457–484.

(2) Ghosh, S.; Verma, P.; Cramer, C. J.; Gagliardi, L.; Truhlar, D. G. Combining Wave Function Methods with Density Functional Theory for Excited States. *Chem. Rev.* **2018**, 118, 7249–7292.

(3) Nesbet, R. K. Configuration interaction in orbital theories. *Proc. R. Soc. Lond. A* **1955**, 230, 312-321.

(4) Cramer, C. J. *Essentials of Computational Chemistry*; John Wiley & Sons, Ltd.: Chichester, 2004; pp. 191–232.
(5) Lee, J. G. *Computational Materials Science: an Introduction*; CRC Press, Taylor & Francis: Boca Raton, 2017; pp. 131-173.
(6) Burke, K. Perspective on density functional theory. *J. Chem. Phys.* **2012**, 136, 150901.
(7) Rappoport, D.; Crawford, N. R. M.; Furche, F.; Burke, K. Approximate Density Functionals: Which Should I Choose? In *Encyclopedia of Inorganic Chemistry*, 2009 DOI: 10.1002/ 0470862106.ia615.
(8) Koch, W.; Holthausen, M. C. *A Chemist's Guide to Density Functional Theory*; Wiley: Weinheim, 2001.
(9) Gautier, S.; Steinmann, S. N.; Michel, C.; Fleurat-Lessard, P.; Sautet, P. Molecular adsorption at Pt(111). How accurate are DFT functionals? *Phys. Chem. Chem. Phys.* **2015**, 17, 28921.
(10) Mardirossian, N.; Head-Gordon, M. Thirty years of density functional theory in computational chemistry: an overview and extensive assessment of 200 density functionals. *Mol. Phys.* **2017**, 115, 2315-2372.
(11) Perdew, J. P.; Burke, K.; Wang, Y. Generalized gradient approximation for the exchange-correlation hole of a many-electron system. *Phys. Rev. B* **1996**, 57, 16533-16539.
(12) Becke, A. D. Density-functional exchange-energy approximation with correct asymptotic behavior. *Phys. Rev. A* **1988**, 38, 3098-3100.
(13) Lee, C.; Yang, W.; Parr, R. G. Development of the Colle-Salvetti correlation-energy formula into a functional of the electron density. *Phys. Rev. B* **1988**, 37, 785-789.
(14) Perdew, J. P.; Burke, K.; Ernzerhof, M. Generalized Gradient Approximation Made Simple. *Phys. Rev. Lett.* **1996**, 77, 3865-3868.
(15) Fritsch, D. Self-consistent Hybrid Functionals: What We've Learned So Far. In *Theory and Simulation in Physics for Materials Applications*, 2020 DOI: 10.1007/978-3-030-37790-8_5.
(16) Giustino, F. *Materials Modelling using Density Functional Theory*; Oxford University Press: Oxford, 2014; pp. 258-263.
(17) Ramer, N. J.; Rappe, A. M. Designed nonlocal pseudopotentials for enhanced transferability. *Phys. Rev. B* **1999**, 59, 12471-12478
(18) Vanderbilt, D. Soft self-consistent pseudopotentials in a generalized eigenvalue formalism. *Phys. Rev. B* **1990**, 41, 7892-7895.
(19) Blöchl, P. E. Projector augmented-wave method. *Phys. Rev. B: Condens. Matter Mater. Phys.*, **1994**, 50, 17953–17979.
(20) Kresse, G.; Furthmüller, J. Efficiency of ab-initio total energy calculations for metals and semiconductors using a plane-wave basis set. *Comput. Mater. Sci.*, **1996**, 6, 15-50.
(21) Kresse, G.; Furthmüller, J. Efficient iterative schemes for *ab initio* total-energy calculations using a plane-wave basis set. *Phys. Rev. B* **1996**, 54, 11169-11186.
(22) Foster, M. E.; Sohlberg, K. Empirically corrected DFT and semi-empirical methods for non-bonding interactions. *Phys. Chem. Chem. Phys.* **2010**, 12, 307-322.

(23) Dion, M.; Rydberg, H.; Schröder, E.; Langreth, D. C.; Lundqvist, B. I. Van der Waals Density Functional for General Geometries. *Phys. Rev. Lett.* **2004**, 92, 246401.
(24) Grimme, S.; Antony, J.; Ehrlich, S.; Krieg, H. A Consistent and Accurate ab Initio Parametrization of Density Functional Dispersion Correction (DFT-D) for the 94 Elements H-Pu. *J. Chem. Phys.* **2010**, 132, 154104.
(25) Henkelman, G.; Jónsson, H. Improved tangent estimate in the nudged elastic band method for finding minimum energy paths and saddle points. *J. Chem. Phys.* **2000**, 113, 9978-9985.
(26) Henkelman, G.; Uberuaga, B. P.; Jónsson, H. A climbing image nudged elastic band method for finding saddle points and minimum energy paths. *J. Chem. Phys.* **2000**, 113, 9901-9904.
(27) Henkelman, G.; Jónsson, H. A dimer method for finding saddle points on high dimensional potential surfaces using only first derivatives. *J. Chem. Phys.* **1999**, 111, 7010-7022.
(28) Henkelman, G.; Jóhannesson, G.; Jónsson, H. Methods for Finding Saddle Points and Minimum Energy Paths. In *Theoretical Methods in Condensed Phase Chemistry*, 2002 DOI: 10.1007/0-306-46949-9_10.
(29) Xiao, P.; Sheppard, D.; Rogal, J.; Henkelman, G. Solid-state dimer method for calculating solid-solid phase transitions. *J. Chem. Phys.* **2014**, 140, 174104.
(30) Hoffmann, R. *Solids and Surfaces: A Chemist's View of Bonding in Extended Structures*; VCH Publishers, Inc.: New York, 1988; pp. 26-32.
(31) Henkelman, G.; Arnaldsson, A. ; Jónsson, H. A fast and robust algorithm for Bader decomposition of charge density. *Comput. Mater. Sci.* **2006**, 36, 354-360.
(32) Tang, W.; Sanville, E.; Henkelman, G. A grid-based Bader analysis algorithm without lattice bias. *J. Phys.: Condens. Matter* **2009**, 21, 084204.
(33) Filot, I. A. W. Introduction to microkinetic modeling. Technische Universiteit Eindhoven, 2016.
(34) Filot, I. A. W.; Zijlstra, B.; Hensen, E. J. M. MKMCXX, a C++ Program for Constructing Microkinetic Models. http://www.mkmcxx.nl (accessed Jul 27, 2021).
(35) Filot, I. A. W.; van Santen, R. A.; Hensen, E. J. M. The optimally performing Fischer−Tropsch catalyst. *Angew. Chem., Int. Ed.* **2014**, 53, 12746−12750.
(36) Filot, I. A. W.; Broos, R. J. P.; van Rijn, J. P. M.; van Heugten, G. J. H.; van Santen, R. A.; Hensen, E. J. M. First-principles based microkinetics simulations of synthesis gas conversion on a stepped rhodium surface. *ACS Catal.* **2015**, 5, 5453−5467.
(37) Matera, S.; Schneider, W. F.; Heyden, A.; Savara, A. Progress in Accurate Chemical Kinetic Modeling, Simulations, and Parameter Estimation for Heterogeneous Catalysis. *ACS Catal.* **2019**, 9, 6624-6647.
(38) Zijlstra, B.; Broos, R. J. P.; Chen, W.; Filot, I. A. W.; Hensen, E. J. M. First-principles based microkinetic modeling of transient kinetics of CO hydrogenation on cobalt catalysts. *Catal. Today* **2020**, 342, 131-141.
(39) JANAF thermochemical tables, 1982 supplement, J. Phys. Chem. Ref. Data 11 (1982) 695–940.
(40) Shomate, C. H. A method for evaluating and correlating thermodynamic data. *J. Phys. Chem.* **1954**, 58, 368–372.

(41) Savara, A. Standard States for Adsorption on Solid Surfaces: 2D Gases, Surface Liquids, and Langmuir Adsorbates. *J. Phys. Chem. C* **2013**, 117, 15710-15715.
(42) Sprowl, L. H.; Campbell, C. T.; Árnadóttir, L. Hindered Translator and Hindered Rotor Models for Adsorbates: Partition Functions and Entropies. *J. Phys. Chem. C* **2016**, 120, 9719-9731.
(43) Campbell, C. T. Finding the rate-determining step in a mechanism: comparing DeDonder relations with the "Degree of Rate Control". *J. Catal.* **2001**, 204, 520−524.
(44) Stegelmann, C.; Andreasen, A.; Campbell, C. T. Degree of rate control: How much the energies of intermediates and transition states control rates. *J. Am. Chem. Soc.* **2009**, 131, 8077−8082.

CHAPTER 3

Stable surface terminations of a perovskite oxyhydride from first principles

3.1 Abstract

Successful synthesis of some perovskite oxyhydrides and their unique catalytic properties have recently attracted researchers' attention. However, their surface structure remains unclear. Here we identify stable surface terminations of a prototypical perovskite oxyhydride, $BaTiO_{2.5}H_{0.5}$, under catalytically relevant temperatures and pressures by using first principles thermodynamics based on density functional theory. Five low-index facets, including (100), (010), (210), (011), and (211), and their various terminations for a total of 47 different surfaces have been examined for relative stability at different temperatures (700, 500, 300 K) and gas environments ($10^{-15} \leq P_{O2} \leq 1$ atm, $10^{-15} \leq P_{H2} \leq 100$ atm). The most stable ones are found to be (010)-Ba_2O_2, (210)-Ti_2O_2, and (211)-Ba_2O_4H surface terminations. These polar surfaces are stabilized by charge compensation. This work provides important insights into the stable surfaces of perovskite oxyhydrides for future studies of their catalytic properties.

3.2 Introduction

Perovskite oxyhydrides are a new class of mixed anion materials derived from the extensively explored perovskite oxides of the formula ABO_3. The larger A cations are typically Ca, Sr, Ba, Na, K, Pb, La, Nd, Pr, and Ce, while the smaller B cations are typically early 3d or 4d transition metals.[1] The perovskite structure can also incorporate non-oxide anions such as H^- and, recently, it was found that the substitution of hydride anions for

oxide in the $BaTiO_3$ perovskite can be successfully carried out, yielding the $BaTiO_{3-x}H_x$ perovskite oxyhydride solid with $x \leq 0.60$.[2] These solids are interesting materials due to their labile hydrides within the solid framework[2-6] and electronic conductivity.[2, 7, 8]

The newly discovered $BaTiO_{3-x}H_x$ perovskite oxyhydride has found many applications in catalysis. In ammonia synthesis,[9, 10] $BaTiO_{3-x}H_x$ is a more efficient support than its parent oxide, $BaTiO_3$, for the Ru metal catalyst. It is suspected that the material's labile hydrides provide a spillover pathway for the incoming H_2 required for NH_3 conversion, thus preventing the Ru metal catalyst from being poisoned.[10] The same $Ru/BaTiO_{3-x}H_x$ catalyst is also promising in CO_2 methanation.[11] Furthermore, $BaTiO_{3-x}H_x$ alone is active for ammonia synthesis as well.[9] Although some of the hydrides become replaced by nitrides, the presence of remaining labile hydrides is sufficient to continue the reaction. Likewise, the mixed oxyhydride-nitride, $BaCeO_{3-x}N_yH_z$, itself acts as a catalyst for ammonia synthesis.[12] Interestingly, the $BaCeO_{3-x}N_yH_z$ catalyst can synthesize ammonia in comparable amounts to $BaTiO_{3-x}H_x$ at the same temperature but a fifth of the pressure. This implies that a change in the B cation can have an effect on the activity of the catalyst.

The mobile hydrides within the oxyhydride framework have also been shown to be synthetically effective in the production of mixed anion material. Previously, the synthesis of $BaTiO_{2.85-y}N_{0.1}$ from $BaTiO_3$ required a temperature of 950 ^oC under a flow of NH_3.[13] But when $BaTiO_{2.4}H_{0.6}$ was used as a precursor, lower temperature ranges of 375-550 ^oC was found to be sufficient for the formation of $BaTiO_{3-x}N_{2x/3}$ with $x \leq 0.60$.[14] At even lower temperatures of 150 ^oC, the $BaTiO_{2.5}H_{0.5}$ material can undergo F-/H- exchange to form

$BaTiO_{2.5}F_{0.25}H_{0.25}$.[15, 16] In contrast, prior work reports the synthesis of $BaTiO_{3-x}F_x$ from reaction of BaO_2, BaF_2, TiO_2, and Ti requiring a temperature of 1300 °C.[17]

While the recent discovery of perovskite oxyhydrides and their applications in catalysis have been exciting, the surface structure underlying their interaction with the metal catalyst and its role in catalysis are unclear. A fundamental understanding of the surface structure of perovskite oxyhydrides is therefore much needed. To the best of our knowledge, single crystals of cubic $ATiO_{3-x}H_x$-type perovskite oxyhydrides are not available yet. While this prevents an experimental surface-science approach to examining their surface structure, a first-principles approach can nicely fill this gap and shed some light.

In this study, our goal is to use first-principles density functional theory to compare various surfaces and terminations of the prototypical perovskite oxyhydride, $BaTiO_{2.5}H_{0.5}$, to determine the stable surface structures relevant to catalytic conditions. These results will lay a foundation for future studies of surface chemistry and catalysis on the $BaTiO_{2.5}H_{0.5}$ perovskite oxyhydride itself as well as on $BaTiO_{2.5}H_{0.5}$-supported metal catalysts. Below, we first describe our computational methods and structural models for various surfaces and terminations of $BaTiO_{2.5}H_{0.5}$.

3.3 Computational Methods

Density functional theory (DFT) calculations were performed with Vienna *ab initio* Simulation Package (VASP).[18, 19] Electron exchange and correlation was treated at the general-gradient approximation (GGA) level using the Perdew-Burke-Ernzerhof (PBE) functional.[20] The electron-core interactions were described by the projector augmented-

wave (PAW) potentials.[21] The plane wave basis set kinetic cutoff energy was set to 450 eV. All calculations were performed with spin polarization. All models were optimized until the interatomic forces were less than 0.03 eV/Å and the total energy converged to within 10^{-5} eV. Bader charge analysis was used to obtain the partial atomic charges within the bulk and slab models.[22]

3.3.1 BaTiO2.5H0.5 (BTOH) Bulk Model. All surface structures studied were cleaved from the BTOH bulk. It was modeled from a 2×1×1 supercell of cubic $BaTiO_3$ perovskite with a hydrogen atom replacing the central oxygen bridging between the two cubic $BaTiO_3$ unit cells. Although bulk $BaTiO_3$ is only cubic at higher temperatures but tetragonal below 400 K,[23] $BaTiO_{3-x}H_x$ of higher hydride concentrations (~ x = 0.6) is in the cubic phase at room temperature.[2] So it is expected that $BaTiO_{2.5}H_{0.5}$ bulk would still be in the cubic phase. This is why we used cubic $BaTiO_3$ unit cells to construct the unit cell for the $BaTiO_{2.5}H_{0.5}$ (BTOH) bulk. The bulk structure and the five cleavage planes of focus are shown in Figure 3.1. The optimized lattice parameters of BTOH based on the double-cubic unit cell are a = 8.06 Å, $b = c$ = 4.03 Å, in excellent agreement with the experimental values of $a = b = c$ = 4.03 Å for BTOH based on a single cubic cell.[16]

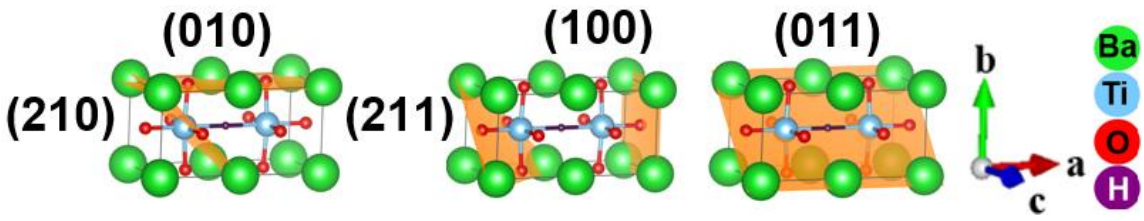

Figure 3.1 Models of bulk $BaTiO_{2.5}H_{0.5}$ with orange planes representing the studied cleavage direction.

3.3.2 Slab Models. A slab with two symmetrical terminations was used to model the semi-infinite surface structures of BTOH. Five low-Miller-index surfaces, including (100), (010), (210), (011), and (211), were examined (Figure 3.1; visualized by the VESTA program[24]). Each surface consists of a set of neutrally charged stoichiometric or nonstoichiometric terminations (see Figures 3.A1- 3.A5 in the Appendix [section 3.7] for details). A total of 47 slab models were initially built with seven layers in each slab and, later, thicker layers were also considered for thickness-dependence; the central three layers of each slab were kept fixed to simulate the bulk region while the remaining outer layers were relaxed. Each model was constructed with a 20 Å vacuum along the z-direction. A Monkhorst-Pack scheme[25] was used to sample the Brillouin zones: k-mesh of 3×6×6 for the bulk; k-meshes of 2×5×1, 5×2×1, 4×2×1, and 2×4×1 for the (100), (010), (210), and (011)/(211) surfaces, respectively.

3.3.3 Surface Grand Potential. Upon cleaving the bulk, exposed surface terminations can be stabilized when in contact with an environment.[26] The resulting free energy from this interaction is quantified as the surface grand potential (SGP).[27] The SGP is plotted as a function of the surrounding gas phase's chemical potential (in our case, H_2 and O_2). Following previous work by Wang et al.,[28] the SGP of a BTOH surface termination can be written as

$$\omega_i = \frac{1}{2S}\left[E^i_{slab} + PV - TS - N_{Ba}\mu_{Ba} - N_{Ti}\mu_{Ti} - N_O\mu_O - N_H\mu_H\right] \qquad (3.1).$$

Since DFT calculations are at 0 K and the PV term is small at reservoir pressures below 100 atm,[29] Equation (3.1) can be rewritten as

$$\omega_i = \frac{1}{2S}\left[E^i_{slab} - N_{Ba}\mu_{Ba} - N_{Ti}\mu_{Ti} - N_O\mu_O - N_H\mu_H\right] \qquad (3.2),$$

where ω_i is the SGP for termination *i*; N_{Ba}, N_{Ti}, N_O, and N_H are the number of Ba, Ti, O, and H atoms in the slab model; μ_{Ba} , μ_{Ti} , μ_O, and μ_H are the chemical potentials of Ba, Ti, O, and H atoms, and S is the surface area of termination *i*. The factor of ½ is included to give the SGP per termination of the symmetric-surface slab model. The relation between the chemical potential of the bulk phase, μ_{BTOH}, and the chemical potential of each constituent element is[27]

$$\mu_{BTOH} = E_{BTOH}^{bulk} = \mu_{Ba} + \mu_{Ti} + 2.5\mu_O + 0.5\mu_H \quad (3.3).$$

The chemical potential term can vary with respect to the computed reference chemical potential (E)[28] as listed in Equations (3.4)-(3.7)

$$\Delta\mu_{Ba} = \mu_{Ba} - E_{Ba}^{bulk} \quad (3.4)$$

$$\Delta\mu_{Ti} = \mu_{Ti} - E_{Ti}^{bulk} \quad (3.5)$$

$$\Delta\mu_O = \mu_O - \frac{1}{2}E_{O_2}^{gas} \quad (3.6)$$

$$\Delta\mu_H = \mu_H - \frac{1}{2}E_{H_2}^{gas} \quad (3.7),$$

where E_{Ba}^{bulk} and E_{Ti}^{bulk} are the electronic energies per atom from the optimized bulk Ba and Ti; $E_{H_2}^{gas}$ and $E_{O_2}^{gas}$ are the ground state electronic energies of an isolated H_2 and O_2 molecule, respectively. Substituting Equations (3.3)-(3.7) into (3.2) yields the SGP equation

$$\omega_i = \phi_i - \frac{1}{2S}[(N_{Ba} - N_{Ti})\Delta\mu_{Ba} + (N_O - 2.5N_{Ti})\Delta\mu_O + (N_H - 0.5N_{Ti})\Delta\mu_H] \quad (3.8),$$

where

$$\phi_i = \frac{1}{2S}[E_{slab}^i - N_{Ti}E_{BTOH}^{bulk} - (N_{Ba} - N_{Ti})E_{Ba}^{bulk} - (N_O - 2.5N_{Ti})\frac{1}{2}E_{O_2}^{gas} - (N_H - 0.5N_{Ti})\frac{1}{2}E_{H_2}^{gas}] \quad (3.9).$$

Values of $\Delta\mu_H$ and $\Delta\mu_O$ corresponding to pressure ranges of $10^{-15} \leq P_{H2} \leq 100$ atm and $10^{-15} \leq P_{O2} \leq 1$ atm were considered for temperatures of 700, 500, and 300 K. In Equations (3.8) and (3.9), $\Delta\mu_{Ti}$ has been eliminated and the remaining variable, $\Delta\mu_{Ba}$, is set to -5 eV. This value was determined by setting a series of thermodynamic boundary conditions prohibiting the precipitation of other Ba-, Ti-, O-, and/or H-containing compounds on the BTOH surface. Details in calculating $\Delta\mu_{Ba}$, $\Delta\mu_H$, and $\Delta\mu_O$ values are explained in the Appendix (section 3.7).

Because Ti has localized 3d electrons, SGP calculations including the Hubbard U parameter (3.3 eV for Ti 3d) were also tested. We found that the relative surface stability trends were the same with or without the U parameter, most likely because the electrons in $BaTiO_{3-x}H_x$ form a delocalized bandstate[7] and give rise to metallic conductivity at room temperature for large enough x (> 0.3).[30] Therefore, we present only the results without the U parameter for $BaTiO_{2.5}H_{0.5}$ surfaces.

As mentioned previously, the TS term in Equation (3.1) was ignored when calculating the SGPs for $BaTiO_{2.5}H_{0.5}$ surface at 0 K. To account for the vibrational energy and entropy contributions at finite temperatures, we estimated the effect of including the lattice vibrational energy and entropy contributions in the computation of SGPs using the harmonic approximation.[31] As shown in Figure 3.A6 in the Appendix (section 3.7), the most stable surface terminations remain the same with or without vibrational contributions. Thus, for the purpose of this study, finite-temperature vibrational contributions are negligible.

3.4 Results and discussion

3.4.1 Surface stability under varying oxidation/reduction conditions at 700 K.

The catalytic applications of BTOH are often at high temperatures, such as around 700 K for ammonia synthesis.[9, 10] We first evaluate the surface grand potentials (SGP) at 700 K under the varying oxidation condition: $10^{-15} \leq P_{O2} \leq 1$ atm at constant $P_{H2} = 10^{-15}$ atm. A total of 47 terminations belonging to the five surfaces [(100), (010), (210), (011), and (211)] were examined and each termination was modeled by a seven-layered slab initially. The terminations with the lowest SGPs (that is, the most stable) from each surface set were remodeled with nine to 13 layers, as described in the next section, for a more accurate and converged SGP. Figure 3.2a plots the SGPs of these stable surface terminations to identify the overall most stable surface termination under the conditions of 700 K, $P_{H2} = 10^{-15}$ atm, and $10^{-15} \leq P_{O2} \leq 1$ atm.

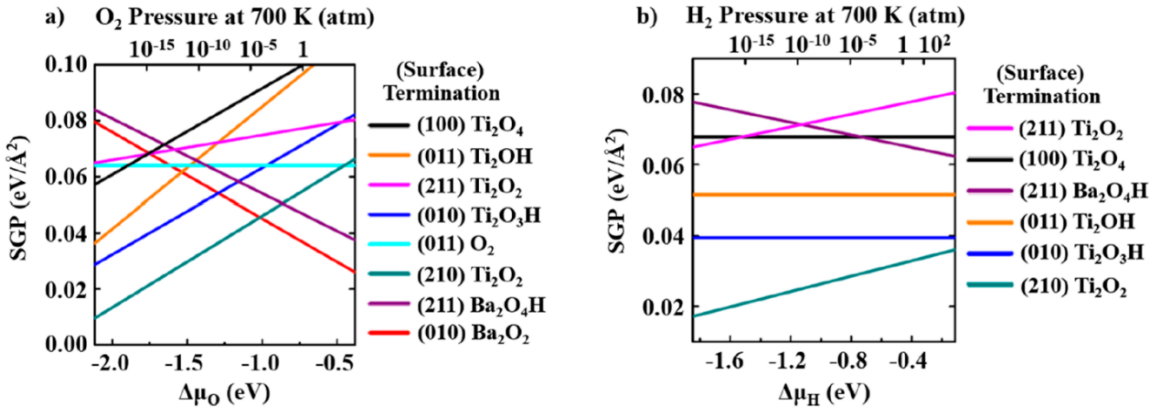

Figure 3.2 Relative stabilities of most stable $BaTiO_{2.5}H_{0.5}$ terminations at 700 K: (a) under increasing oxidation condition, with $P_{H2} = 10^{-15}$ atm and $10^{-15} \leq P_{O2} \leq 1$ atm; (b) under increasing reducing condition: $P_{O2} = 10^{-15}$ atm and $10^{-15} \leq P_{H2} \leq 100$ atm.

One can see that for $P_{O2} < 10^{-4}$ atm, the (210)-Ti_2O_2 termination is the most stable, and for $P_{O2} > 10^{-4}$ atm, the (010)-Ba_2O_2 termination is the most stable. We then evaluated the SGPs at 700 K under varying reducing conditions: $10^{-15} \leq P_{H2} \leq 100$ atm at constant $P_{O2} = 10^{-15}$ atm. As shown in Figure 3.2b, the (210)-Ti_2O_2 termination is the most stable under all H_2 pressures considered.

3.4.2 Structure of stable surface terminations. To further confirm the surface stability, the seven-layered slabs from the most stable terminations as determined from Figure 3.2 were remodeled with additional layers to reach a more accurate and converged SGP.[32] As a result, we found that while nine layers were sufficient for most of the slabs, the (100)-Ti_2O_4 surface termination required 11 layers and (211)-Ti_2O_2 required 13 layers to reach SGP convergence within 0.003 eV/Å^2. The side and top views of the most stable, relaxed nine surface terminations with their converged number of layers are depicted in Figure 3.3. The surface relaxation of each slab model in Figure 3.3 is summarized in Table 3.A1 of the Appendix (section 3.7).

The two most stable surface terminations from Figure 3.2 are (210)-Ti_2O_2 and (010)-Ba_2O_2. The relaxed (210)-Ti_2O_2 termination is a vicinal surface with a triangular-wave-like surface corrugation: the top of the triangle is a row of TiO, and the unit cell has two such rows, hence the Ti_2O_2 name; below one surface Ti atom, there are two subsurface O atoms, while below the other surface Ti atom, there is one subsurface O and one subsurface H atom. These subsurface atoms should be accessible to small adsorbates approaching the troughs of the triangular-wave-like surface corrugation of the (210)-Ti_2O_2 termination. The (010)-Ba_2O_2 termination has a rather flat surface, resembling the common

A-termination of the (100) surface of a cubic ABO_3; the hydride is in the subsurface but not directly accessible to gas phase reactants, unless there is a surface oxygen vacancy for H to diffuse out to the surface.

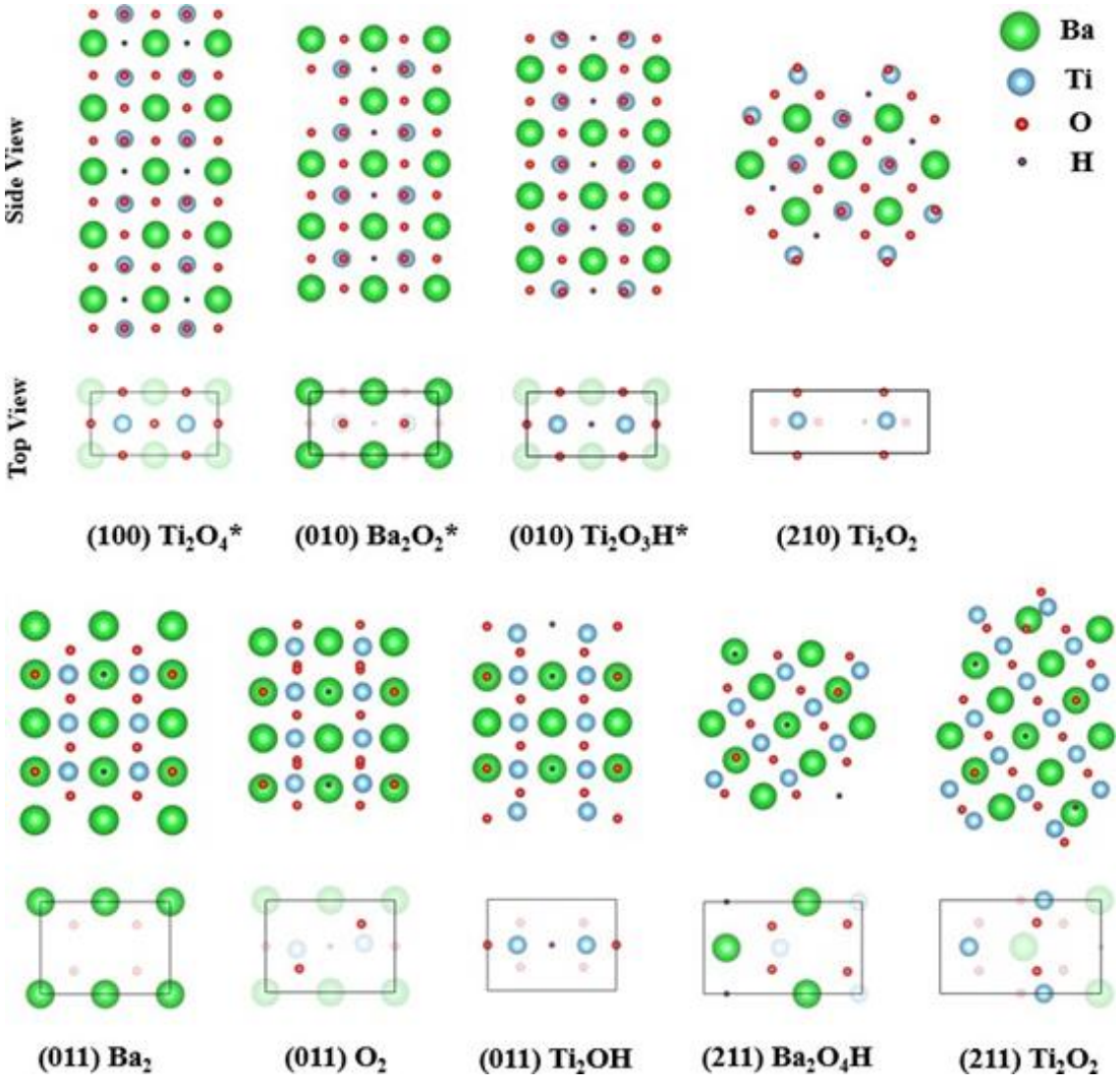

Figure 3.3 Side and top views of the nine most stable surface terminations of $BaTiO_{2.5}H_{0.5}$ after geometry optimization. Stoichiometric terminations are marked with an asterisk.

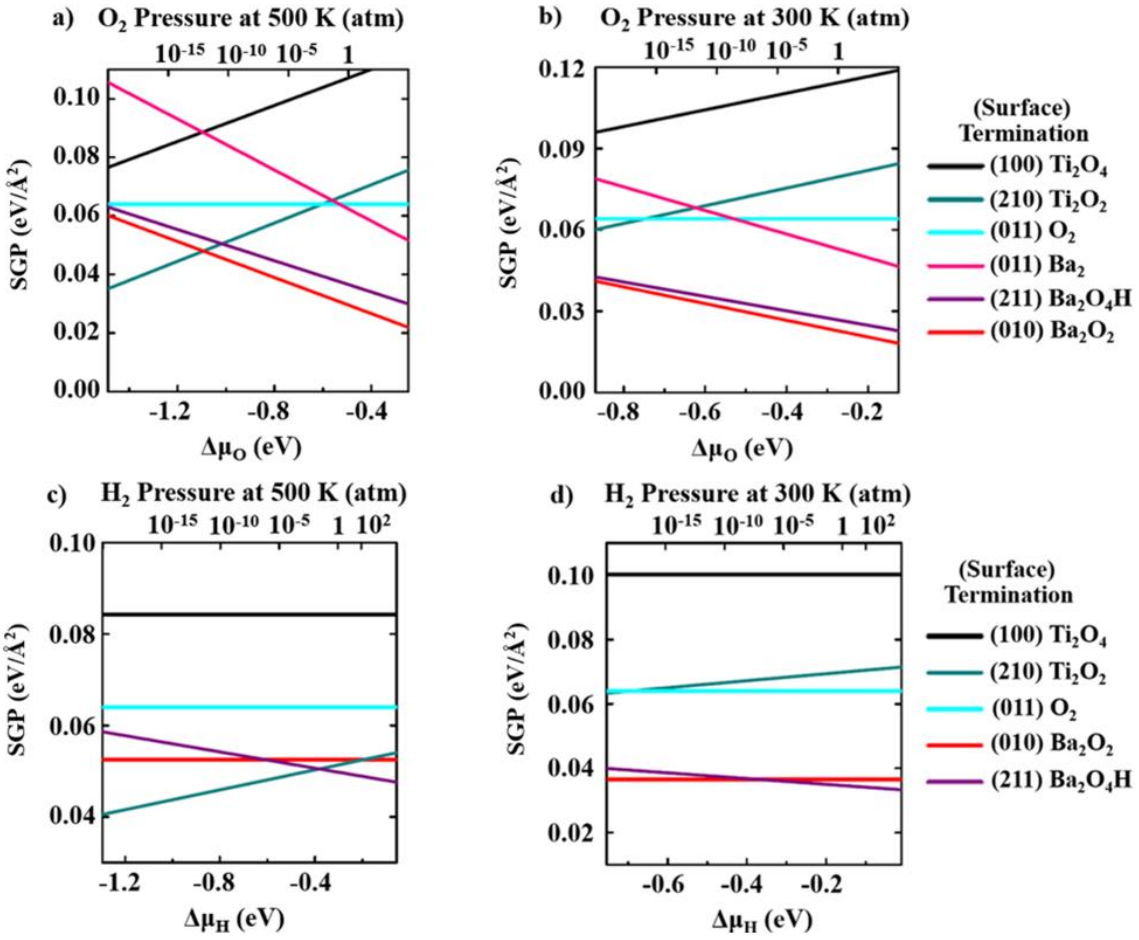

Figure 3.4 Relative stabilities of most stable $BaTiO_{2.5}H_{0.5}$ terminations at different temperatures: (a) 500 K and under increasing oxidation condition ($P_{H2} = 10^{-15}$ atm); (b) 300 K and under increasing oxidation condition ($P_{H2} = 10^{-15}$ atm); (c) 500 K and under increasing reducing condition ($P_{O2} = 10^{-15}$ atm); (d) 300 K and under increasing reducing condition ($P_{O2} = 10^{-15}$ atm).

3.4.3 Temperature effects. We next examine the temperature effect on the stability under oxidation conditions. As shown in Figure 3.4a, the crossover from (210)-Ti_2O_2 to (010)-Ba_2O_2 in terms of stability takes place now at a much lower O_2 pressure at 500 K; in other words, lowering the temperature makes (010)-Ba_2O_2 more stable over a wider range of O_2 pressures. When the temperature is further lowered to 300 K, now the (010)-Ba_2O_2

termination becomes the most stable surface over the whole O_2 pressure range considered (Figure 3.4b).

In the reducing condition, and when temperature is lowered to 500 K (Figure 3.4c), we found that the (211)-Ba_2O_4H termination becomes the most stable when the H_2 pressure is high enough (> 10^{-2} atm). When temperature is further lowered to 300 K (Figure 3.4d), the (010)-Ba_2O_2 termination replaces the (210)-Ti_2O_2 termination as the most stable at lower H_2 pressures (<10^{-7} atm). As shown in Figure 3.3, the relaxed surface of (211)-Ba_2O_4H is flat and exposes Ba, O, and H on the surface.

3.4.4 Surface phase diagram at different temperatures. Extending our stability evaluations for any given H_2/O_2 pressures at a specific temperature, we can determine the most stable surface termination at such conditions and plot the surface diagram. Figure 3.5 shows such surface diagrams at 300, 500, and 700 K. One can see that at 700 and 500 K there are three stable terminations: (010)-Ba_2O_2, (210)-Ti_2O_2, and (211)-Ba_2O_4H. At 300 K, there are two: (010)-Ba_2O_2 and (211)-Ba_2O_4H. Figure 3.5 provides a useful guide to tell the most likely surface structure of $BaTiO_{2.5}H_{0.5}$ at given temperatures and pressures of H_2 and O_2. For example, Kobayashi et al. synthesized ammonia using BTOH[9] under 5MPa of flowing N_2/H_2 with O_2 in ppt amounts at 673 K. Figure 3.5c predicts that the (210)-Ti_2O_2 termination would be the most probable surface under such conditions. The present work aims to identify the stable surface terminations of $BaTiO_{2.5}H_{0.5}$ under varying temperature and pressure conditions. One can further build upon the present work's findings to investigate the $BaTiO_{2.5}H_{0.5}$ crystal morphology based on the Gibbs-Wulff theorem. Such study would be a useful one and is warranted.

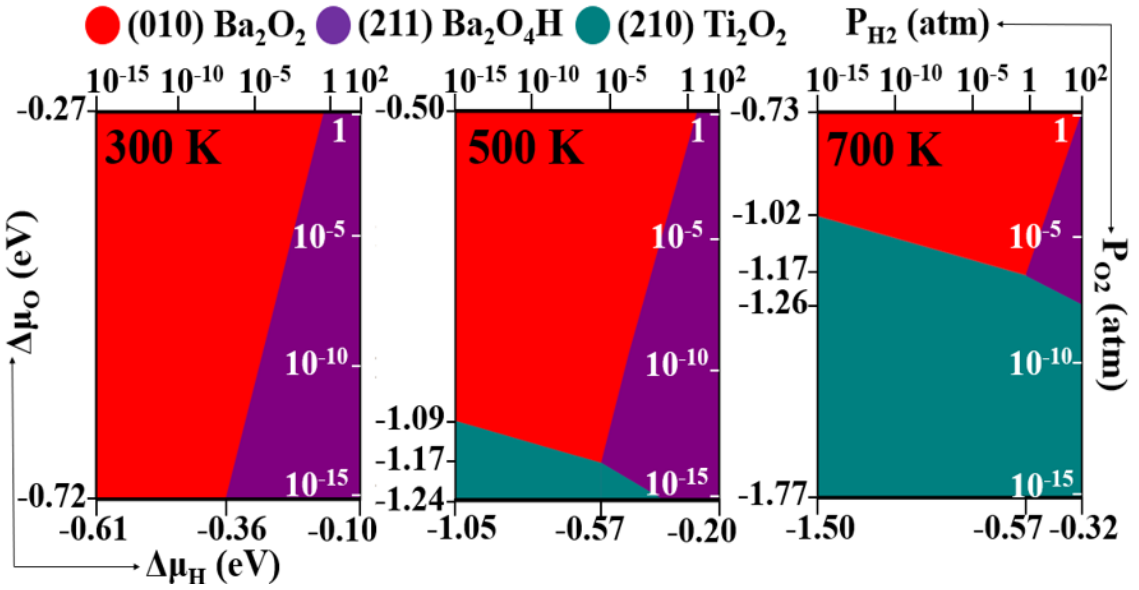

Figure 3.5 Surface diagrams of $BaTiO_{2.5}H_{0.5}$ as a function of O_2 and H_2 pressure (atm): (a) 300 K; (b) 500 K; (c) 700 K with $\Delta\mu_{Ba}$ = -5 eV. It shows that within the given pressure boundary conditions, only the (210)-Ti_2O_2 and (010)-Ba_2O_2 surface terminations are stable at 300 K. The (210)-Ti_2O_2, (010)-Ba_2O_2, and (211)-Ba_2O_4H surface terminations are stable at 500 and 700 K.

3.4.5 Charge compensation. Since many of the BTOH surfaces shown in Figure 3.3 are polar, the symmetric slabs are used to cancel the surface dipole in the supercell.[33] Here we examine the charge redistribution among the different regions of the slabs to understand the charge compensation. Equation (3.10) represents the general charge compensation criterion for a slab

$$\sum_{j=1}^{m} \sigma_j = -\frac{\sigma_{m+1}}{2} \quad (3.10),$$

where m is the number of relaxed outer layers each of which has a charge of σ_j, while σ_{m+1} is the charge of the central three layers of the slab (in our case) that resemble the bulk. Therefore, Equation (3.10) states that the total charge of the m outer layers ($\sum_{j=1}^{m} \sigma_j$) must equal to negative half of the total charge of the central three bulk-like layers (σ_{m+1}) for the

surface to be stabilized through charge compensation. Table 3.1 compares these two quantities for each slab model. One can see that all the surfaces are polar but overall, the charge compensation is well maintained.

Table 3.1 Sum of Bader charges (|e|) for the top m layers ($\sum_{j=1}^{m}\sigma_j$**)** compared with that of the central three bulk-like layers (σ_{m+1}**)** for the nine slab models (see Figure 3.3).

(Surface) Termination	**m**	$\sum_{j=1}^{m}\boldsymbol{\sigma_j}$	$\boldsymbol{\sigma_{m+1}}$	$-\frac{\boldsymbol{\sigma_{m+1}}}{\mathbf{2}}$
(100) Ti_2O_4	4	0.34	-0.72	0.36
(010) Ba_2O_2	3	0.32	-0.65	0.33
(010) Ti_2O_3H	3	-0.28	0.60	-0.30
(210) Ti_2O_2	3	2.03	-4.02	2.01
(011) Ba_2	3	2.41	-4.74	2.37
(011) O_2	3	-2.32	4.59	-2.30
(011) Ti_2OH	3	2.39	-4.80	2.40
(211) Ba_2O_4H	3	-1.93	3.88	-1.94
(211) Ti_2O_2	5	1.78	-3.52	1.76

3.5 Conclusions

We have identified stable terminations of $BaTiO_{2.5}H_{0.5}$ surfaces under catalytically relevant temperature and pressure conditions (300 – 700 K, $10^{-15} \leq P_{O2} \leq 1$ atm, $10^{-15} \leq P_{H2} \leq 100$ atm) from first principles DFT. By computing the surface grand potential, we compared 47 different terminations of $BaTiO_{2.5}H_{0.5}$ belonging to five different facets: (100), (010), (210), (011), and (211). We then constructed surface phase diagrams for different temperatures. The diagrams show that (010)-Ba_2O_2, (210)-Ti_2O_2, and (211)-

Ba_2O_4H are the most stable at 700 and 500 K and that (010)-Ba_2O_2 and (211)-Ba_2O_4H are the most stable at 300 K. While (010)-Ba_2O_2 and (211)- Ba_2O_4H are flat, (210)-Ti_2O_2 is vicinal. (211)-Ba_2O_4H exposes surface hydride and (210)-Ti_2O_2 exposes subsurface hydride, but the hydride in (010)-Ba_2O_2 is not accessible. We found that charge compensation is well maintained for all of these polar surfaces. The present work has laid a foundation to further explore surface chemistry and catalysis on the surfaces of $BaTiO_{2.5}H_{0.5}$ perovskite oxyhydride.

3.6 References

(1) Voorhoeve, R. J. H.; Remeika, J. P.; Trimble, L. E. Defect chemistry and catalysis in oxidation and reduction over perovskite-type oxides. *Ann. N.Y. Acad. Sci.* **1976**, 272, 3-21.

(2) Kobayashi, Y.; Hernandez, O. J.; Sakaguchi, T.; Yajima, T.; Roisnel, T.; Tsujimoto, Y.; Morita, M.; Noda, Y.; Mogami, Y.; Kitada, A.; Ohkura, M.; Hosokawa, S.; Li, Z.; Hayashi, K.; Kusano, Y.; Kim, J.; Tsuji, N.; Fujiwara, A.; Matsushita, Y.; Yoshimura, K.; Takegoshi, K.; Inoue, M.; Takano, M.; Kageyama, H. An oxyhydride of $BaTiO_3$ exhibiting hydride exchange and electronic conductivity. *Nat. Mater.* **2012**, 11, 507-511.

(3) Tang, Y.; Kobayashi, Y.; Shitara, K.; Konishi, A.; Kuwabara, A.; Nakashima, T.; Tassel, C.; Yamamoto, T.; Kageyama, H. On Hydride Diffusion in Transition Metal Perovskite Oxyhydrides Investigated via Deuterium Exchange. *Chem. Mater.* **2017**, 29, 8187-8194.

(4) Sakaguchi, T.; Kobayashi, Y.; Yajima, T.; Ohkura, M.; Tassel, C.; Takeiri, F.; Mitsuoka, S.; Ohkubo, H.; Yamamoto, T.; Kim, J.; Tsuji, N.; Fujihara, A.; Matsushita, Y.; Hester, J.; Avdeev, M.; Ohoyama, K.; Kageyama, H. Oxyhydrides of (Ca, Sr, Ba) TiO_3 Perovskite Solid Solutions. *Inorg. Chem.* **2012**, 51, 11371-11376.

(5) Zhang, J.; Gou, G.; Pan, B. Study of Phase Stability and Hydride Diffusion Mechanism of $BaTiO_3$ Oxyhydride from First-Principles. *J. Phys. Chem. C* **2014**, 118, 17254-17259.

(6) Eklöf-Österberg, C.; Nedumkandathil, R.; Häussermann, U.; Jaworski, A.; Pell, A. J.; Tyagi, M.; Jalarvo, N. H.; Frick, B.; Faraone, A.; Karlsson, M. Dynamics of Hydride Ions in Metal Hydride-Reduced $BaTiO_3$ Samples Investigated with Quasielastic Neutron Scattering. *J. Am. Chem. C* **2019**, 123, 2019-2030.

(7) Granhed, E. J.; Lindman, A.; Eklöf-Österberg, C.; Karlsson, M.; Parker, S. F.; Wahnström, G. Band vs. polaron: vibrational motion and chemical expansion of hydride ions as signatures for the electronic character in oxyhydride barium titanate. *J. Mater. Chem. A* **2019**, 7, 16211-16221.

(8) Yajima, T.; Kitada, A.; Kobayashi, Y.; Sakaguchi, T.; Bouilly, G.; Kasahara, S.; Terashima, T.; Takano, M.; Kageyama, H. Epitaxial Thin Films of $ATiO_{3-x}H_x$ (A=Ba, Sr, Ca) with Metallic Conductivity. *J. Am. Chem. Soc.* **2012**, 134, 21, 8782-8785.

(9) Kobayashi, Y.; Tang, Y.; Kageyama, T.; Yamashita, H.; Masuda, N.; Hosokawa, S.; Kageyama, H. Titanium-Based Hydrides as Heterogeneous Catalysts for Ammonia Synthesis. *J. Am. Chem. Soc.* **2017**, 139, 18240-18246.

(10) Tang, Y.; Kobayashi, Y.; Masuda, N.; Uchida, Y.; Okamoto, H.; Kageyama, T.; Hosokawa, S.; Loyer, F.; Mitsuhara, K.; Yamanaka, K.; Tamenori, Y.; Tassel, C.; Yamamoto, T.; Tanaka, T.; Kageyama, H. Metal-Dependent Support Effects of Oxyhydride-Supported Ru, Fe, Co Catalysts for Ammonia Synthesis. *Adv. Energy Mater.* **2018**, 8, 1801772.

(11) Tang, Y.; Kobayashi, Y.; Tassel, C.; Yamamoto, T.; Kageyama, H. Hydride-Enhanced CO_2 Methanation: Water-Stable $BaTiO_{2.4}H_{0.6}$ as a New Support. *Adv. Energy Mater.* **2018**, 8, 1800800.

(12) Kitano, M.; Kujirai, J.; Ogasawara, K.; Matsuishi, S.; Tada, T.; Abe, H.; Niwa, Y.; Hosono, H. Low-Temperature Synthesis of Perovskite Oxynitride-Hydrides as Ammonia Synthesis Catalysts. *J. Am. Chem. Soc.* **2019**, 141, 20344-20353.

(13) Bräuniger, T.; Müller, T.; Pampel, A.; Abicht, H.-P. Study of oxygen-Nitrogen Replacement in $BaTiO_3$ by ^{14}N Solid-State Nuclear Magnetic Resonance. *Chem. Mater.* **2005**, 17, 4114-4117.

(14) Yajima, T.; Takeiri, F.; Aidzu, K.; Akamatsu, H.; Fujita, K.; Yoshimune, W.; Ohkura, M.; Lei, S.; Gopalan, V.; Tanaka, K.; Brown, C. M.; Green, M. A.; Yamamoto, T.; Kobayashi, Y.; Kageyama, H. A labile hydride strategy for the synthesis of heavily nitridized $BaTiO_3$. *Nat. Chem.* **2015**, 7, 1017-1023.

(15) Kobayashi, Y.; Hernandez, O.; Tassel, C.; Kageyama, H. New chemistry of transition metal oxyhydrides. *Sci. Technol. Adv. Mater.* **2017**, 18, 905-918.

(16) Masuda, N.; Kobayashi, Y.; Hernandez, O.; Bataille, T.; Paofai, S.; Suzuki, H.; Ritter, C.; Ichijo, N.; Noda, Y.; Takegoshi, K.; Tassel, C.; Yamamoto, T.; Kageyama, H. Hydride in $BaTiO_{2.5}H_{0.5}$: A Labile Ligand in Solid State Chemistry. *J. Am. Chem. Soc.* **2015**, 137, 15315-15321.

(17) Endo, T.; Kobayashi, T.; Sato, T.; Shimada, M. High pressure synthesis and electrical properties of $BaTiO_{3-x}F_x$. *J. Mater. Sci.* **1990**, 25, 619-623.

(18) Kresse, G.; Furthmüller, J. Efficiency of ab-initio total energy calculations for metals and semiconductors using a plane-wave basis set. *Comput. Mater. Sci.* **1996**, 6, 15-50.

(19) Kresse, G.; Furthmüller, J. Efficient Iterative Schemes for Ab Initio Total-Energy Calculations Using a Plane-Wave Basis Set. *Phys. Rev. B: Condens. Matter Mater. Phys.* **1996**, 54, 11169-11186.

(20) Perdew, J. P.; Burke, K.; Ernzerhof, M. Generalized Gradient Approximation Made Simple. *Phys. Rev. Lett.* **1996**, 77, 3865.
(21) Blöchl, P. E. Projector Augmented-Wave Method. *Phys. Rev. B: Condens. Matter Mater. Phys.* **1994**, 50, 17953-17979.
(22) Tang, W.; Sanville, E.; Henkelman, G. A grid-based Bader analysis algorithm without lattice bias. *J. Phys.: Condens. Matter* **2009**, 21, 084204.
(23) Smith, M. B.; Page, K.; Siegrist, T.; Redmon, P. L.; Walter, E. C.; Seshadri, R.; Brus, L. E.; Steigerwald, M. L. Crystal Structure and the Paraelectric-to-Ferroelectric Phase Transition of Nanoscale $BaTiO_3$. *J. Am. Chem. Soc.* **2008**, 130, 6955-6963.
(24) Momma, K.; Izumi, F. VESTA 3 for three-dimensional visualization of crystal, volumetric and morphology data. *J. Appl. Cryst.* **2011**, 44, 1272-1276.
(25) Monkhorst, H. J.; Pack, J. D. Special points for Brillouin-zone integrations. *Phys. Rev. B: Solid State* **1976**, 13, 5188-5192.
(26) Xie, Y.; Yu, H.; Zhang, G.; Fu, H.; Suu, J. First-Principles Investigation of Stability and Structural Properties of the $BaTiO_3$ (110) Polar Surface. *J. Phys. Chem. C* **2007**, 111, 6343-6349.
(27) Bottin, F.; Finocchi, F.; Noguera, C. Stability and electronic structure of the (1×1) $SrTiO_3$ (110) polar surfaces by first-principles calculations. *Phys. Rev. B* **2003**, 68, 035418.
(28) Wang, Y.; Cheng, J.; Behtash, M.; Tang, W.; Luo, J.; Yang, K. First-principles studies of polar perovskite $KTaO_3$ surfaces: structural reconstruction, charge compensation, and stability diagram. *Phys. Chem. Chem. Phys.* **2018**, 20, 18515-18527.
(29) Reuter, K.; Scheffler, M. Composition, structure, and stability of RuO_2 (110) as a function of oxygen pressure. *Phys. Rev. B* **2001**, 65, 035406.
(30) Bouilly, G.; Yajima, T.; Terashima, T.; Yoshimune, W.; Nakano, K.; Tassel, C.; Kususe, Y.; Fujita, K.; Tanaka, K.; Yamamoto, T.; Kobayashi, Y.; Kageyama, H. Electrical Properties of Epitaxial Thin Films of Oxyhydrides $ATiO_{3-x}H_x$ (A = Ba and Sr). *Chem. Mater.* **2015**, 27, 6354-6359.
(31) Fultz, B. Vibrational thermodynamics of materials. Prog. Mater. Sci. **2010**, 247-352).
(32) Fiorentini, V.; Methfessel, M. Extracting convergent surface energies from slab calculations. *J. Phys.: Condens. Matter* **1996**, 8, 6525-6529.
(33) Noguera, C. Polar oxide surfaces. *J. Phys.: Condens. Matter* **2000**, 12, R367.

3.7 Appendix

3.A1 Surface Relaxations

Table 3.A1 The surface relaxations (Å) of the nine stable surface terminations of study. A positive (negative) value indicates the average outward (inward) direction of displacement by Ba, Ti, O, and/or H atoms in layers 1-5 (L1-L5) of each slab model.

Surface		(100)	(010)		(011)			(210)	(211)	
Terminations		Ti_2O_4	Ba_2O_2	Ti_2O_3H	Ba_2	O_2	Ti_2OH	Ti_2O_2	Ba_2O_4H	Ti_2O_2
L1	Ba		-0.02		-0.19				0.07	
	Ti	-0.04		-0.07			-0.25	-0.19		-0.02
	O	0.04	-0.04	0.04		-0.16	0.16	0.13	-0.09	0.04
	H			0.04			0.28		-0.06	
L2	Ba	0.12		0.05		0.20				0.28
	Ti		0.04			-0.09			0.07	
	O		0.04	0.04	0	-0.03	0	0		-0.01
	H	0.16	0.04			0		0.03		0.47
L3	Ba		0		0.08		-0.03	0	0.09	
	Ti	0		-0.04	0.03		0.03	0.06		0.07
	O	0.04	0.04	0	0	0.08	-0.03	-0.03	-0.04	
	H			0	0.03		-0.03		0	
L4	Ba	0.04								-0.02
	Ti									
	O	0								0.03
	H									0
L5	Ba									
	Ti									0.04
	O									
	H									

3.A2 Details in Computing the Surface Grand Potentials

3.A2.A. Quantifying $\Delta\mu_H$ and $\Delta\mu_O$

Assuming ideal-gas behavior, $\mu_H(T,P)$ can be expressed as[1]

$$\mu_H(T,P) = \mu_H(T,P^o) + \frac{1}{2}kTln(\frac{P}{P^o}) \quad (3.A1).$$

Rearranging Equation (3.7) from the main text to $\mu_H(T,P) = \Delta\mu_H(T,P) + \frac{1}{2}E_{H_2}^{gas}$ and substituting into Equation (3.A1) yields

$$\Delta\mu_H(T,P) = \mu_H(T,P^o) - \frac{1}{2}E_{H_2}^{gas} + \frac{1}{2}kTln(\frac{P}{P^o}) \quad (3.A2).$$

If we set the reference state, $\mu_H(0\ K, P^o)$, to be the energy of hydrogen in an isolated H_2 molecule, we can write[Error! Bookmark not defined.]

$$\mu_H(T, P^o) - \frac{1}{2}E_{H_2}^{gas} = \frac{1}{2}G_{H_2}(T, P^o) - \frac{1}{2}G_{H_2}(0K, P^o) \quad (3.A3),$$

where

$$\frac{1}{2}G_{H_2}(T, P^o) - \frac{1}{2}G_{H_2}(0\ K, P^o) = \frac{1}{2}[H_{H_2}(T, P^o) - H_{H_2}(0\ K, P^o)] - \frac{1}{2}T[S_{H_2}(T, P^o) - S_{H_2}(0\ K, P^o)] \quad (3.A4).$$

Enthalpy and entropy values for H_2 were obtained from the JANAF thermochemical tables[2] which report these energies per mole of substance at P^o (1 atm) under various temperature conditions. The result from Equation (3.A3) was substituted into Equation (3.A2) with pressure, P, within $10^{-15} \leq P_{H2} \leq 100$ atm. This same procedure was used to calculate $\Delta\mu_O$ with P within $10^{-15} \leq P_{O2} \leq 1$ atm. Table 3.A2 lists the values of $\Delta\mu_H$ and $\Delta\mu_O$ used in calculating the SGP for the $BaTiO_{2.5}H_{0.5}$ (BTOH) surface terminations considered.

Table 3.A2 Chemical potentials (in eV) for O and H at varying pressures (atm) and temperatures (K)

	700 K		500 K		300 K	
Pressure	$\Delta\mu_H$	$\Delta\mu_O$	$\Delta\mu_H$	$\Delta\mu_O$	$\Delta\mu_H$	$\Delta\mu_O$
10^{-15}	-1.50	-1.77	-1.05	-1.24	-0.61	-0.72
10^{-10}	-1.15	-1.42	-0.80	-0.99	-0.46	-0.57
10^{-5}	-0.81	-1.08	-0.55	-0.74	-0.31	-0.42
1	-0.46	-0.73	-0.30	-0.50	-0.16	-0.27
100	-0.32		-0.20		-0.10	

3.A2.B Determining $\Delta\mu_{Ba}$

We are most interested in calculating SGPs of clean BTOH surface terminations without the formation of precipitates. Therefore, the following conditions must be satisfied for Ba, Ti, O, and H atoms to not be deposited on the surfaces[3,4]

$$\Delta\mu_{Ba} < 0 \tag{3.A5}$$

$$\Delta\mu_{Ti} < 0 \tag{3.A6}$$

$$\Delta\mu_{O} < 0 \tag{3.A7}$$

$$\Delta\mu_{H} < 0 \tag{3.A8}.$$

Inequalities (3.A5)-(3.A8) give the upper boundary limit for the chemical potentials of each constituting element. By combining Equation (3.3) from the main text and Equation (3.A6), we obtain the following lower boundary condition:

$$\Delta\mu_{Ba} + 2.5\Delta\mu_{O} + 0.5\Delta\mu_{H} > \Delta H_f(BaTiO_{2.5}H_{0.5}) \tag{3.A9}.$$

There are also a variety of substances that can form from the combinations of Ba, Ti, O, and/or H atoms within the BTOH material. In order to prevent these corresponding substances from precipitating onto the surfaces, the following boundary conditions must be true[3]

$$\Delta\mu_{Ba} + \Delta\mu_{O} < \Delta H_f(BaO) \tag{3.A10}$$

$$\Delta\mu_{Ti} + 2\Delta\mu_{H} < \Delta H_f(TiH_2) \tag{3.A11}$$

$$\Delta\mu_{Ti} + 2\Delta\mu_{O} < \Delta H_f(TiO_{2,\ rutile}) \tag{3.A12}$$

$$\Delta\mu_{Ba} + 2\Delta\mu_O + 2\Delta\mu_H < \Delta H_f(Ba(OH)_2) \quad (3.A13)$$

$$\Delta\mu_{Ba} + 2\Delta\mu_H < \Delta H_f(BaH_2) \quad (3.A14)$$

$$\Delta\mu_O + 2\Delta\mu_H < \Delta H_f(H_2O) \quad (3.A15).$$

While other substances such as TiO_2 (anatase) and H_2O_2 can also form, their heat of formations are higher than those listed in Inequalities (3.A12) and (3.A15). Only substances with lower heat of formations are considered to further constrain the boundary condition. A sample calculation for the heat of formation of bulk $BaTiO_{2.5}H_{0.5}$ is listed below:[3]

$$\Delta H_f(BaTiO_{2.5}H_{0.5}) = E_{BTOH}^{bulk} - E_{Ba}^{bulk} - E_{Ti}^{bulk} - 2.5\left(\frac{1}{2}E_{O_2}^{bulk}\right) - 0.5(\frac{1}{2}E_{H_2}^{bulk}) \quad (3.A16).$$

All heat of formations in Inequalities (3.A10)-(3.A15) are calculated similarly. Plugging in the associated heat of formation values into Inequalities (3.A9)-(3.A15) along with the calculated $\Delta\mu_O$ and/or $\Delta\mu_H$ values at different temperatures and pressures from Table 3.A2 gives ranges of appropriate $\Delta\mu_{Ba}$ that can be chosen for SGP calculations. A $\Delta\mu_{Ba}$ value of -5 eV was chosen as a result. It is important to note that the $\Delta\mu_H$ and $\Delta\mu_O$ values recorded in Table 3.A2 in combination with $\Delta\mu_{Ba}$ = -5 eV do not satisfy all boundary conditions listed in Inequalities (3.A9)-(3.A15). However, this procedure still provides a general guideline for choosing an appropriate $\Delta\mu_{Ba}$ value that best represents the formation of a clean BTOH surface in the absence of unwanted precipitation by atoms or other substances.

3.A3 Optimized Geometries of Bulk Materials and Reference States

This section lists the optimized geometries, in fractional coordinates, of each bulk material used to determine the value of $\Delta\mu_{Ba}$. The corresponding space groups[5,6] followed by the Monkhorst-Pack k-point grid used for each bulk material are indicated in parentheses. No space group was designated for systems consisting of a small molecule in a large cubic cell. The structures of bulk $Ba(OH)_2$, BaH_2, and TiH_2 were downloaded from the Open Quantum Materials Database (OQMD).[7,8]

$BaTiO_{2.5}H_{0.5}$ (space group: P4/mmm; k-mesh used: 3 × 6 × 6)

```
4.0300000000000002
    2.0000000000000000 0.0000000000000000 0.0000000000000000
    0.0000000000000000 1.0000000000000000 0.0000000000000000
    0.0000000000000000 0.0000000000000000 1.0000000000000000
  Ba   Ti   O    H
  2    2    5    1
Direct
 -0.0000088305922951 -0.0000000744716003  0.0000001901313323
  0.5000071947734379  0.0000000127423596 -0.0000001308954777
  0.2419895003732961  0.5000000509970608  0.5000000845914642
  0.7579811987448319  0.4999999084803107  0.4999998383124237
 -0.0000050164162309  0.4999998090335747  0.4999998712732276
  0.2572195892499656  0.0000002905508464  0.5000007952486185
  0.2572192094891504  0.4999999285303932  0.0000005691419533
  0.7427923712303642 -0.0000001078094860  0.4999992477376725
  0.7427925343888070  0.5000002588868835 -0.0000005332370076
  0.5000122037586797  0.4999999230596576  0.5000000676957932
```

Ba (space group: Im-3m; k-mesh used: 4 × 4 × 4)

```
5.0800000000000001
    1.0000000000000000 0.0000000000000000 0.0000000000000000
    0.0000000000000000 1.0000000000000000 0.0000000000000000
    0.0000000000000000 0.0000000000000000 1.0000000000000000
Ba
2
Direct
  0.0000000000000000  0.0000000000000000  0.0000000000000000
  0.5000000000000000  0.5000000000000000  0.5000000000000000
```

BaH_2 (space group: Pnma; k-mesh used: 3 × 5 × 3)

```
6.8200000000000003
    1.0000000000000000 0.0000000000000000 0.0000000000000000
    0.0000000000000000 0.6140000000000000 0.0000000000000000
```

0.0000000000000000 0.0000000000000000 1.1570000000000000
H Ba
8 4
Direct
0.0310550846104078 0.2499999713983572 0.1812410642673755
0.9689450193716614 0.7500005485716531 0.8187599921514445
0.4689448552755153 0.7500002275637446 0.6812402186348380
0.5310548272177801 0.2499989565158226 0.3187591282697499
0.6442593526395539 0.2500002605899487 0.9282615351540571
0.3557413428800242 0.7499990190879636 0.0717385148426826
0.8557404185897517 0.7500012010284233 0.4282614726501522
0.1442593000973666 0.2499999525012465 0.5717389386128053
0.2591030994372291 0.2499983627264313 0.8884385271365797
0.7408973067324546 0.7500014638571072 0.1115614086421794
0.2408961890303563 0.7499996803811841 0.3884383415053669
0.7591031471179047 0.2500003557781176 0.6115608661327765

BaO (space group: Fm-3m; k-mesh used: 4 × 4 × 4)

5.6200000000000001
1.0000000000000000 0.0000000000000000 0.0000000000000000
0.0000000000000000 1.0000000000000000 0.0000000000000000
0.0000000000000000 0.0000000000000000 1.0000000000000000
Ba O
4 4
Direct
0.0000000000000000 0.0000000000000000 0.0000000000000000
0.0000000000000000 0.5000000000000000 0.5000000000000000
0.5000000000000000 0.0000000000000000 0.5000000000000000
0.5000000000000000 0.5000000000000000 0.0000000000000000
0.5000000000000000 0.5000000000000000 0.5000000000000000
0.5000000000000000 0.0000000000000000 0.0000000000000000
0.0000000000000000 0.5000000000000000 0.0000000000000000
0.0000000000000000 0.0000000000000000 0.5000000000000000

$Ba(OH)_2$ (space group: $P2_1/c$; k-mesh used: 3 × 3 × 2)

6.8200000000000003
1.0000000000000000 0.0000000000000000 -0.1020000000000000
0.0000000000000000 1.1739999999999999 0.0000000000000000
0.0000000000000000 0.0000000000000000 1.3970000000000000
Ba H O
8 16 16
Direct
0.7506748598951078 0.1429034034162831 0.1025475459592469
0.2171851661924908 0.4503073121866132 0.1830127722256468
0.2828164624839469 0.9503023370797047 0.3169816111895100
0.7493226279730770 0.6429147866119944 0.3974539788076565
0.2506773917120006 0.3570849929504473 0.6025461350240747
0.7171839181684528 0.0496983276383200 0.6830181442238336
0.7828149691062675 0.5496927363830111 0.8169873763139603
0.2493251037725269 0.8570964869465399 0.8974525339880913

0.2268362225746514 0.1499440547671437 0.0248020492662489
0.5516729217070985 0.7550543242792257 0.0972272943083408
0.6908906400539750 0.5386081547798083 0.1180366126020395
0.9368833699585520 0.7327718679615756 0.1195291946761605
0.5631173977014465 0.2327727157870136 0.3804698875993756
0.8091107136648807 0.0386100539327934 0.3819663900487740
0.9483236608757007 0.2550555526182249 0.4027704019451218
0.2731642836478113 0.6499413508147229 0.4751993367069925
0.7268357685621085 0.3500587148051658 0.5248007469399510
0.0516764000315960 0.7449443197712985 0.5972295213585355
0.1908894341978823 0.9613897395270712 0.6180335033368309
0.4368826462343842 0.7672274107841659 0.6195301497775828
0.0631166416142941 0.2672281453402794 0.8804707862919290
0.3091092828573278 0.4613917333237657 0.8819634797561111
0.4483270224302851 0.2449455972361612 0.9027726512862343
0.7731637255563835 0.8500559441186879 0.9751980529222204
0.3537173079470491 0.1413273986484939 0.0853872020923081
0.9885705110006491 0.8444904788993007 0.1011879677258761
0.8240061025559192 0.4929184456012459 0.1172031146054814
0.4728911931907511 0.6999085880668933 0.1643368209998511
0.0271103933633123 0.1999043884227028 0.3356664994128439
0.6759950631010987 0.9929185936786724 0.3827981516545169
0.5114279872028301 0.3444899876113747 0.3988132433130404
0.1462826512726491 0.6413299202349041 0.4146130772720927
0.8537169852757178 0.3586703361593662 0.5853869863021690
0.4885719216624647 0.6555099921288740 0.6011868454008281
0.3240049501023521 0.0070812010601389 0.6172019133290573
0.9728894942502139 0.8000954619324149 0.6643334532930040
0.5271090285694698 0.3000915417286383 0.8356633011544534
0.1759936679632488 0.5070814941370894 0.8827967327105271
0.0114295378882448 0.1555094232937538 0.8988118914818785
0.6462825736817821 0.8586726853361191 0.9146126426976026

H_2 (molecule; k-mesh used: 1 × 1 × 1)

1.0000000000000000
20.0000000000000000 0.0000000000000000 0.0000000000000000
0.0000000000000000 20.0000000000000000 0.0000000000000000
0.0000000000000000 0.0000000000000000 20.0000000000000000
H
2
Direct
-0.0000000000000202 -0.0000000000000070 0.0348675423371724
0.0000000000000202 0.0000000000000070 0.0723924576628242

H_2O (molecule; k-mesh used: 1 × 1 × 1)

1.0000000000000000
20.0000000000000000 0.0000000000000000 0.0000000000000000
0.0000000000000000 20.0000000000000000 0.0000000000000000
0.0000000000000000 0.0000000000000000 20.0000000000000000
H O

2 1
Direct
0.4598878551875883 0.1332351984813023 0.0000101252148377
0.5362824743244726 0.1247009610029408 0.9999898300541034
0.5013896474879336 0.1585538345157524 0.0000000307310649

O_2 (molecule; k-mesh used: 1 × 1 × 1)

1.0000000000000000
20.0000000000000000 0.0000000000000000 0.0000000000000000
0.0000000000000000 20.0000000000000000 0.0000000000000000
0.0000000000000000 0.0000000000000000 20.0000000000000000
O
2
Direct
0.0000072521996231 0.0000047077143785 0.0345233911403283
-0.0000072521996231 -0.0000047077143785 0.0961966098596719

Ti (space group: $P6_3/mmc$; k-mesh used: 7 × 7 × 4)

2.9300000000000002
1.0000000000000000 0.0000000000000000 0.0000000000000000
-0.5000000000000000 0.8660000000000000 0.0000000000000000
0.0000000000000000 0.0000000000000000 1.5859999999999999
Ti
2
Direct
0.3333333460000034 0.6666666919999997 0.2500000000000000
0.6666666209999974 0.3333333229999980 0.7499999750000015

TiH_2 (space group: I4/mmm; k-mesh used: 6 × 6 × 5)

3.1899999999999999
1.0000000000000000 0.0000000000000000 0.0000000000000000
0.0000000000000000 1.0000000000000000 0.0000000000000000
0.0000000000000000 0.0000000000000000 1.3369999999999997
H Ti
4 2
Direct
0.5000000000000000 0.0000000000000000 0.2500000000000000
0.0000000000000000 0.5000000000000000 0.2500000000000000
0.5000000000000000 0.0000000000000000 0.7500000000000000
0.0000000000000000 0.5000000000000000 0.7500000000000000
0.0000000000000000 0.0000000000000000 0.0000000000000000
0.5000000000000000 0.5000000000000000 0.5000000000000000

Rutile TiO_2 (space group: $P4_2/mnm$; k-mesh used: 4 × 4 × 8)

4.6399999999999997
1.0000000000000000 0.0000000000000000 0.0000000000000000
0.0000000000000000 1.0000000000000000 0.0000000000000000
0.0000000000000000 0.0000000000000000 0.6440000000000000
Ti O
2 4

Direct

0.0000000000000000	0.0000000000000000	0.0000000000000000
0.5000000000000000	0.5000000000000000	0.5000000000000000
0.3047999980000000	0.3047999980000000	0.0000000000000000
0.6951999500000028	0.6951999500000028	0.0000000000000000
0.1952000020000000	0.8048000499999972	0.5000000000000000
0.8048000499999972	0.1952000020000000	0.5000000000000000

3.A4 (100) Slab Models

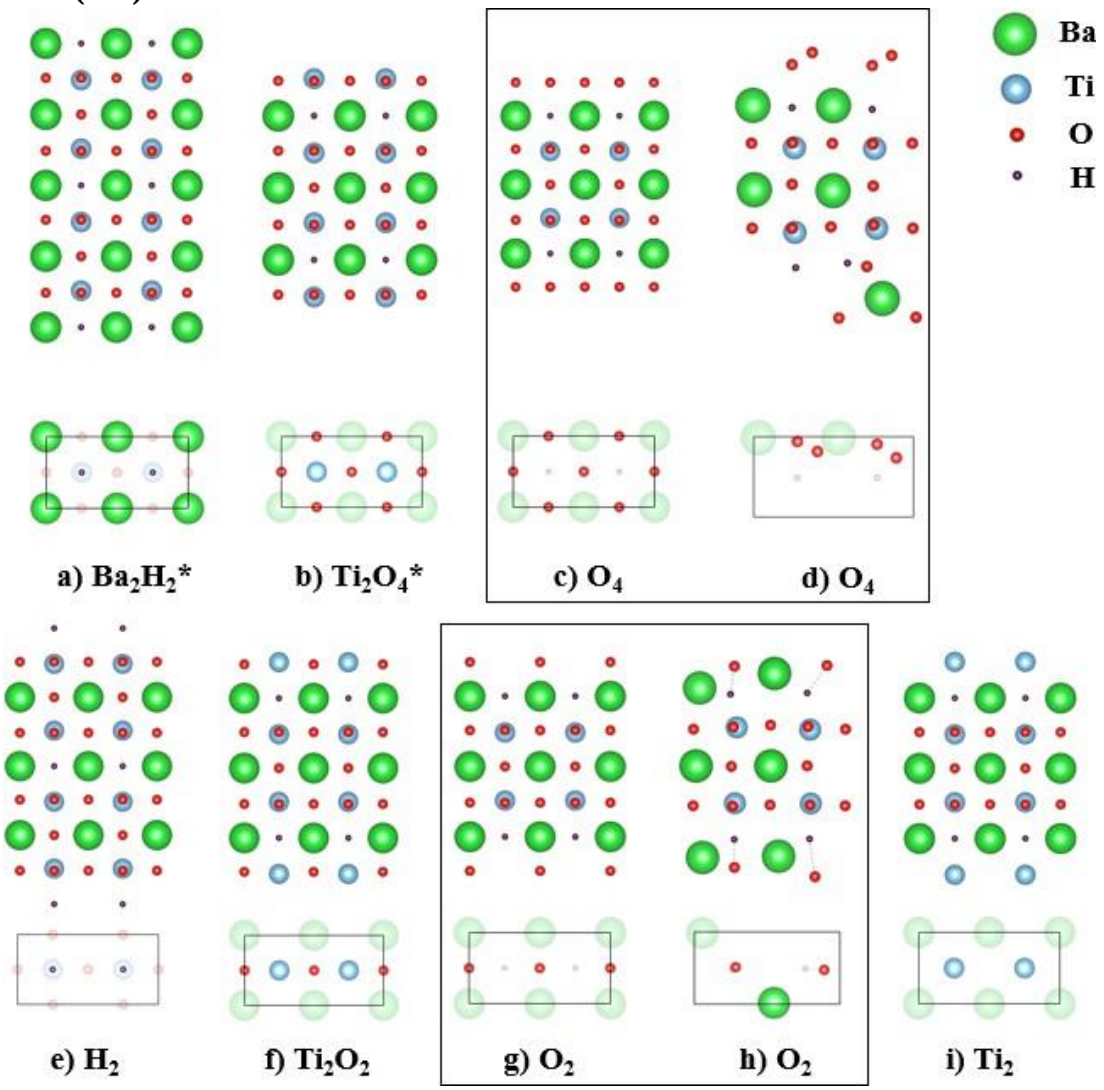

Figure 3.A1 Side and top views of the seven slab models of different (100) terminations prior to relaxation. The (100) Ba_2H_2 and H_2 slab model required nine layers to preserve slab symmetry. The (100) O_4 and (100) O_2 surface terminations were not considered in the process of identifying the most stable BTOH surface termination due to severe reconstruction at the surface. (c) and (g) show the slab models prior to relaxation while (d) and (h) show the models after relaxation. The (100) O_4 surface seemed to relax to a structure (d) with the four surface oxygen atoms rearranging to form two O_2 molecules adsorbed to the surface of a (100) Ba_2H_2 surface termination. The (100) O_2 surface termination relaxed to a structure (h) containing hydrogen bonds (dashed lines) formed between the surface oxygen atoms and sub-surface hydrogen atoms. Stoichiometric terminations are marked with an asterisk.

3.A5 (010) Slab Models

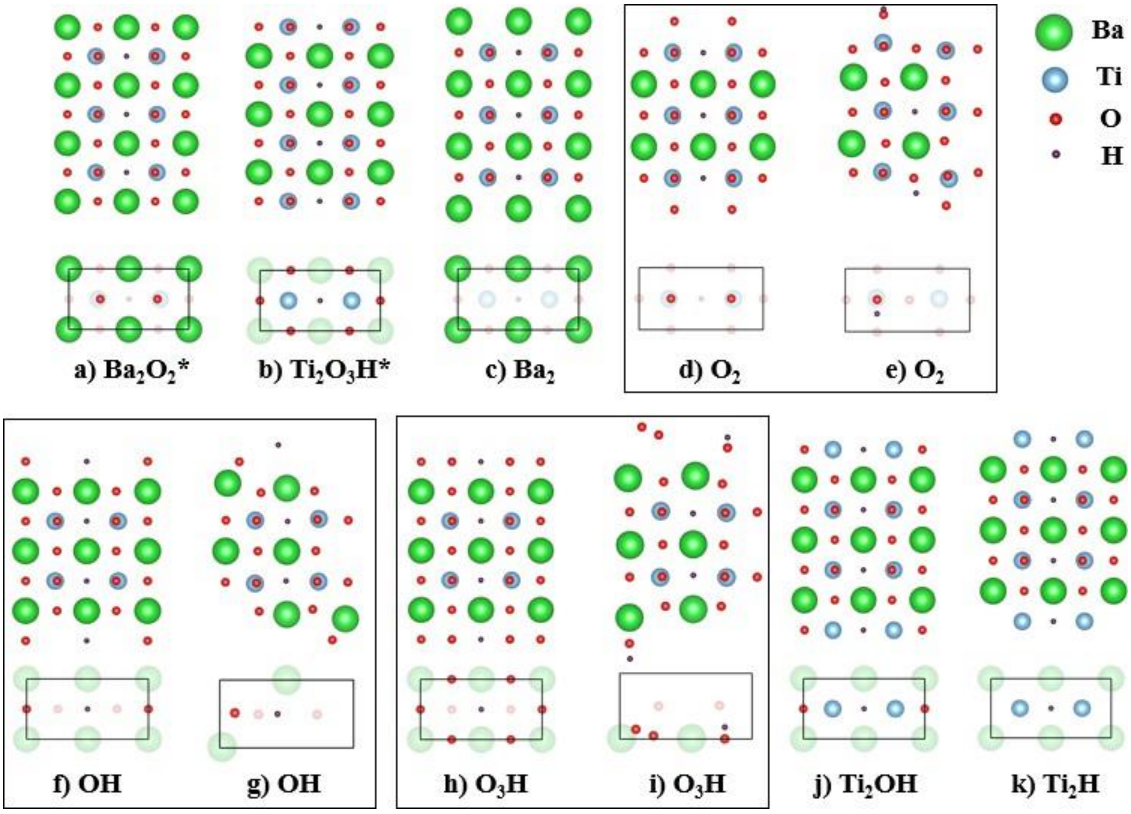

Figure 3.A2 Side and top views of the eight slab models of different (010) terminations prior to relaxation. The (010) O_2, (010) OH, and (010) O_3H surface terminations were not considered in the process of identifying the most stable BTOH surface termination due to severe reconstruction at the surface. (d), (f), and (h) show the slab models prior to relaxation while (e), (g), and (i) show the models after relaxation. The (010) O_2 surface seemed to relax to a structure (e) with a sub-surface hydrogen atom bonded to a surface oxygen atom to form a surface hydroxyl group. The hydrogen vacancy is subsequently replaced by the second surface oxygen atom. The (010) OH surface termination relaxed to a structure that seemed to contain a hydrogen atom being desorbed from the surface. The (010) O_3H surface termination relaxed to a structure (i) in which (1) a sub-surface hydrogen atom becomes bonded with a surface oxygen atom to form a surface hydroxyl group and (2) two oxygen atoms from the surface seems to form an O_2 molecule adsorbed to the surface. Stoichiometric terminations are marked with an asterisk.

3.A6 (210) Slab Models

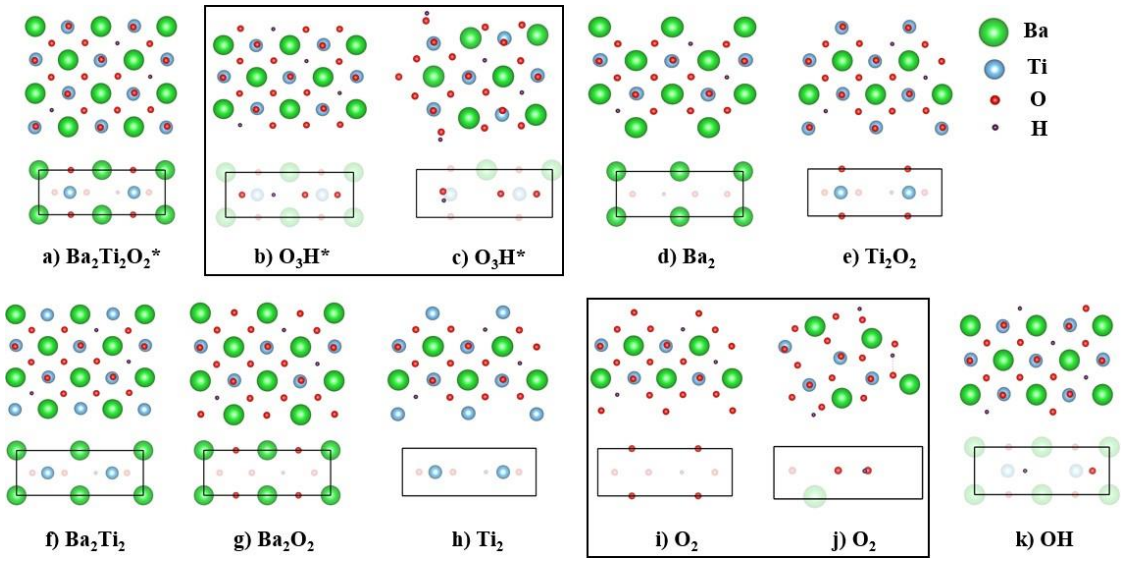

Figure 3.A3 Side and top views of the nine slab models of different (210) terminations prior to relaxation. The (210) O_3H and (210) O_2 surface terminations were not considered in the process of identifying the most stable BTOH surface termination due to severe reconstruction at the surface. (b) and (i) show the slab models prior to relaxation while (c) and (j) show the surfaces after relaxation. The (210) O_3H surface seemed to relax to a structure (c) with a surface hydrogen atom bonded to a neighboring surface oxygen atom to form a surface hydroxyl group. The (010) O_2 surface termination relaxed to a structure (j) with severe atom rearrangement. All hydrogen atoms in the (010) O_2 slab model formed hydroxyl groups with neighboring oxygen atoms. Stoichiometric terminations are marked with an asterisk.

3.A7 (011) Slab Models

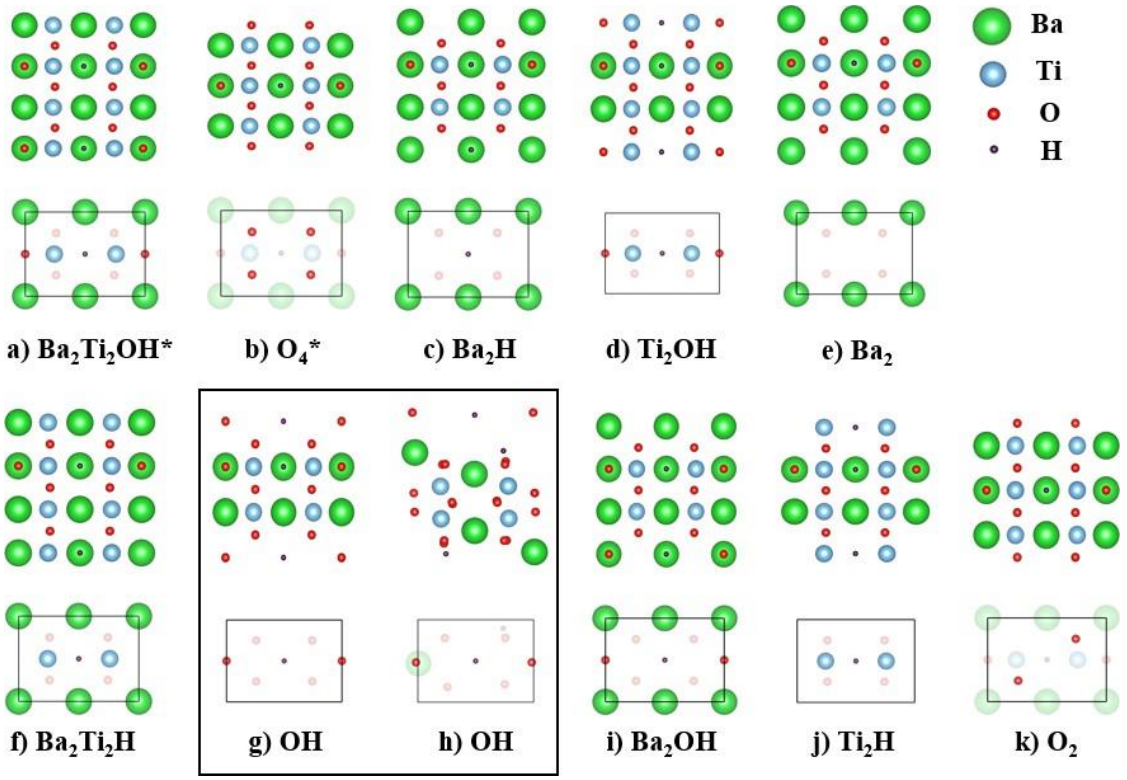

Figure 3.A4 Side and top views of the ten slab models of different (011) terminations prior to relaxation. The (011) OH surface termination was not considered in the process of identifying the most stable BTOH surface termination due to severe reconstruction at the surface. (g) shows the slab model prior to relaxation while (h) shows the model after relaxation. The (011) OH surface seemed to relax to a structure (h) with inner hydrogen atoms bound to neighboring oxygen atoms to form sub-surface hydroxyl groups. Stoichiometric terminations are marked with an asterisk.

3.A8 (211) Slab Models

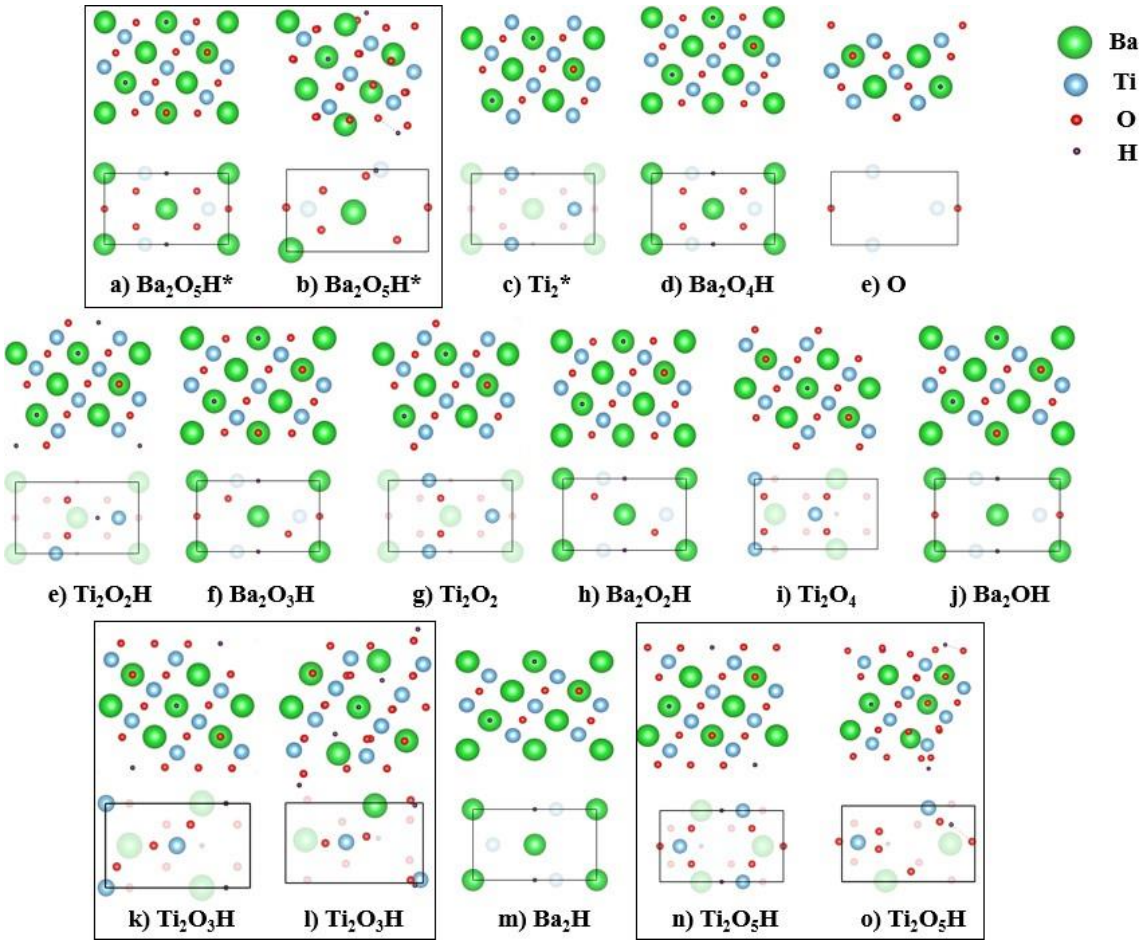

Figure 3.A5 Side and top views of the 13 slab models of different (211) terminations prior to relaxation. The (211) Ba_2O_5H, (211) Ti_2O_3H and Ti_2O_5H surface terminations were not considered in the process of identifying the most stable BTOH surface termination due to severe reconstruction at the surface. (a), (k), and (n) show the slab models prior to relaxation while (b), (l), and (o) show the models after relaxation. The (211) Ba_2O_5H surface seemed to relax to a structure (b) with a surface hydrogen atom bonded to a neighboring surface oxygen atom to form a hydroxyl group. This is also the case for (211) Ti_2O_3H and (211) Ti_2O_5H. The relaxed (211) Ti_2O_5H slab structure also forms an O_2 molecule, from two surface oxygen atoms, that is adsorbed to the surface. Stoichiometric terminations are marked with an asterisk.

3.A9 Surface Grand Potentials Including Vibrational Contributions

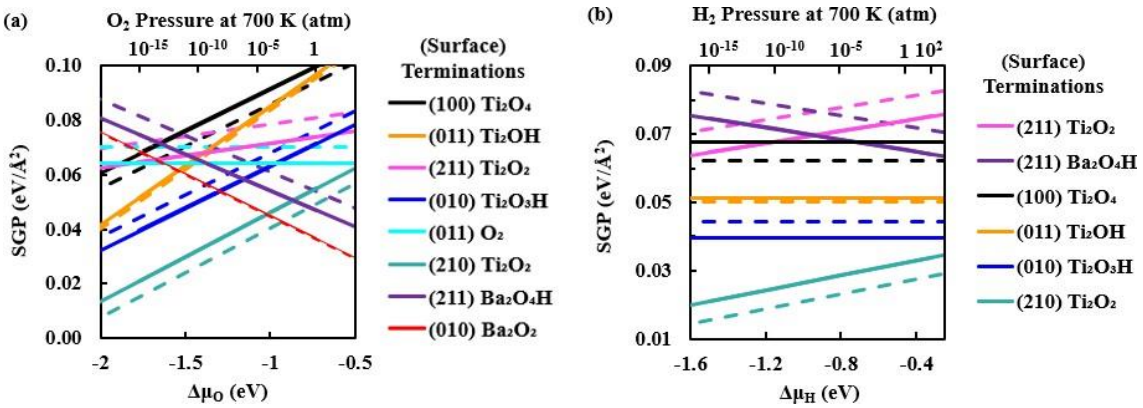

Figure 3.A6 Surface grand potential (SGP) plots calculated with (dashed lines) and without (solid lines) vibrational energy and entropy contributions and the relative stabilities of the most stable $BaTiO_{2.5}H_{0.5}$ terminations at 700 K under increasing oxidation conditions at constant $P_{H2} = 10^{-15}$ atm (a) and reducing conditions at constant $P_{O2} = 10^{-15}$ atm (b). ($\Delta\mu_{Ba}$ = -4.5 eV).

Using the harmonic approximation, the Helmholtz vibrational free energy contribution was calculated as:[9]

$$\boldsymbol{F_{vib} = \frac{1}{2}\sum_i^{3N} \varepsilon_i + k_B T \sum_i^{3N} \ln\left(1 - e^{-\beta\varepsilon_i}\right)},$$

where ε_i is the corresponding energy of each frequency calculated at the gamma point, k_B is the Boltzmann constant, T = 700 K, and β is $(k_B T)^{-1}$. The zone-center frequencies were calculated using the finite difference method in VASP.

3.A10 References

(1) Reuter, K.; Scheffler, M. Composition, structure, and stability of RuO2 (110) as a function of oxygen pressure. *Phys. Rev. B* **2001**, 65, 035406.

(2) Chase, M. W. *NIST-Janaf Thermochemical Tables,* NIST Standard Reference Database, 1998; 13. https://janaf.nist.gov

(3) Wang, Y.; Cheng, J.; Behtash, M.; Tang, W.; Luo, J.; Yang, K. First-principles studies of polar perovskite KTaO3 surfaces: structural reconstruction, charge compensation, and stability diagram. *Phys. Chem. Chem. Phys.* **2018**, 20, 18515-18527.

(4) Xie, Y.; Yu, H.; Zhang, G.; Fu, H.; Suu, J. First-Principles Investigation of Stability and Structural Properties of the BaTiO3 (110) Polar Surface. *J. Phys. Chem. C* **2007**, 111, 6343-6349.

(5) Stokes, H. T.; Hatch, D. M.; Campbell, B. J. FINDSYM, ISOTROPY Software Suite, iso.byu.edu.

(6) Stokes, H. T.; Hatch, D. M. Program for Identifying the Space Group Symmetry of a Crystal. *J. Appl. Cryst.* **2005**, 38, 237-238.

(7) Saal, J. E.; Kirklin, S.; Aykol, M.; Meredig, B.; Wolverton, C. Materials Design and Discovery with High-Throughput Density Functional Theory: The Open Quantum Materials Database (OQMD). *JOM* **2013**, 65, 1501-1509.

(8) Kirklin, S.; Saal, J. E.; Meredig, B.; Thompson, A.; Doak, J. W.; Aykol, M.; Rühl, S.; Wolverton, C. The Open Quantum Materials Database (OQMD): assessing the accuracy of DFT formation energies. Npj *Comput. Mater.* **2015**, 1, 15010.

(9) Fultz, B. Vibrational thermodynamics of materials. *Prog. Mater. Sci.* **2010**, 55, 247-352

CHAPTER 4

Ammonia synthesis on $BaTiO_{2.5}H_{0.5}$: computational insights into the role of hydrides

4.1 Abstract

Perovskite oxyhydrides such as $BaTiO_{2.5}H_{0.5}$ have been found to be able to catalyze NH_3 synthesis, but the mechanism and the role of the catalyst's lattice hydrides in the catalytic reaction remain unknown. Here we employ first principles density functional theory to investigate the mechanism of ammonia synthesis and the role of lattice hydrides on a prototypical perovskite oxyhydride, $BaTiO_{2.5}H_{0.5}$ (BTOH). Two mechanistic hypotheses, the distal and alternating pathways, have been tested on the Ti_2O_2 termination of the BTOH (210) surface, previously determined to be the most stable surface termination under the reaction conditions considered. In the distal pathway, H atoms hydrogenate N_2 to form the $*N–NH_x$ key intermediates, followed by N–N bond breaking. In the alternating pathway, H atoms hydrogenate N_2 in an alternating fashion to form the $*NH_x–NH_y$ intermediates before N–N bond breaking and formation of co-adsorbed $*NH_x/*NH_y$ on the surface. We find that the subsurface hydride vacancy formed after reaction of $*N_2$ with the lattice hydride is key to the distal pathway, leading to surface nitride formation after breaking the $*N–NH_3$ bond, while the neighboring surface Ti sites are key to bridging and stabilizing the *NNH intermediate in the alternating pathway. In both pathways, desorption of NH_3 is the most uphill in energy. Our results provide important insights into the role of hydrides and surface vacancies in hydrogenation reactions over BTOH, which will be useful to guide future spectroscopic experiments such as operando IR and inelastic neutron scattering to verify the key intermediates.

4.2 Introduction

Complex oxides, composed of at least two metallic elements, find wide applications in thermal catalysis,[1] electrocatalysis,[2] and photocatalysis.[3] Their surfaces can take on numerous configurations and expose different combinations of metal cations and anions, thus providing a myriad of local chemical environments more diverse than binary oxides. For example, when the ABO_3-type perovskite, $LaNiO_3$, is used as the catalyst in CO_2 hydrogenation, CO_2 is selectively converted into CH_4.[4] However, when La cations are partially replaced by K cations, the reaction selectivity shifts from CO_2 methanation to the reverse water gas shift (rWGS) reaction. The incorporation of K promotes the formation of thermally unstable C-intermediates that escape hydrogenation to form the rWGS reaction products rather than CH_4 from CO_2 methanation.[4]

The catalytic properties of complex oxides can also be tuned by anion substitution such as in the case of perovskite oxyhydrides ($ABO_{3-x}H_x$). These mixed-anion perovskite materials are the hydride-reduced forms of the ABO_3 perovskites where lattice O^{2-} are randomly replaced by H^- to form the mixed-anion material.[5–7] Previously, there have been very few well-characterized oxyhydride compounds; the first mixed oxyhydride was discovered in 1982 with the synthesis of LaHO.[8] This material was found to be highly hygroscopic and released hydrogen when in contact with ambient moisture. Later on, other oxyhydride materials such as $Ba_3(AlO_4)H$[9] and $Ba_{21}Ge_2O_5H_{24}$[10] were synthesized, albeit under extremely reducing conditions. It was not until 2002 when Hayward *et al.* showed how the $LaSrCoO_4$ layered-perovskite's structure can be preserved upon reacting with CaH_2 to form the $LaSrCoO_3H_{0.7}$ oxyhydride using a soft chemistry method.[11] These earlier

works paved the way to the discovery of an air- and water-stable barium titanium oxyhydride in 2012 by Kobayashi *et al.*[5] Since then, a vast number of other types of perovskite oxyhydrides have been synthesized, which contain other elements such as Sc,[12] V,[13,14] Cr,[15] or Mn[16] as the B-cation.

Catalysis over perovskite oxyhydride solids has lately been of interest due to the impact that lattice hydrides have on the oxyhydride's redox properties and electronic structure. For example, using the $BaTiO_{3-x}H_x$ perovskite oxyhydride as a support results in an enhanced catalytic activity in hydrogenation reactions including CO_2 methanation and ammonia synthesis.[17,18] This observed improvement in reaction rate was attributed to the following factors: (i) the material's labile hydrides providing a spillover pathway for the incoming H_2, thus preventing the Ru metal catalyst from being poisoned; (ii) the participation of lattice hydrides in the catalytic cycle *via* a hydride-based Mars–van Krevelen (MvK) mechanism; (iii) the transfer of charges to the metal centers, which assists in N_2 activation.[17,18] Furthermore, $BaTiO_{3-x}H_x$ (with $x = 0.5$) alone is also active for ammonia synthesis under conditions (*i.e.* 400 °C, 5 MPa) comparable to the Haber–Bosch conditions over an iron-based catalyst.[19,31] But the role of lattice hydrides in ammonia synthesis over $BaTiO_{2.5}H_{0.5}$ has been unclear.

Perovskite oxyhydrides can further incorporate nitride ions because their labile hydrides[5–7,20,21] can easily desorb as H_2[5,6] or exchange with nitrogen anions or halides starting at a temperature of 673 K.[22] This property further enriched their catalytic capability. For instance, the $BaCeO_{3-x}N_yH_z$ perovskite oxynitride–hydride was shown to be able to incorporate its lattice nitrogen and hydrogen species in the synthesis of ammonia

and subsequently replace those lattice sites by gas-phase nitrogen or hydrogen *via* an anion-vacancy mediated MvK mechanism.[23]

The emergence of perovskite oxyhydrides as a new class of mixed-anion materials for catalysis necessitates fundamental understandings of their surface structure and the corresponding structure–activity–selectivity relationships for catalysis. Building off our previous study on the stable surface terminations of $BaTiO_{2.5}H_{0.5}$,[30] here we aim to reveal the role of lattice hydrides in $BaTiO_{2.5}H_{0.5}$ (BTOH) for ammonia synthesis from N_2 and H_2. This work will also lay a foundation for future studies of BTOH as a support for metal catalysts. Below, we first introduce the computational methods and our surface model.

4.3 Computational methods

Spin-polarized density functional theory (DFT) calculations were performed using the Vienna *ab initio* simulation package (VASP).[24,25] Electron exchange and correlation energies were treated at the general-gradient approximation (GGA) level using the Perdew–Burke–Ernzerhof (PBE) functional[26] and the electron-core interactions were described by the projector augmented-wave (PAW) potentials.[27] The electronic wave functions were expanded using a plane wave basis set with kinetic cutoff energy of 450 eV and the van der Waals interactions were accounted for by DFT-D3.[28] The convergence criteria for force and energy were 0.02 eV $Å^{-1}$ and 10^{-5} eV, respectively. Bader charge analysis was used to obtain the partial atomic charges.[29]

The same BTOH double-cubic, tetragonal unit cell from our previous study[30] was used and has lattice parameters of a = 8.06 Å, $b = c$ = 4.03 Å. The BTOH (210)-Ti_2O_2 surface termination, previously determined to be the most stable termination[30] under

the NH_3 synthesis conditions[31] *via* first principles thermodynamics applied to perovskite surfaces,[32] was used as a model structure for mechanistic studies. Here we note that, because we used the double-cubic cell for our bulk BTOH structure, the (210) surface of our unit cell resembles the (110) surface of a cubic unit cell of $BaTiO_3$. The bottom three layers of the six-layered slab for the BTOH (210)-Ti_2O_2 surface were fixed in their bulk positions and a 3 × 3 × 1 *k*-point mesh in the Monkhorst–Pack scheme[33] was used to sample its Brillouin zone. To compensate the net dipole moment along the surface normal due to slab asymmetry, a dipole correction[34] was included.

Adsorption energies were calculated according to the equation

$$E_{ads} = E_{surface+adsorbate} - (E_{surface} + E_{adsorbate}) \quad (4.1)$$

where $E_{\text{surface+adsorbate}}$, E_{surface}, and $E_{\text{adsorbate}}$ are the electronic energies for the adsorbate-slab system (adsorbates are either a reactant, intermediate, or product), the clean surface, and the isolated adsorbate molecules (H_2, N_2, or NH_3), respectively. The energies of N_2, H_2, and NH_3 were computed by placing each adsorbate in a 15 × 15 × 15 $Å^3$ cell. The climbing-image nudged elastic band (CI-NEB) method[35] was used to search the transition state for H_2 dissociation over the BTOH surface; the force convergence criterion was set to 0.05 eV $Å^{-1}$ and the transition state found was verified by vibrational frequency analysis.

The change in Gibbs free energy corresponding to NH_3 desorption (ΔG_{des}) from the surface was approximated using the following equation

$$\Delta G_{des} = \Delta H_{des} - T\Delta S_{des} \approx (\Delta E_{elec} + \Delta E_{vib}) - T\Delta S_{des} \quad (4.2)$$

where ΔE_{elec} is the change in electronic energy, ΔE_{vib} is the change in vibrational energy (including the zero-point energy), T is temperature at 673 K, and ΔS_{des} is the change in

entropy between the adsorbed state (initial state) and the desorbed state (final state). The finite-difference method, as implemented in VASP, was used to compute the vibrational frequencies of isolated NH_3 and NH_3 adsorbed on a completely fixed slab. We approximate the rotational and vibrational entropic contributions to be less than the translational entropic contribution and

$$\Delta S_{des} = S_{NH_3} - S_{NH_3{}^*} = S_{NH_3} - \left(S_{NH_3} - S_{NH_3,trans}\right) = S_{NH_3,trans} \qquad (4.3)$$

where S_{NH3} is the total entropy of gaseous NH_3, S_{NH3*} is the total entropy of adsorbed NH_3, and $S_{NH3,trans}$ is the translational entropy of gaseous NH_3. The Sackur–Tetrode equation was used to calculate the translational entropy of NH_3 in the gaseous state.[36] See section 4.A1 of the Appendix (section 4.7) for the details used to calculate ΔG_{des} and $S_{NH_3,trans}$.

4.4 Results and discussion

The key steps of NH_3 synthesis include N_2 adsorption and activation, H_2 adsorption and activation, and NH_3 formation and desorption. Because of the complication and complexity from the expected participation of lattice hydrides in the reaction, our mechanistic studies will especially focus on the role of hydrides and hydrogenation steps. We start with an analysis of the surface structure of the BTOH (210)-Ti_2O_2 termination.

4.4.1 Structure of BTOH (210)-Ti2O2 surface termination. We previously found[30] that the most stable BTOH surface termination under NH_3 synthesis conditions (673 K and under 5 MPa of pressure)[31] is (210)-Ti_2O_2. A side view of the 2 × 2 slab model and of the top two layers are shown in Figure 4.1. This vicinal surface has a corrugated surface structure with each of the two ridges consisting of TiO (Figure 4.1b), hence the Ti_2O_2 name. The 2 × 2 supercell exposes four surface Ti and four surface O atoms. Ti^A and

Ti^B have an average Bader charge of +1.84 |*e*|, each bonded to two subsurface O atoms; Ti^C and Ti^D are slightly more reduced and have an average Bader charge of +1.71 |*e*|, each bonded to one subsurface O and one subsurface H atom (Figure 4.1b). The bond lengths between surface and subsurface atoms of the BTOH (210)-Ti_2O_2 surface are shown in Figure 4.1b. The two different types of Ti atoms on the surface are a result of an electron donation into the Ti 3d conduction bands when O^{2-} is substituted by H^- during the hydride reduction of $BaTiO_3$.[7,37] It is expected that the two different types of surface Ti will have different reactivity toward reactants, which is examined next.

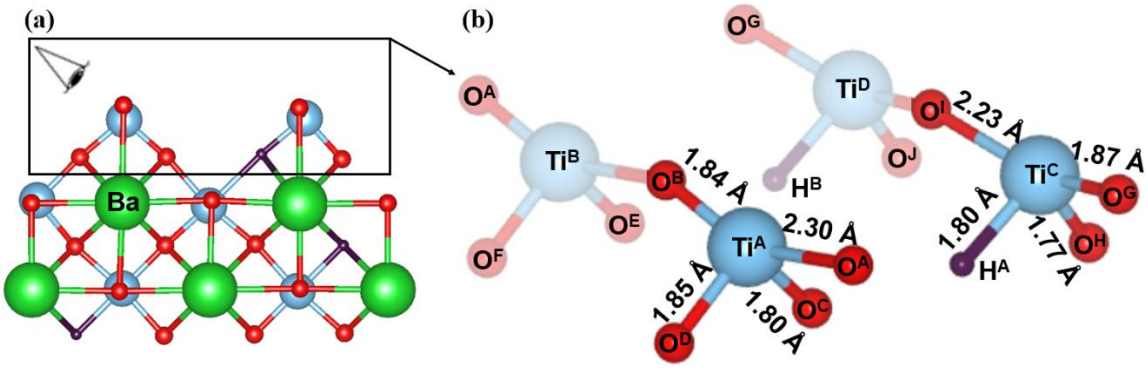

Figure 4.1 Structure model of the (210)-Ti_2O_2 surface of $BaTiO_{2.5}H_{0.5}$: (a) side view of the slab; (b) perspective view of the top two layers showing various Ti, O, and H sites as well as the bond lengths between surface and subsurface atoms. Since the slab model is a 2×2 supercell, the distances between atoms of the faded region are the same as the distances between atoms of the unfaded region.

4.4.2 Adsorption of reactants on the BTOH (210)-Ti2O2 surface. The adsorption positions of the N_2 and H_2 molecules on BTOH were first determined prior to exploring ammonia synthesis pathways over the catalytic surface. To fully consider all possible adsorption sites, N_2 and H_2 were adsorbed at surface sites of different coordination

environments (Figure 4.1b) and the corresponding adsorption energies are reported in Table 4.1, while the most stable adsorption structures of each molecule are shown in Figure 4.2. One can see that H_2 preferably adsorbs onto a surface Ti than an O site, with no selectivity for Ti^A or Ti^C, and adopts a tilted geometry with one H atom closer to the Ti atom (Figure 2a and b). The same adsorption energy of H_2 on the two different Ti sites can be attributed to the physical nature of the adsorption, which is less sensitive to the chemical difference between the two Ti sites.

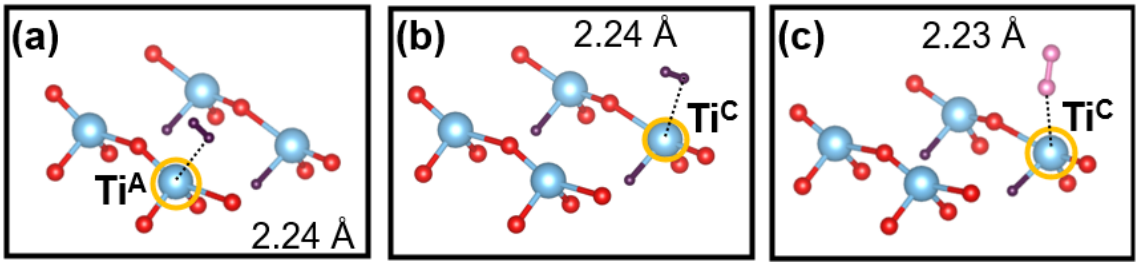

Figure 4.2 The most stable adsorption structures for H_2 (a and b) and N_2 (c) on the (210)-Ti_2O_2 surface of $BaTiO_{2.5}H_{0.5}$. Shown also are the distances (dashed lines) between the adsorbate and the nearest surface atom (circled in yellow and labeled). Color code: blue, Ti; red, O; pink, N; purple, H.

N_2 activation typically occurs when the molecule's filled σ- and π-orbitals interact with the metal's d_z^2 or $d_{x^2-y^2}$ orbitals and the electrons in the metal's d_{xz}, d_{yz}, or d_{xy} orbitals back-donate into the vacant π*-orbital of N_2.[38] Hence, we considered only the Ti sites for N_2 adsorption. We found that the N_2 molecule prefers to adsorb terminally (Figure 4.2c) on the more reduced Ti^C atom than on Ti^A (Table 4.1). Local density of states (DOS) as a result of the interaction between the N_2 molecule with Ti^A or Ti^C is shown in Figure 4.3.

Table 4.1 Adsorption energies (E_{ads}) of N_2 and H_2 on the different surface sites of BTOH (210)-Ti_2O_2.

Adsorbate	Surface Site	E_{ads} (eV)	Adsorbate	Surface Site	E_{ads} (eV)
N_2	Ti^A	-0.31	H_2	O^A	-0.08
N_2	Ti^C	-0.42	H_2	O^B	-0.08
H_2	Ti^A	-0.22	H_2	O^G	-0.07
H_2	Ti^C	-0.22	H_2	O^I	-0.06

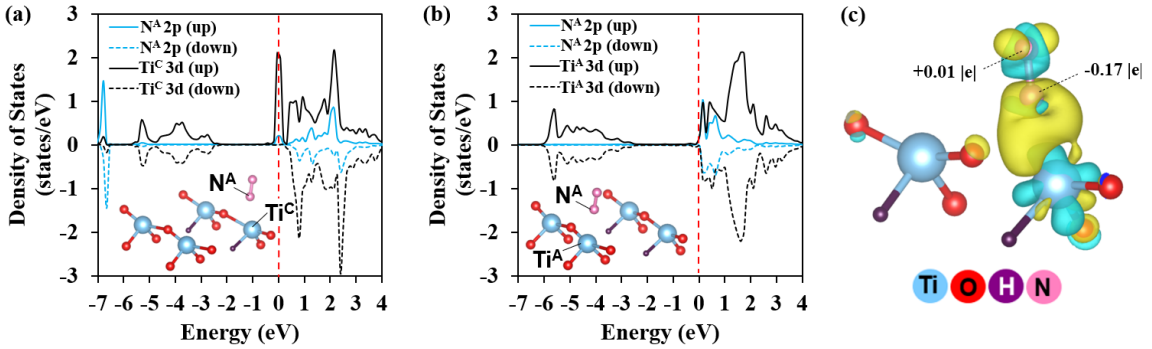

Figure 4.3 Local density of states of N_2 adsorbed BTOH (210)-Ti_2O_2: (a) on Ti^C; (b) on Ti^A. (c) Charge–density-difference plot of the N_2–Ti^C configuration: the yellow region represents charge accumulation, and the blue region charge depletion; the Bader charges on each N atom are also shown.

One can see greater orbital hybridization between N_2 and Ti^C than between N_2 and Ti^A. The charge-density difference plot and the Bader charges of N (Figure 4.3c) clearly show charge accumulation along the Ti–N bonding region, depleted from Ti and the far-end N atom.

4.4.3 Reaction mechanisms of ammonia synthesis on the BTOH (210)-Ti_2O_2 surface. During NH_3 synthesis, BTOH lattice hydrides can incorporate into the catalytic cycle. A previous study has shown this direct involvement of the mobile lattice hydrides

for NH_3 synthesis when deuterated NH_3 was initially produced over the $Ru/BaTiO_{2.4}D_{0.6}$ catalyst.[18] On the other hand, we found that H_2 readily dissociates across the surface Ti–O bond, as indicated by the relatively low barrier of 0.15 eV (Figure 4.4), thereby replenishing the surface H atoms used to hydrogenate N_2 to NH_3.

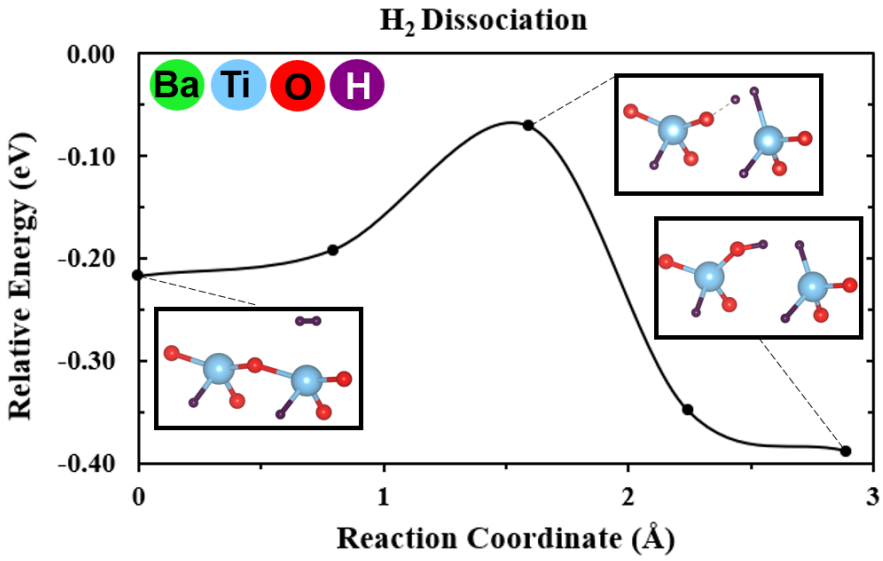

Figure 4.4 Minimum energy path of H_2 dissociation across the surface Ti^C-O bond and the structures for the initial, transition, and final states.

Here we considered two likely pathways for ammonia synthesis on the (210)-Ti_2O_2 surface termination of BTOH. Both pathways proceed first with H_2 adsorption and dissociation on the surface and then reduction of N_2 by either H_2-sourced surface H atoms or surface lattice hydrides followed by N–N cleavage. Figure 4.5 shows the mechanistic overview of the two pathways studied: (a) the distal pathway whereby H atoms hydrogenate N_2 to form the *N–NH_2 and *N–NH_3 key intermediates, followed by N–N bond breaking; (b) the alternating pathway whereby H atoms hydrogenate N_2 in an alternating fashion to form the

intermediates such as *NHNH, before N–N bond breaking, and formation of co-adsorbed *NH/*NH_2 and *NH_2/*NH_2 on the surface. The pathway starting with N_2 dissociation prior to H addition was not pursued because we found that dissociation of N_2 into two N atoms adsorbed on surface Ti sites is a highly uphill process (>6 eV; see Figure 4.6). Below we examine the two pathways in detail.

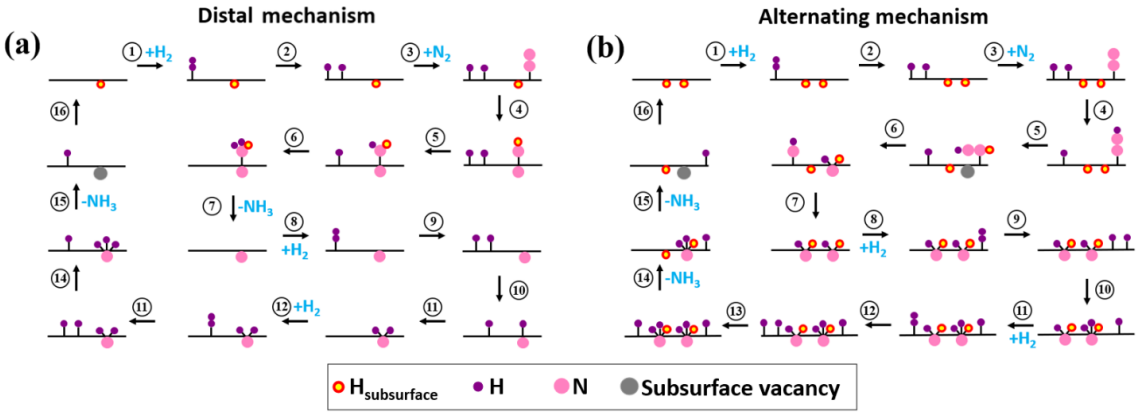

Figure 4.5 A mechanistic overview of (a) the distal and (b) alternating mechanisms for NH_3 synthesis over the BTOH (210)-Ti_2O_2 surface. The surface is represented as a horizontal black line and any atom below the line represents subsurface atoms.

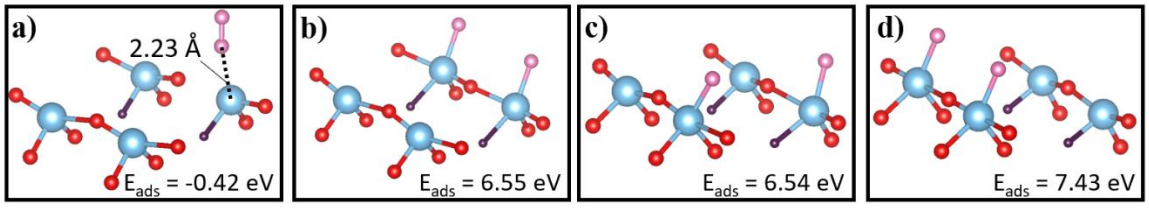

Figure 4.6 The structures of N_2 adsorbed on a surface Ti site (a) and of dissociated N_2 adsorbed on different surface Ti sites (b)-(d). The adsorption energies are listed on the bottom of each panel.

4.4.3.1 The distal pathway. Figure 4.7a shows the energy profiles of the key states involved in the formation of the two NH_3 molecules and Figure 4.7b shows the structures

of the key intermediates on the surface. Formation of the first NH_3 molecule starts with H_2 adsorption and then dissociation across the surface Ti^C–O^I bond (states 1 to 3). After N_2 adsorption on Ti^C (state 4), a subsurface lattice hydride hydrogenates $*N_2$ to *NNH (state 5), which subsequently moves to the hydride-vacancy site occupied previously by the subsurface lattice hydride (structure 5 in Figure 4.7b). We found that this configuration is the more stable one. (Alternatively, the hydride from H_2 dissociation can hydrogenate N_2, while the subsurface lattice hydride stays in place; this scenario is key to the alternating pathway that will be discussed in the next section.) In this configuration, the N–N bond length elongates to 1.30 Å from 1.11 Å of the gas phase N_2. From there, the two surface H atoms from H_2 consecutively hydrogenate *NNH to form $*NNH_2$ (state 6) and then $*NNH_3$ (state 7). Next, the N–N bond is cleaved, leaving a subsurface lattice nitride and an NH_3 molecule adsorbed on Ti^C (state 8). Local density-of-states (DOS) plots (Figure 4.8) show that state 8 has greater orbital hybridization between N 2p and Ti 3d than state 7, suggesting that state 8's much lower energy is contributed by both formation of a stable molecule (NH_3) and the stronger Ti–N interaction. Although it requires 1.5 eV in energy to desorb the NH_3 molecule from state 8, the free energy of NH_3 desorption is significantly lower at 0.28 eV after adding the favorable entropy contribution due to formation of a gaseous NH_3 molecule (state 9) at the reaction temperature.

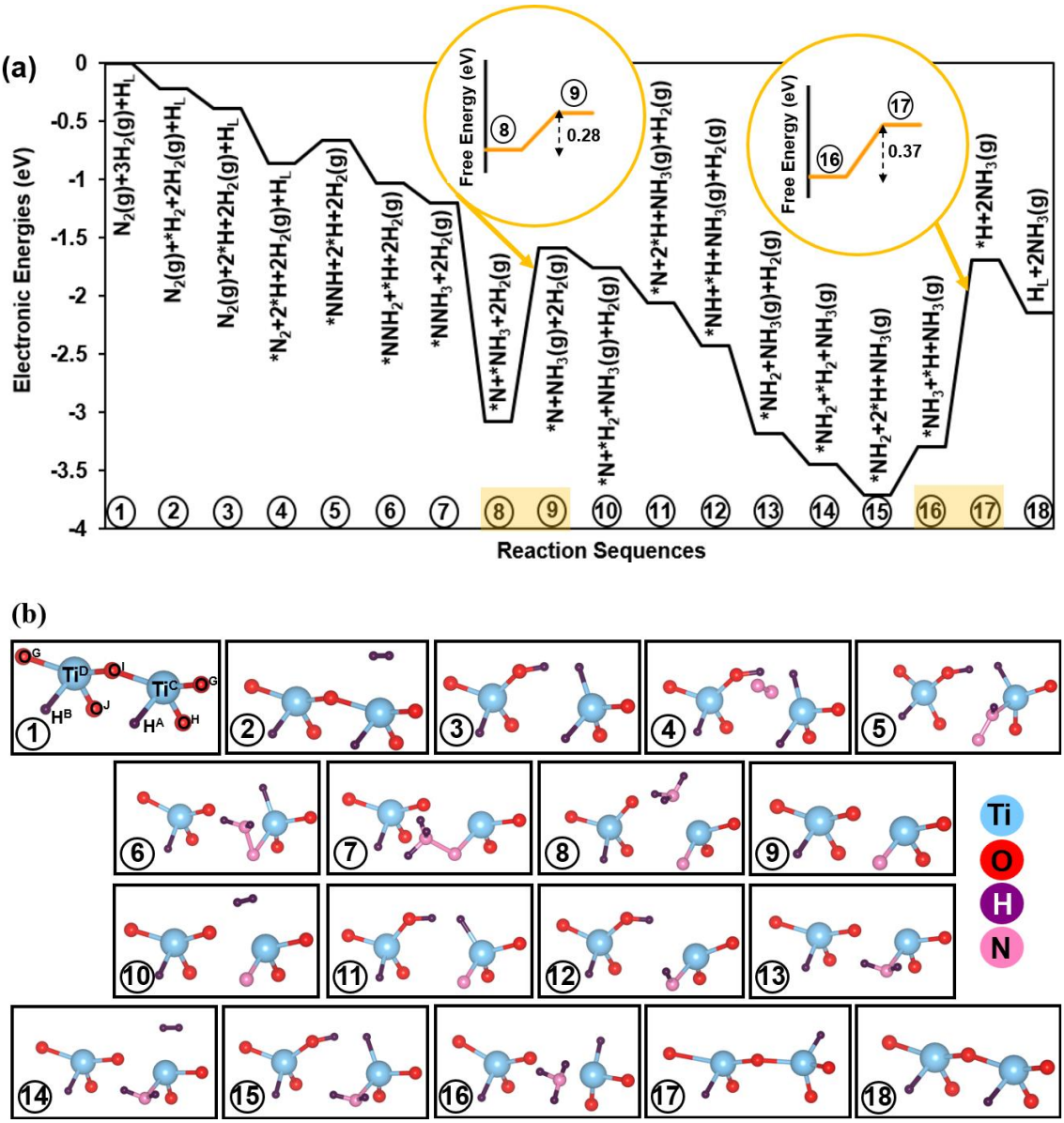

Figure 4.7 Formation of the two NH_3 molecules *via* the distal mechanism. Gaseous and adsorbed states are represented by (*g*) and *, respectively. The free energies of desorption of the 1st and 2nd NH_3 molecules (*i.e.* 0.28 and 0.37 eV, respectively) are shown in the orange bubbles in (a). All intermediate structures are shown in (b).

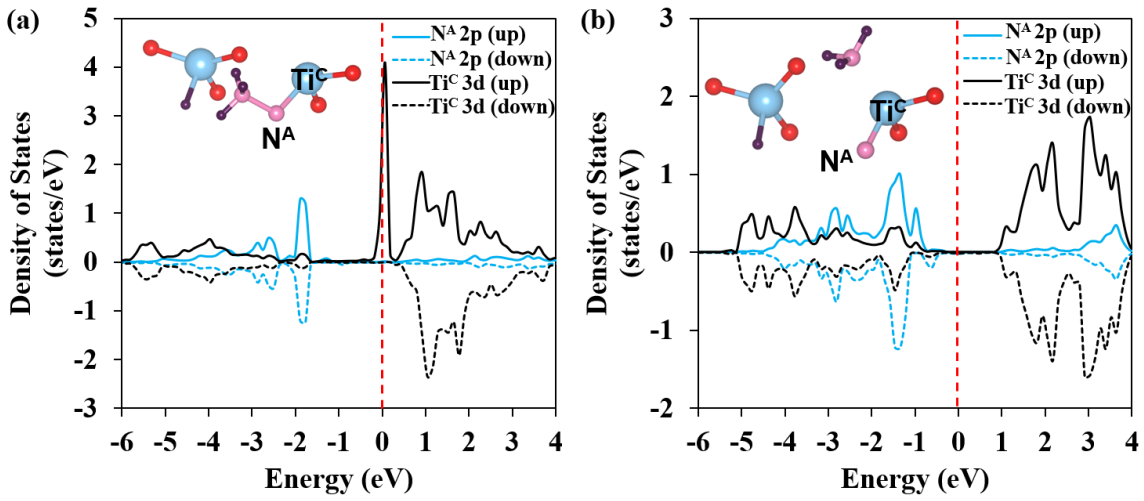

Figure 4.8 Local densities of states of state 7 (a) and state 8 (b) in the distal pathway.

In states 10-18, a second NH_3 molecule is formed by hydrogenating the subsurface lattice nitride in state 9 with three more surface H atoms from the dissociation of two H_2 molecules, while the fourth H atom is used to regenerate the surface lattice hydride site. The second adsorbed H_2 molecule is heterolytically cleaved across Ti^C and O^I (states 10 and 11). Next, H on Ti^C transfers to *N to form *NH (state 12) that is further hydrogenated to $*NH_2$ (state 13) by H on O^I. Then the third H_2 molecule adsorbs (state 14) and heterolytically cleaves across Ti^C and O^I atoms (state 15). Furthermore, H on O^I reacts with $*NH_2$ to form $*NH_3$ (state 16) with an uphill energy of 0.41 eV. The second NH_3 desorbs (state 17: ΔE = 1.61 eV; ΔG = 0.37 eV). Finally, the remaining H adsorbed on Ti^C rotates and fills the subsurface anion vacancy to regenerate the catalytic surface in state 18. Overall, two key factors are involved in the distal pathway: (i) the presence of surface Ti^C and O^I atoms to heterolytically cleave H_2 and generate surface H atoms that

hydrogenate *N_2; (ii) the hydride vacancy site to anchor N–NH after the hydride transfers to adsorbed N_2.

4.4.3.2 The alternating pathway. In this mechanism, both N atoms of N_2 are hydrogenated before N–N bond breaking. Figure 4.9 shows the energy profile and structures of key intermediates. The reaction starts with dissociative H_2 adsorption, followed by N_2 adsorption (states 1–4, same as in the distal pathway). The next step is different: instead of subsurface lattice hydride attacking N_2 as in the distal pathway, now the surface H atom bonded to Ti^C from H_2 dissociation first reacts with *N_2 to form *NNH (state 5). The *NNH intermediate is stabilized by bridging Ti^C and Ti^D sites (5 in Figure 4.9b). This is an important intermediate in the alternating pathway. Then, one of the subsurface lattice hydrides, H^A, hydrogenates the proximal N of *NNH to form the *NHNH species (state 6), still bridged by Ti^C and Ti^D. Next, the surface H bonded to O^I from H_2 dissociation transfers to *NHNH, leading to cleavage of the N–N bond and formation of co-adsorbed *NH_2 at the hydride-vacancy site and *NH on Ti^D (state 7). Subsequent addition of another subsurface lattice hydride, H^B, to *NH results in two *NH_2 groups occupying two subsurface hydride-vacancy sites (state 8).

Figure 4.9a shows that all the states (1 to 8) of N_2 reaction with two lattice hydrides and one molecule of dissociated H_2 to form 2 *NH_2 are downhill, especially from 7 to 8.

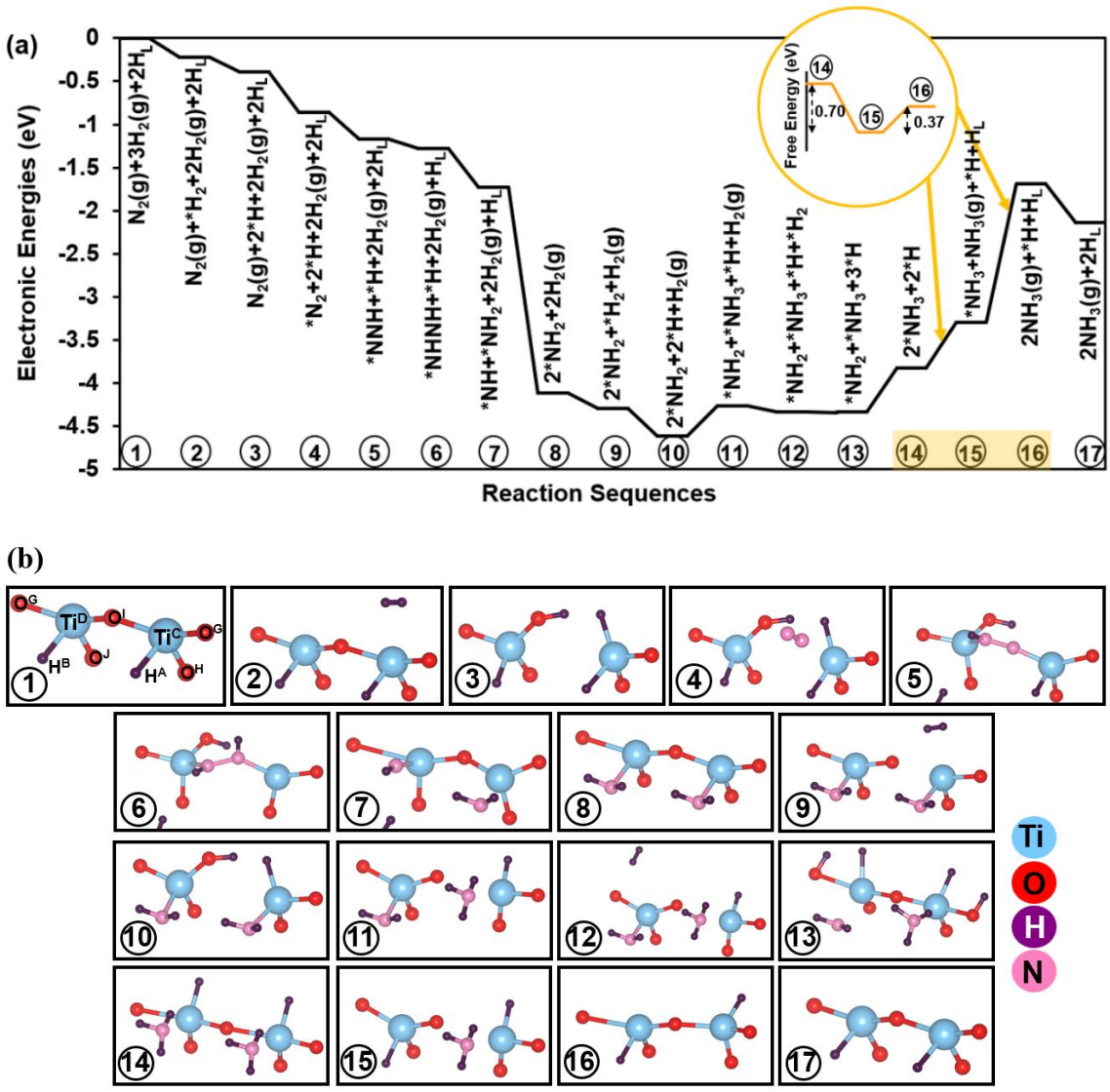

Figure 4.9 Formation of the two NH_3 molecules *via* the alternating mechanism (a). Gaseous and adsorbed states are represented by (*g*) and *, respectively. The free energies of desorption of the 1st and 2nd NH_3 molecules (*i.e.* −0.70 and 0.37 eV, respectively) are shown in the orange bubble in (a). All intermediate structures are shown in (b).

To understand the origin of this extra stability at state 8, we analyzed in detail the change in the local geometry from 7 to 8 (Figure 4.10). One distinct change is the Ti–O distances, especially the distances to the subsurface O atoms shortened from 1.90 and 1.85 Å

in Figure 4.10a to 1.78 and 1.79 Å in Figure 4.10b, respectively. In other words, after hydrogenation of *NH by the subsurface lattice hydride H^B to form two *NH_2 groups occupying two subsurface hydride-vacancy sites, the local bonding of the two surface Ti atoms is greatly strengthened, leading to a much more stable state.

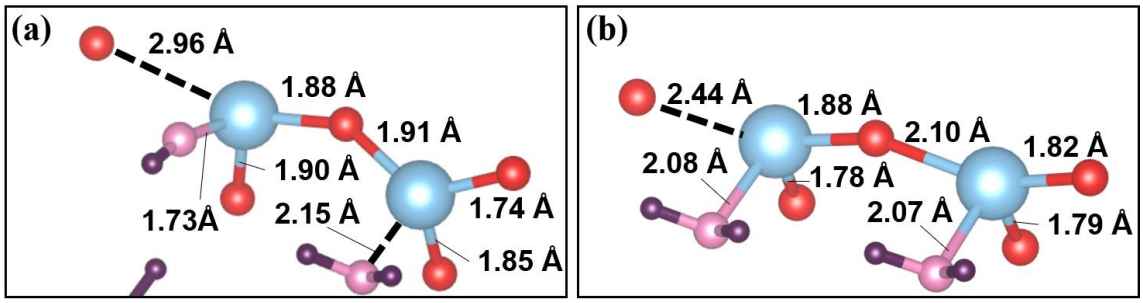

Figure 4.10 Local geometries in state 7 (a) and state 8 (b) of the alternating pathway.

In the subsequent states (9 to 17), two more molecules of H_2 adsorb and dissociate on the surface, generating four surface H atoms: two of them hydrogenate NH_2 to NH_3 while the other two regenerate the subsurface lattice hydrides. First, the second H_2 molecule adsorbs (state 9) and dissociates across the surface Ti^C–O^I bond (state 10) to replenish surface H atoms. Then, the surface H on the O^I site hydrogenates one *NH_2 to *NH_3 (state 11; slightly uphill by 0.36 eV). Next, dissociative adsorption of the third H_2 molecule takes place (states 12 and 13). Furthermore, the surface H on the O^G site hydrogenates the remaining *NH_2 to *NH_3 (state 14; uphill by 0.49 eV). The desorption of the first NH_3 molecule happens simultaneously with the H on Ti^D rotating to the subsurface hydride-vacancy site (state 15: ΔE = 0.52 eV; ΔG = −0.70 eV). The desorption of the

second NH_3 molecule is significantly more uphill (state 16, ΔE = 1.61 eV; ΔG = 0.37 eV). Finally, the remaining hydride adsorbed on Ti^C fills the subsurface vacancy in state 17.

4.4.3.3 Comparison of the two pathways. In comparing the distal and the alternating pathways, one can see that the crucial bifurcating point is how the first H atom is added to $*N_2$ to form *NNH (Figure 4.11 and 4.12): in the distal pathway, the first H is a subsurface lattice hydride and after hydrogenation the proximal N of *NNH is anchored at the anion-vacancy site; in the alternating pathway, the first H is from H_2 dissociation and the *NNH intermediate is bridged between two surface Ti sites. The two different sites for *NNH dictate the two subsequently different paths for N–N cleavage. Here we note that *NNH in the alternating pathway is 0.51 eV more stable (Figure 4.11). In the distal pathway, the state of $*NNH_3$ dissociating to *N and $*NH_3$ is most exothermic, while in the alternating pathway it is the hydrogenation of *NH to $*NH_2$. In both pathways, desorption of the NH_3 molecules is the most energetically uphill, especially the second one; but with the entropy gain in forming gaseous NH_3, the free-energy change is much less positive and can even turn negative in the case of the first NH_3 desorption in the alternative pathway. Given that the step of hydrogenating $*N_2$ to *NNH is uphill in the case of the distal pathway but downhill in the alternating pathway and that desorption of the first $*NH_3$ is much more uphill in the distal pathway than in the alternating pathway (Figure 4.12), we think that the alternating pathway is more favorable. On the other hand, as the distal pathway involves only one hydride/vacancy in the synthesis of ammonia, while the alternating pathway involves two adjacent hydrides/vacancies, it suggests that the distal pathway is more likely

to happen on $BaTiO_{3-x}H_x$ for smaller *x*-values, while the alternating pathway for larger *x* values.

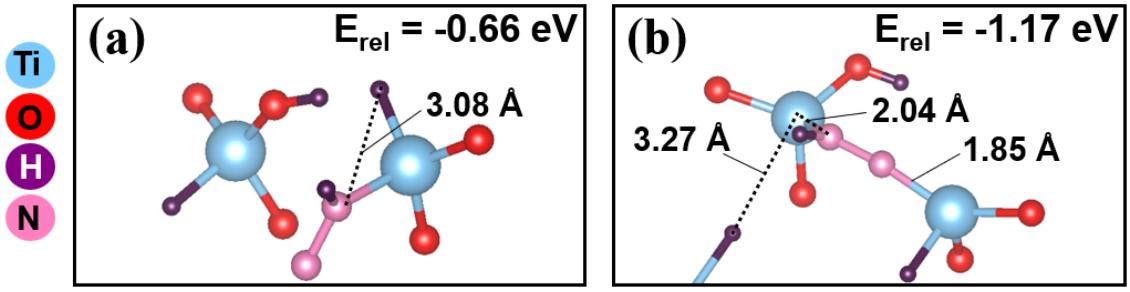

Figure 4.11 Comparison of the two *NNH intermediates: (a) state 5 in the distal pathway (Figure 4.7), formed from reaction with a subsurface lattice hydride and adsorbed at the subsurface anion vacancy; (b) state 5 in the alternating pathway (Figure 4.9), formed from reaction with a surface hydride (from H2 dissociation) and adsorbed on a surface Ti site.

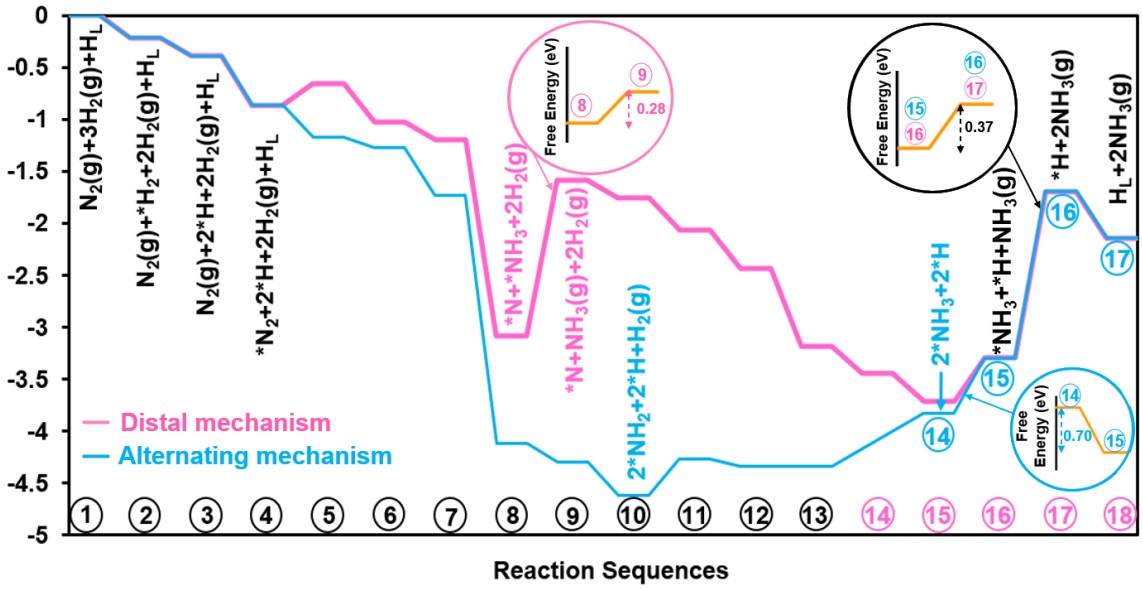

Figure 4.12 Comparison of the energy profiles of the distal and alternating pathways. The intermediate states shared by the two pathways are labeled in black (in the beginning and the end).

4.4.4 Experimental implications. As Ti is an early transition metal, it bonds strongly with N, making metallic Ti unsuitable for catalytic ammonia synthesis. However, Kobayashi *et al.* have shown that powdered samples of BTOH exhibited catalytic activity for NH_3 synthesis, thus suggesting that catalysts containing Ti and H could weaken the strong Ti–N bond.[31] As a way to explain the potential Ti–N bond weakening by Ti–H-containing catalysts, they performed DFT calculations of N_2 adsorption over the following Ti-terminated surfaces: Ti(001), TiN(111), and TiH_2(111); their results showed that indirect electronic effects from the lattice hydride were not enough to explain the activity observed. Our results above suggest that both lattice hydrides and hydride vacancies are influential in the synthesis of NH_3 rather than only the mere presence of lattice hydrides in BTOH. From Figure 4.7 and 4.9, one can see that in both the distal and alternating pathways for NH_3 synthesis, lattice hydrides provide a source of H atoms for N_2 hydrogenation and the resulting vacancies are needed for the eventual cleavage of the N–N bond.

Future experimental work using inelastic neutron scattering (INS) would be necessary to identify different H species on the BTOH surface and determine which H species are consumed for hydrogenation of N_2, while quasielastic neutron scattering can be used to study dynamics of hydrides in the lattice as done recently for layered oxyhydride $SrVO_2H$.[39] Further experimental work using operando IR spectroscopy can help differentiate the two mechanisms by identifying the vibrational signatures of key intermediate structures in the alternating and distal mechanisms.

Using first principles DFT methods to investigate NH_3 synthesis mechanisms over a metal catalyst supported on BTOH is also an exciting next step. An experimental study has shown that Ru, Co, or Fe loaded on a $BaTiO_{3-x}H_x$ support exhibited higher activity than the metal catalysts supported on $BaTiO_3$.[18] The study proposes that the higher activity exhibited on $Ru/BaTiO_{3-x}H_x$ was likely due to hydrogen spillover, thus preventing H_2 poisoning on Ru, while the activity of Fe or $Co/BaTiO_{3-x}H_x$ was possibly due to electron donation from H^- to Fe or Co, which assists in N_2 activation. It would be interesting to verify these proposed pathways *via* DFT.

4.5 Conclusion

Using first principles DFT methods, we have investigated NH_3 synthesis pathways on the (210)-Ti_2O_2 surface termination of $BaTiO_{2.5}H_{0.5}$ (BTOH) in order to understand the role of lattice hydrides in the perovskite oxyhydride's surface chemistry. We found that N_2 prefers to adsorb on the more reduced surface Ti atom, which is bonded to a subsurface lattice hydride, while heterolytically dissociative H_2 adsorption is also facile on the surface. Then, two mechanistic hypotheses have been examined for hydrogenation of adsorbed N_2: (a) the distal pathway whereby H atoms hydrogenate N_2 to form the $*N–NH_2$ and $*N–NH_3$ key intermediates, followed by N–N bond breaking; (b) the alternating pathway whereby H atoms hydrogenate N_2 in an alternating fashion to form intermediates such as *NHNH, before N–N bond breaking and formation of co-adsorbed $*NH/NH_2$ and $*NH_2/*NH_2$ on the surface. In the distal pathway, the subsurface hydride vacancy from reaction of $*N_2$ with the lattice hydride was found to be key to breaking the $*N–NH_3$ bond and leading to surface nitride formation. In the alternating pathway, the neighboring

surface Ti sites are key to bridging and stabilizing the *NNH intermediate. In both pathways, the hydrogenation steps are generally downhill in energy and desorption of NH_3 is the most uphill. Overall, the alternating pathway is more favorable, especially when lattice hydrides are abundant on the surface. Our results shed light on the role of surface lattice hydrides and their vacancies in hydrogenation of N_2 over BTOH, which could be useful in understanding catalytic hydrogenation on perovskite oxyhydrides in general.

4.6 References

(1) Grant, J. T.; Venegas, J. M.; McDermott, W. P.; Hermans, I. Aerobic oxidations of light alkanes over solid metal oxide catalysts. *Chem. Rev.*, **2018**, 118, 2769–2815.

(2) Hwang, J.; Rao, R. R.; Giordano, L.; Katayama, Y.; Yu, Y.; Shao-Horn, Y. Perovskites in catalysis and electrocatalysis. *Science*, **2017**, 358, 751–756.

(3) Chen, S.; Takata, T.; Domen, K. Particulate photocatalysts for overall water splitting. *Nat. Rev. Mater*., **2017**, 2, 17050.

(4) Tsounis, C.; Wang, Y.; Arandiyan, H.; Wong, R. J.; Toe, C. Y.; Amal, R.; Scott, J. Tuning the Selectivity of $LaNiO_3$ Perovskites for CO_2 Hydrogenation through Potassium Substitution, *Catalysts*, **2020**, 10, 409.

(5) Kobayashi, Y.; Hernandez, O. J.; Sakaguchi, T.; Yajima, T.; Roisnel, T.; Tsujimoto, Y.; Morita, M.; Noda, Y.; Mogami, Y.; Kitada, A.; Ohkura, M.; Hosokawa, S.; Li, Z.; Hayashi, K.; Kusano, Y.; Kim, J.; Tsuji, N.; Fujiwara, A.; Matsushita, Y.; Yoshimura, K.; Takegoshi, K.; Inoue, M.; Takano, M.; Kageyama, H. An oxyhydride of $BaTiO_3$ exhibiting hydride exchange and electronic conductivity. *Nat. Mater.*, **2012**, 11, 507–511.

(6) Tang, Y.; Kobayashi, Y.; Shitara, K.; Konishi, A.; Kuwabara, A.; Nakashima, T.; Tassel, C.; Yamamoto, T.; Kageyama, H. On hydride diffusion in transition metal perovskite oxyhydrides investigated via deuterium exchange. *Chem. Mater.*, **2017**, 29, 8187–8194.

(7) Sakaguchi, T.; Kobayashi, Y.; Yajima, T.; Ohkura, M.; Tassel, C.; Takeiri, F.; Mitsuoka, S.; Ohkubo, H.; Yamamoto, T.; Kim, J.; Tsuji, N.; Fujihara, A.; Matsushita, Y.; Hester, J.; Avdeev, M.; Ohoyama, K.; Kageyama, H. Oxyhydrides of (Ca, Sr, Ba)TiO_3 Perovskite Solid Solutions. *Inorg. Chem.*, **2012**, 51, 11371–11376.

(8) Brice, J. F.; Moreau, A. Synthese et conductivite anionique des hydruro-oxydes de lanthane de formule LaHO, $LaH_{1+2x}O_{1-x}$ et $LaH_{1+y}O_{1-x}$ (y < 2SC). *Ann. Chim.*, **1982**, 7, 623–634.
(9) Huang, B.; Corbett, J. D. Ba_3AlO_4H: synthesis and structure of a new hydrogen-stabilized phase. *J. Solid State Chem.*, **1998**, 141, 570–575.
(10) Huang, B.; Corbett, J. D. $Ba_{21}Ge_2O_5H_{24}$ and Related Phases. A Corrected Structure Type and Composition for a Zintl Phase Stabilized by Hydrogen. *Inorg. Chem.*, **1998**, 37, 1892–1899.
(11) Hayward, M. A.; Cussen, E. J.; Claridge, J. B.; Bieringer, M.; Rosseinsky, M. J.; Kiely, C. J.; Blundell, S. J.; Marshall, I. M.; Pratt, F. L. The Hydride Anion in an Extended Transition Metal Oxide Array: $LaSrCoO_3H_{0.7}$. *Science*, **2002**, 295, 1882–1884.
(12) Goto, Y.; Tassel, C.; Noda, Y.; Hernandez, O.; Pickard, C. J.; Green, M. A.; Sakaebe, H.; Taguchi, N.; Uchimoto, Y.; Kobayashi, Y.; Kageyama, H. Pressure-Stabilized Cubic Perovskite Oxyhydride $BaScO_2H$. *Inorg. Chem.*, **2017**, 56, 4840–4845.
(13) Bang, J.; Matsuishi, S.; Hiraka, H.; Fujisaki, F.; Otomo, T.; Maki, S.; Yamaura, J.; Kumai, R.; Murakami, Y.; Hosono, H. Hydrogen Ordering and New Polymorph of Layered Perovskite Oxyhydrides: $Sr_2VO_{4-x}H_x$. *J. Am. Chem. Soc.*, **2014**, 136, 7221–7224.
(14) Romero, F. D.; Leach, A.; Möller, J. S.; Foronda, F.; Blundell, S. J.; Hayward, M. A. Strontium Vanadium Oxide-Hydrides: "Square-Planar" Two-Electron Phases. *Angew. Chem., Int. Ed.*, **2014**, 53, 7556–7559.
(15) Tassel, C.; Goto, Y.; Kuno, Y.; Hester, J.; Green, M.; Kobayashi, Y.; Kageyama, H. Direct synthesis of chromium perovskite oxyhydride with a high magnetic-transition temperature. *Angew. Chem.*, **2014**, 126, 10545–10548.
(16) Tassel, C.; Goto, Y.; Watabe, D.; Tang, Y.; Lu, H.; Kuno, Y.; Takeiri, F.; Yamamoto, T.; Brown, C. M.; Hester, J.; Kobayashi, Y.; Kageyama, H. High-pressure synthesis of manganese oxyhydride with partial anion order. *Angew. Chem., Int. Ed.*, **2016**, 55, 9667–9670.
(17) Tang, Y.; Kobayashi, Y.; Tassel, C.; Yamamoto, T.; Kageyama, H. Hydride-Enhanced CO_2 Methanation: Water-Stable $BaTiO_{2.4}H_{0.6}$ as a New Support. *Adv. Energy Mater.*, **2018**, 8, 1800800.
(18) Tang, Y.; Kobayashi, Y.; Masuda, N.; Uchida, Y.; Okamoto, H.; Kageyama, T.; Hosokawa, S.; Loyer, F.; Mitsuhara, K.;Yamanaka, K.; Tamenori, Y.; Tassel, C.; Yamamoto, T.; Tanaka, T.; Kageyama, H. Metal-Dependent Support Effects of Oxyhydride-Supported Ru, Fe, Co Catalysts for Ammonia Synthesis. *Adv. Energy Mater.*, **2018**, 8, 1801772.
(19) M. Appl, Ammonia, 1. Introduction, Ullmann's Encyclopedia of Industrial Chemistry, 2011, DOI: 10.1002/14356007.a02_143.pub3.
(20) Zhang, J.; Gou, G.; Pan, B. Study of Phase Stability and Hydride Diffusion Mechanism of $BaTiO_3$ Oxyhydride from First-Principles. *J. Phys. Chem. C*, **2014**, 118, 17254–17259.

(21) Eklöf-Österberg, C.; Nedumkandathil, R.; Häussermann, U.; Jaworski, A.; Pell, A. J.; Tyagi, M.; Jalarvo, N. H.; Frick, B.; Faraone, A.; Karlsson, M. J. Dynamics of Hydride Ions in Metal Hydride-Reduced $BaTiO_3$ Samples Investigated with Quasielastic Neutron Scattering. *Phys. Chem. C*, **2019**, 123, 2019–2030.
(22) Kobayashi, Y.; Hernandez, O.; Tassel, C.; Kageyama, H. New chemistry of transition metal oxyhydrides. *Sci. Technol. Adv. Mater.*, **2017**, 18, 905–918.
(23) Kitano, M.; Kujirai, J.; Ogasawara, K.; Matsuishi, S.; Tada, T.; Abe, H.; Niwa, Y.; Hosono, H. Low-temperature synthesis of perovskite oxynitride-hydrides as ammonia synthesis catalysts. *J. Am. Chem. Soc.*, **2019**, 141, 20344–20353.
(24) Kresse, G.; Furthmüller, J. Efficient iterative schemes for *ab initio* total-energy calculations using a plane-wave basis set. *J. Comput. Mater. Sci.*, **1996**, 6, 15–50.
(25) Kresse, G.; Furthmüller, J. Efficient Iterative Schemes for Ab Initio Total-Energy Calculations Using a Plane-Wave Basis Set. *Phys. Rev. B: Condens. Matter Mater. Phys.* **1996**, 54, 11169-11186.
(26) Perdew, J. P.; Burke, K.; Ernzerhof, M. Generalized Gradient Approximation Made Simple. *Phys. Rev. Lett.* **1996**, 77, 3865.
(27) Blöchl, P. E. Projector Augmented-Wave Method. *Phys. Rev. B: Condens. Matter Mater. Phys.* **1994**, 50, 17953-17979.
(28) Grimme, S.; Antony, J.; Ehrlich, S.; Krieg, H. A consistent and accurate *ab initio* parametrization of density functional dispersion correction (DFT-D) for the 94 elements H-Pu. *J. Chem. Phys.*, **2010**, 132, 154104.
(29) Tang, W.; Sanville, E.; Henkelman, G. A grid-based Bader analysis algorithm without lattice bias. *J. Phys.: Condens. Matter* **2009**, 21, 084204.
(30) Wang, K.; Fung, V.; Wu, Z.; Jiang, D.-E. Stable Surface Terminations of a Perovskite Oxyhydride from First-Principles. *J. Phys. Chem. C*, **2020**, 124, 18557–18563.
(31) Kobayashi, Y.; Tang, Y.; Kageyama, T.; Yamashita, H.; Masuda, N.; Hosokawa, S.; Kageyama, H. Titanium-Based Hydrides as Heterogeneous Catalysts for Ammonia Synthesis. *J. Am. Chem. Soc.* **2017**, 139, 18240-18246.
(32) Wang, Y.; Cheng, J.; Behtash, M.; Tang, W.; Luo, J.; Yang, K. First-principles studies of polar perovskite $KTaO_3$ surfaces: structural reconstruction, charge compensation, and stability diagram. *Phys. Chem. Chem. Phys.* **2018**, 20, 18515-18527.
(33) Monkhorst, H. J.; Pack, J. D. Special points for Brillouin-zone integrations. *Phys. Rev. B: Solid State* **1976**, 13, 5188-5192.
(34) Neugebauer, J.; Scheffler, M. Adsorbate-substrate and adsorbate-adsorbate interactions of Na and K adlayers on Al (111). *Phys. Rev. B: Condens. Matter Mater. Phys.*, **1992**, 46, 16067–16080.
(35) Henkelman, G.; Uberuaga, B. P.; Jonsson, H. A climbing image nudged elastic band method for finding saddle points and minimum energy paths. *J. Chem. Phys.*, **2000**, 113, 9901.
(36) Savara, A. Standard states for adsorption on solid surfaces: 2D gases, surface liquids, and Langmuir adsorbates. *J. Phys. Chem. C*, **2013**, 117, 15710–15715.

(37) Bouilly, G.; Yajima, T.; Terashima, T.; Yoshimune, W.; Nakano, K.; Tassel, C.; Kususe, Y.; Fujita, K.; Tanaka, K.; Yamamoto, T.; Kobayashi, Y.; Kageyama, H. Electrical Properties of Epitaxial Thin Films of Oxyhydrides $ATiO_{3-x}H_x$ (A = Ba and Sr). *Chem. Mater.* **2015**, 27, 6354-6359.
(38) Shaver, M. P.; Fryzuk, M. D. Activation of Molecular Nitrogen: Coordination, Cleavage and Functionalization of N_2 Mediated By Metal Complexes. *Adv. Synth. Catal.*, **2003**, 345, 1061–1076.
(39) Lavén, R.; Häussermann, U.; Perrichon, A.; Andersson, M. S.; Targama, M. S.; Demmel, F.; Karlsson, M. Diffusional Dynamics of Hydride Ions in the Layered Oxyhydride $SrVO_2H$. *Chem. Mater.*, **2021**, 33, 2967–2975.

4.7 Appendix

4.A1 Details of the thermodynamic calculations

The change in Gibbs free energy corresponding to NH_3 desorption (ΔG_{des}) from the surface was approximated using the following equation

$$\Delta G_{des} = \Delta H_{des} - T\Delta S_{des} \approx (\Delta E_{elec} + \Delta E_{vib}) - T\Delta S_{des} \quad (4.A1)$$

where ΔE_{elec} is the change in electronic energy, ΔE_{vib} is the change in vibrational energy, T is temperature at 673 K, and ΔS_{des} is the change in entropy between the adsorbed state (initial state) and the desorbed state (final state). In this work, we approximated that the rotational and vibrational entropic contributions are much less than the translational entropic contribution such that

$$\Delta S_{des} = S_{NH_3} - S_{NH_3{}^*} = S_{NH_3} - \left(S_{NH_3} - S_{NH_3,trans}\right) = S_{NH_3,trans} \quad (4.A2)$$

where S_{NH3} is the total entropy of gaseous NH_3, S_{NH3*} is the total entropy of adsorbed NH_3, and $S_{NH3,trans}$ is the translational entropy of gaseous NH_3. The equation used to calculate E_{vib} in Equation 4.A1 is

$$E_{vib} = \sum_i \{\frac{hv_i}{2} + \frac{hv_i e^{\frac{-hv_i}{kT}}}{1-e^{\frac{-hv_i}{kT}}}\} \quad (4.A3)$$

where h is the Planck's constant, v_i is the vibrational frequency of mode *i*, T is the temperature at 673 K, and k is the Boltzmann constant. The Sackur-Tetrode equation[1] was used to calculate $S_{NH3,trans}$ which approximately equals to ΔS_{des}

$$\Delta S_{des} \approx S_{NH_3,trans} = Rln\left(\left(\frac{\sqrt{2\pi mkT}}{h}\right)^D \frac{L^D}{nN_A}\right) + \left(1+\frac{D}{2}\right) R \quad (4.A4)$$

where R is the ideal gas constant, m is the molecular mass of NH_3, D is the number of dimensions NH_3 gas is confined to, L is the length of the box NH_3 is confined to, n is the total number of moles, and N_A is Avogadro's number. In this work, D = 3 such that L^D gives the volume of the box in which NH_3 is confined. The value of L was calculated by first solving for the volume (V) of the box using the ideal gas equation (PV = nRT), where P = 1 bar, and then taking the cube root of V. The value of n was set to 1.

4.A2 References

(1) Savara, A. Standard States for Adsorption on Solid Surfaces: 2D Gases, Surface Liquids, and Langmuir Adsorbates. *J. Phys. Chem. C* **2013**, 117, 15710-15715.

CHAPTER 5

Catalytic acetylene semi-hydrogenation on perovskite oxyhydride: Insights from first principles and microkinetic modeling

5.1 Abstract

Perovskite oxyhydrides (POHs) belong to a new class of mixed-anion system that has shown promise as both a catalyst and a support in hydrogenation reactions such as ammonia synthesis. But it is unknown if they have the potential to efficiently catalyze alkyne semi-hydrogenation. Here, we use first-principles density functional theory, coupled with microkinetic modeling, to investigate acetylene semi-hydrogenation on a prototypical POH, $BaTiO_{2.5}H_{0.5}$ (BTOH). Both Horiuti-Polanyi and lattice hydride mechanisms are examined, based on a representative surface of BTOH under the reaction conditions. In the Horiuti-Polanyi mechanism, H_2 first heterolytically dissociates on the surface after which the resulting surface H atoms are then sequentially added to acetylene. In the lattice hydride mechanism, two lattice hydrides from the BTOH surface hydrogenate acetylene first after which the lattice hydrides are regenerated from H_2 re-filling the two lattice-hydride vacancies. Using density functional theory (DFT), we have mapped out minimum-energy pathways for these two mechanisms in hydrogenation of acetylene to ethylene, as well as further to ethane. Microkinetic modeling based on the DFT energies and barriers indicates that at 523 K, hydrogenation to ethylene and ethane via the Horiuti-Polanyi mechanism occurs at a rate up to two orders of magnitude faster than via the lattice hydride mechanism. Furthermore, a selectivity analysis for the temperature range of 373 – 673 K shows that the product observed is essentially only ethylene within the more active

Horiuti-Polanyi mechanism. Therefore, our simulations suggest that BTOH can selectively hydrogenate acetylene to ethylene with a high selectivity at a temperature range of 373 – 673 K and a total system pressure of 1.1 bar. This is because the steady-state surface structure containing surface anion vacancies can facilitate H_2 dissociation and help stabilize a vinyl intermediate. The present findings suggest that BTOH and other POH materials may be potential catalysts for selective hydrogenation such as alkyne semi-hydrogenation.

5.2 Introduction

Perovskite oxyhydrides (POHs) are a type of mixed-anion material derived from the ABO_3-type perovskite in which a small percentage of the solid's lattice O^{2-} are replaced by H^- upon reduction.[1,2,3] They have lately been of interest in catalysis due to their high anion exchangeability,[4,5,6] lattice hydride mobility,[1,2,3,7,8] and electronic conductivity, which play various roles in catalysis. $BaTiO_{3-x}H_x$ was one of the first prepared and most studied POHs. It was found that when $BaTiO_{3-x}H_x$ is used as a catalyst support instead of $BaTiO_3$, the catalytic activity of CO_2 methanation and ammonia synthesis increased.[9,10] This enhanced activity was attributed to the transfer of charges to the metal centers, the participation of lattice hydrides in the catalytic cycle as well as the prevention of hydrogen-poisoning on the metal catalysts.[9,10] Furthermore, $BaTiO_{3-x}H_x$ (with $x = 0.5$) exhibited activity for ammonia synthesis[11] at conditions that are milder (i.e. 400 ^oC, 5 MPa) than the Haber-Bosch conditions over an iron-based catalyst.[12]

Although the studies above have shown the advantages of using POHs in hydrogenation reactions, there have been no published studies on their utilization in alkyne semi-hydrogenation. Alkyne semi-hydrogenation is a key reaction useful in the polymer

and fine chemical industries.[13] Perhaps one of the most important reactions is the semi-hydrogenation of acetylene to ethylene as a means to purify ethylene streams for ethylene polymerization. In order to maximize the amount of ethylene in the feed, it is crucial for the participating catalyst to avoid the over-hydrogenation of ethylene to form ethane and to prevent the oligomerization of acetylene to form higher molecular weight compounds. Currently, Pd-Ag catalysts are the most widely used industrial catalysts for acetylene semi-hydrogenation.[14] This is because in the presence of Ag, the energy required to desorb ethylene is lower than the activation energy for further hydrogenation of ethylene to ethane, thus making the catalyst selective.[15] On the other hand, researchers have been actively searching for cheaper and more naturally abundant catalysts for alkyne semi-hydrogenation as alternatives to the noble metal-based Pd-Ag catalyst.[16,17,18]

Recent studies have shown that some metal oxides are highly selective for the semi-hydrogenation of acetylene.[19,20,21] For instance, ceria exhibited high acetylene conversion and ethylene selectivity at ambient pressure,[20] which was correlated with the absence of oxygen vacancies as the surface oxygen is crucial in stabilizing the active surface hydrogen proposed. However, a more recent study showed that hydride species on a moderately reduced ceria may play an active role in the hydrogenation of acetylene to ethylene.[22] This involvement of hydride in selective hydrogenation and H_2 activation on an oxide surface could be a general phenomenon.[23,45]

In POHs, the surfaces naturally expose hydride sites or have hydride vacancies, which may present interesting mechanisms in hydrogenation reactions, especially for selective hydrogenation. To this end, we aim to investigate the role of lattice hydrides in

POHs for acetylene semi-hydrogenation. As a prototypical POH, $BaTiO_{2.5}H_{0.5}$ (BTOH) is our choice of system. Under realistic acetylene semi-hydrogenation conditions,[20] the Ba_2O_4H termination of the BTOH (211) surface was determined to be the most stable.[24] Therefore, here we choose this termination as our surface model for both first principles and microkinetic analyses to investigate the potential of BTOH for acetylene semi-hydrogenation.

5.3 Computational Methods

5.3.1 First principles calculations. The Vienna *ab initio* Simulation Package (VASP)[25,26] was used to perform spin-polarized density functional theory (DFT) calculations from first principles. The Perdew-Burke-Ernzerhof (PBE) form of the generalized-gradient approximation (GGA) was used to treat the electron exchange and correlation[27] and the electron-core interactions were described by the projector augmented-wave (PAW) potentials.[28] A kinetic energy cutoff of 450 eV was used for the planewave basis set and the van der Waals interactions were accounted for with the DFT-D3 method.[29] The convergence criteria for force and energy were 0.02 eV/Å and 10^{-5} eV, respectively. Bader charge analysis was used to obtain the partial atomic charges.[30]

The BTOH (211)-Ba_2O_4H surface termination was used as the surface model for this mechanistic study as it was determined to be the most stable termination[24] under acetylene semi-hydrogenation conditions (i.e., 523 K, P_{total} = 1 bar).[20] A 2×2 supercell of the (211)-Ba_2O_4H slab, cleaved from the BTOH bulk,[24] contains a total of eight layers for a total of 78 atoms, with the bottom four layers fixed in their bulk positions. A vacuum layer of 15 Å was added to the surface slab along the z direction. The Brillouin zone was

sampled using a 3×3×1 Monkhorst-Pack scheme.[31] A dipole correction[32] was included within the vacuum region in order to compensate the net dipole moment along the surface normal due to slab asymmetry.

Adsorption energies were calculated using the equation $E_{ads} = E_{surface+adsorbate} - (E_{surface} + E_{adsorbate})$, where $E_{surface+adsorbate}$, $E_{surface}$, and $E_{adsorbate}$ are the energies of the adsorbate-slab system (adsorbates are either a reactant, intermediate, or product), the clean surface, and the isolated adsorbate molecules. The energies of the isolated molecules (H_2, C_2H_2, C_2H_4, and C_2H_6) were computed by placing each adsorbate in a cubic cell with a 15 Å wide vacuum in each direction. Transition states were searched for using both the climbing-image nudged elastic band (CI-NEB)[33] and the dimer method[34] with a force convergence criterion set to 0.05 eV/Å. Transition states were confirmed to be a rank-1 saddle point by calculating its frequencies using the finite difference method. The corresponding vibrations were used to compute the zero-point energy (ZPE) corrections for all adsorbed species and transition states as well as the vibrational partition functions for adsorbed reactant molecules.

5.3.2 Microkinetic modeling. The MKMCXX code[35] was used for microkinetic modeling,[36,37,38] to gain information on the kinetic properties for acetylene semi-hydrogenation over a BTOH surface. Specifically, the reaction rate, rate-controlling step(s), surface coverage and selectivity analysis were investigated to understand BTOH selectivity for ethylene. All elementary reaction steps within the Horiuti-Polanyi and lattice hydride mechanisms are listed in Tables A3 and A4 of the Appendix (section 5.7) along with the corresponding forward and reverse energy barriers. The possibility of surface re-

adsorption for all gaseous species (i.e., H_2, C_2H_2, C_2H_4, C_2H_6) were considered. For surface reactions, the pre-exponential factor is mainly dependent on the k_bT/h term such that the forward and reverse rate constants are calculated according to the equation $k = \frac{k_bT}{h}\exp\left(\frac{-\Delta E_{act}^{ZPE}}{k_bT}\right)$ where k_b is the Boltzmann constant, T is temperature, h is the Planck's constant, and ΔE_{act}^{ZPE} is the ZPE corrected enthalpy difference between the transition state and the initial or final state.

For adsorption reactions, processes are treated as non-activated with the rate constants and rates per site expressed as $k_{ads} = \frac{S}{\sqrt{2\pi m k_bT}} / \sigma_s$ and $r_{ads} = Pk_{ads}(1-\theta)$, where P is the gas pressure (typically in bar), σ_s is the site density (typically in sites per m^2), m is the mass of the molecule (typically in kg), S is the sticking coefficient which has a default value of 1, and θ is the total relative coverage for that site type. S was assumed to be 1 for all adsorption reactions. Each adsorption site surface area, A, was approximated to be 1.41×10^{-19} m^2 which equates to one eighth of the 2×2 BTOH supercell of dimensions 9.87 Å × 11.40 Å. Using the relationship $K_{eq} = k_{ads}/k_{des}$, the rate constant for desorption (k_{des}) can then be described as[39]

$$k_{des} = \frac{k_{ads}}{K_{eq}^{\circ}} * \frac{1/\theta^{\circ}}{(1/(1-\theta^{\circ}))(1/P^{\circ})} = \frac{1-\theta^{\circ}}{\theta^{\circ}}\left(\frac{AP^{\circ}}{\sqrt{2\pi m k_bT}}S\right)\frac{\exp\left(\frac{S_{gas}^{\circ}}{R}\right)}{q_{ads}}\exp\left(\frac{\Delta H_{ads}{}^{\circ} - H_{gas}^{\circ\,298.15\rightarrow T}}{RT}\right),$$

where $S_{gas}{}^{\circ}$ and $H_{gas}^{\circ\,298.15\rightarrow T}$ were calculated from thermodynamic tables[40] using the Shomate equation.[41] The standard states used were as described previously such that the surface standard states cancel in the above expression.[42] The total partition function of an adsorbed reactant molecule (q_{ads}) is a product of each of the individual partition functions from electronic, vibrational, rotational, and translational motion such that $q_{ads} =$

$q_{el}q_{vib}q_{rot}q_{trans}$, where q_{el} is often assumed to be 1. As adsorbates have hindered translational and rotational motions parallel to the surface, hindered motion equations[43] are used to approximate for q_{rot} and q_{trans} in this work while q_{vib} was calculated according to the equation $q_{vib} = \prod_i \frac{1}{1-\exp\left(-\frac{\varepsilon_i}{k_b T}\right)}$. Section 5.A1 and Tables 5.A1 and 5.A2 of the Appendix (section 5.7) provide details on how q_{rot} and q_{trans} were calculated for H_2, C_2H_2, C_2H_4, and C_2H_6.

The degree at which an elementary step controls the overall rate of the reaction is analyzed by the degree of rate control (DRC) method.[44,45] For elementary step *i*, the DRC ($X_{RC,i}$) is calculated accordingly $X_{RC,i} = \frac{k_i}{r}\left(\frac{\partial r}{\partial k_i}\right)_{k_{j\neq i},K_i} = \left(\frac{\partial lnr}{\partial lnk_i}\right)_{k_{j\neq i},K_i}$, where k_i, K_i, and r are the forward rate constant and the equilibrium constant for elementary step *i*, and the reaction rate, respectively. Additionally, the DRCs obey the following sum rule $\sum_i X_{RC,i} = 1$.

5.4 Results and Discussion

When acetylene is hydrogenated, the semi-hydrogenated product (ethylene) and the fully hydrogenated product (ethane) can be formed. Ideally, 100% selectivity toward ethylene (and zero ethane) with high conversion of acetylene is the most desired outcome for a potential catalyst. However, the more favorable thermodynamics toward ethane formation presents a challenge when the possibility of re-adsorption and further hydrogenation exists. Therefore, whether POHs can overcome such a challenge to achieve acetylene semi-hydrogenation is the key question that we investigate with the BTOH (211)-Ba_2O_4H in this study.

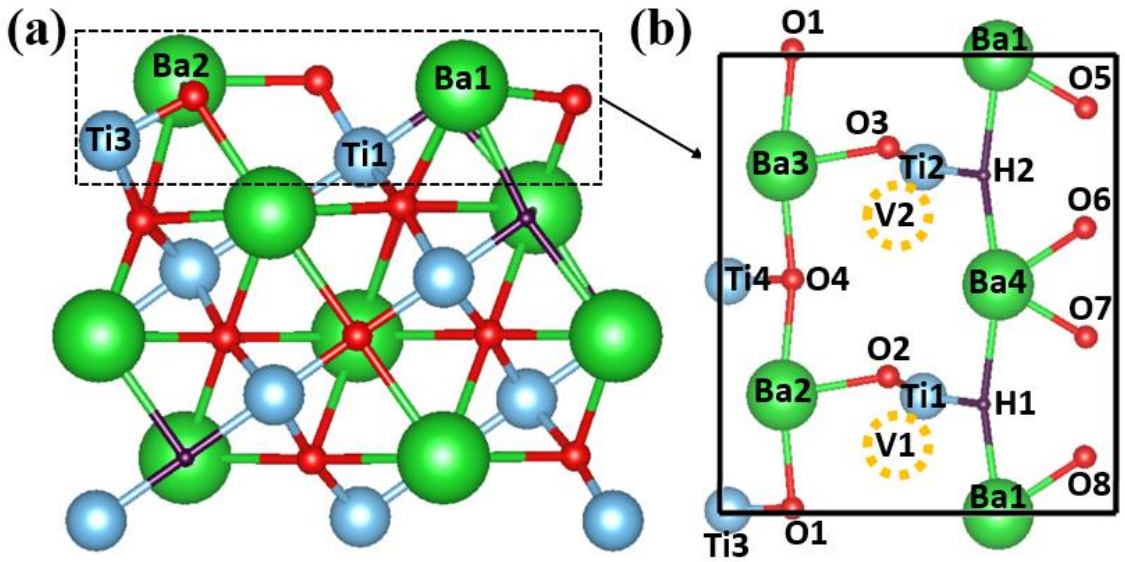

Figure 5.1 Structure model of the (211)-Ba_2O_4H surface termination of $BaTiO_{2.5}H_{0.5}$: (a) side view of the slab (the box denotes the surface layers); (b) top view of the surface layers [the box region in (a)]. The yellow dotted circles labeled V1 and V2 represent the surface anion vacancies.

5.4.1 Surface structure of the BTOH (211)-Ba2O4H termination. It was previously[24] found that the most stable BTOH surface termination under acetylene semi-hydrogenation conditions (523 K, P_{total} = 1 bar)[20] is (211)-Ba_2O_4H. A side view of the slab model is shown in Figure 5.1a; the top two surface layers (box in Figure 5.1a) are further displayed as a top view in Figure 5.1b. The relatively flat surface comprises Ba, O, and H atoms as well as anion vacancies (dotted circles in Figure 5.1b). In addition, next to each of the anion vacancies is one subsurface Ti. How these surface species work together for H_2 activation and C_2H_2 adsorption/hydrogenation are the important mechanistic questions that we want to answer. It is hypothesized that the surface anion vacancies are involved in heterolytic H_2 dissociation as this process over metal oxides is typically more kinetically favored than homolytic H_2 dissociation.[46,47]

5.4.2 Overview of acetylene semi-hydrogenation on BTOH (211)-Ba2O4H.

Typically, hydrogenation reactions over heterogeneous catalysts occur via the Horiuti-Polanyi mechanism in which H_2 initially dissociates over the surface and the resulting H species are then sequentially added to unsaturated compounds such as acetylene.[48]

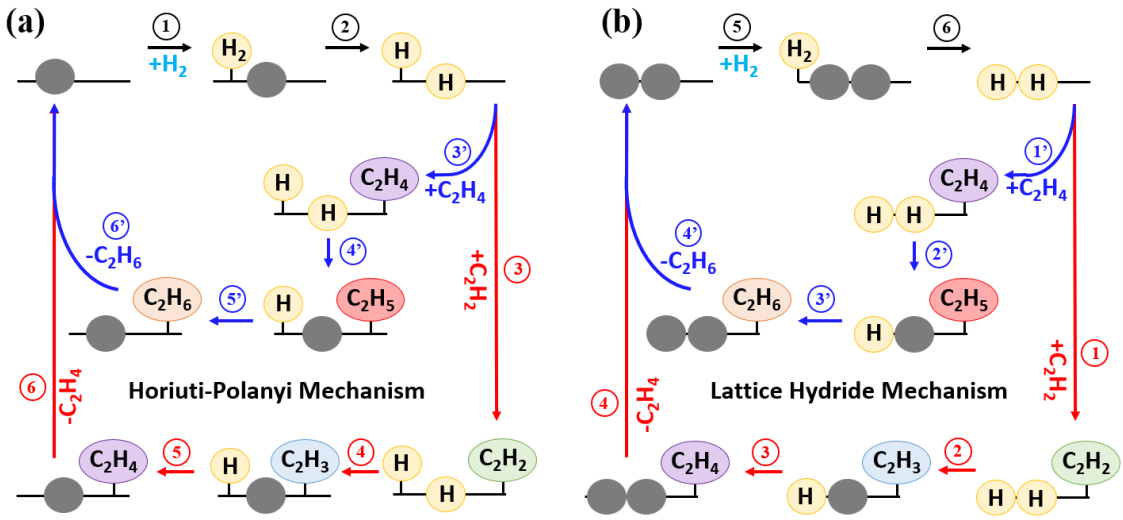

Figure 5.2 Mechanistic overview of acetylene hydrogenation over BTOH: (a) the Horiuti-Polanyi mechanism; (b) the lattice hydride mechanism. The BTOH surface is represented as a horizontal black line and the gray dots on the line represent surface anion vacancies. In both (a) and (b), the pathway following the red arrows leads to acetylene semi-hydrogenation and the pathway following the blue arrows leads to ethylene hydrogenation. For each mechanism, the hydrogen adsorption step begins at the top left of the figure, and the numbering corresponds to the states in the DFT calculated energy diagrams of sections 5.4.3 and 5.4.4.

Figure 5.2a shows a schematic for such a mechanism on the BTOH surface where a surface anion vacancy is represented by a gray dot; after H_2 adsorption (step 1) and dissociation (step 2), C_2H_2 adsorbs (step 3) and gets hydrogenated (steps 4 and 5). Because C_2H_4 is also assumed to be present in the gas phase, it can also adsorb (step 3') and get hydrogenated (steps 4' and 5') on the surface. On the other hand, BTOH contains labile lattice hydrides

that can participate in hydrogenation reactions, so we also investigate the lattice hydride mechanism which resembles the Mars-van Krevelen mechanism of lattice oxygen for oxidation reactions. As shown in Figure 5.2b, herein two surface BTOH lattice hydrides are initially used to hydrogenate adsorbed acetylene (step 1) to ethylene (steps 2 and 3); after ethylene desorption (step 4), the lattice sites are regenerated by reacting the surface anion vacancies with molecular hydrogen (steps 5 and 6). Likewise, C_2H_4 can also adsorb (step 1') and get hydrogenated by the lattice hydrides (steps 2' and 3'). In section 5.4.3 and section 5.4.4 we examine each mechanism in detail.

5.4.3 The Horiuti-Polanyi mechanism. Figure 5.3 shows the energy profiles for acetylene semi-hydrogenation to ethylene via the Horiuti-Polanyi mechanism. It begins with H_2 adsorption (state 2, Figure 5.3a) followed by heterolytic H_2 dissociation (E_a = 0.53 eV; TS1) over a surface anion vacancy and surface oxygen site (O2 in Figure 5.1b) to form one surface hydride and one surface hydroxyl. From there, acetylene adsorbs onto the hydrogenated surface at the O1 site (state 5, Figure 5.3b), which is then hydrogenated by the surface hydride (E_a = 0.34 eV; TS2A, state 6 in Figure 5.3a) to form the vinyl intermediate (state 7A in Figure 5.3b). Lastly, the surface proton on the hydroxyl group hydrogenates the vinyl intermediate (E_a = 0.08 eV; TS3A) to form ethylene (state 10A). An energy of 0.55 eV is necessary to desorb ethylene from the surface (10 → 11 in Figure 5.3a). Overall, one can see that this path has rather low barriers from H_2 activation and acetylene hydrogenation. In Path A, acetylene is hydrogenated at the proximal carbon to form intermediate state 7A. Alternatively, acetylene can be hydrogenated at the distal carbon (Path B) to form a metastable intermediate state 7B which further relaxes to a more

stable intermediate state 8B where the vinyl intermediate forms a C-Ti bond with subsurface Ti1 at a distance of 2.29 Å. From there, a barrier of 0.79 eV has to be overcome to hydrogenate the vinyl intermediate in state 8B to form ethylene in state 10B.

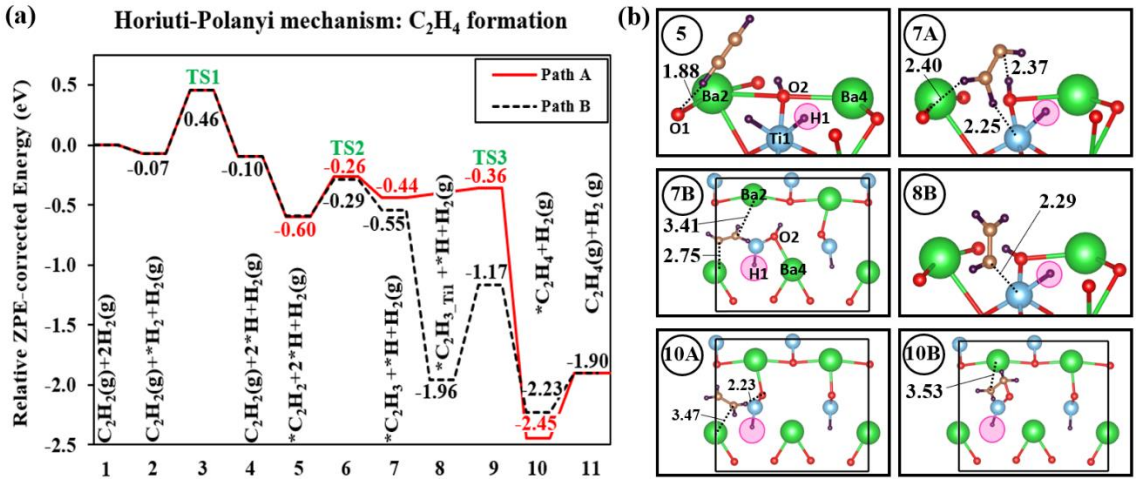

Figure 5.3 Semi-hydrogenation of C_2H_2 to C_2H_4 via the Horiuti-Polanyi mechanism on BTOH (211)-Ba_2O_4H: (a) energy profiles for two paths; (b) key intermediate structures. In (b), A/B after state number indicates path A/B in (a); lattice hydride is highlighted in pink. All energies listed are ZPE corrected, and all atomic distances are reported in units of Å. Ba, green; Ti, blue; O, red; H, dark purple; C, light brown. The same color scheme is used in subsequent figures.

As a competing pathway, ethylene can also be hydrogenated to form ethane as shown in Figure 5.4. In this case, after H_2 adsorption (state 13) and dissociation (states 14-15), ethylene is adsorbed onto the hydrogenated surface (state 16) and then hydrogenated by a surface hydride (E_a = 0.50 eV, TS2) to form the ethyl intermediate (state 18). From here, subsequent ethyl hydrogenation can continue either through path C or D. In path C, the ethyl intermediate is adsorbed onto the Ba2 site (state 18) and then hydrogenated by the surface proton through a near barrierless process (E_a = 0.01 eV, TS3C) to form ethane

(state 22C). The desorption energy of ethane in state 22C is 0.34 eV. We also explored a path D whereby the ethyl intermediate moves from interacting with Ba2 (state 18) to Ti1 (state 20D), prompted by the energetically stable C-Ti1 bond formed between vinyl and the surface (8B in Figure 5.3b). We found that an energy barrier of 0.39 eV is required for this transition from state 18 to 20D to occur before finally hydrogenating the ethyl intermediate (E_a = 0.59 eV, TS3D) to ethane (state 22D) with the surface proton. The desorption energy of ethane in state 22D is 0.30 eV.

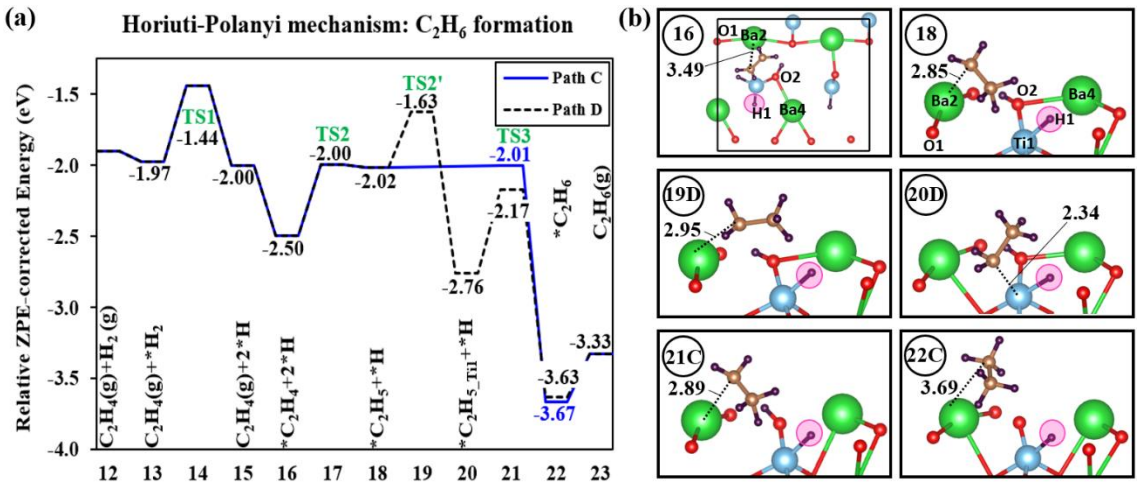

Figure 5.4 Hydrogenation of C_2H_4 to C_2H_6 via the Horiuti-Polanyi mechanism on BTOH (211)-Ba_2O_4H: (a) energy profiles for two paths; (b) key intermediate structures. In (b), C/D after state number indicates path C/D in (a); lattice hydride is highlighted in pink. All energies listed are ZPE corrected, and all atomic distances are reported in units of Å.

To compare Path A and B for ethylene formation and Path C and D for ethane formation, we performed microkinetic modeling using the DFT energetics in Figures 5.3 and 5.4 under the typical conditions of 523 K and 1.1 bar for a mixture of 1.76% H_2, 0.09% C_2H_2, 3.60% C_2H_4, and He balance.[49,50,51] As shown in Table 5.1, Path B is the preferred channel for ethylene formation over Path A and is over four orders of magnitude faster than

ethane formation via Path C. In other words, we predict that the BTOH(211)-Ba_2O_4H surface can catalyze acetylene semi-hydrogenation with high selectivity, if the Horiuti-Polanyi mechanism is the main channel. A detailed explanation for the favorability of Path B over A is explained in section A2.3 of the Appendix (section 5.7). The chemical kinetic reasons for this selectivity difference will be analyzed and discussed in section 5.4.6.

Table 5.1 Rates of ethylene and ethane formation via the Horiuti-Polanyi mechanism at a temperature of 523 K and pressure of 1.1 bar. Gas mixture: 1.76% H_2, 0.09% C_2H_2, 3.60% C_2H_4, He gas balance.

	C_2H_4 formation		C_2H_6 formation	
Path	**A**	**B**	**C**	**D**
Rate (mol s^{-1} unit $cell^{-1}$)	2.42	22.4	2.11E-03	3.78E-04

5.4.4 The lattice hydride mechanism. Figure 5.5 shows the energy profiles for acetylene semi-hydrogenation to ethylene via the lattice hydride mechanism. After initial migration of the H_2 lattice hydride to the V1 vacancy site (states 1-5), the mechanism (Figure 5.5a) continues with acetylene adsorption at the O1 site (state 6E, Figure 5.5b) which is then hydrogenated by the H2 lattice hydride (E_a = 0.53 eV; TS3E) to form the vinyl intermediate (state 8E). Finally, the H1 lattice hydride hydrogenates the vinyl intermediate (E_a = 0.48 eV; TS4) to form ethylene (state 13E). To regenerate the lattice hydrides, ethylene must first desorb from the hydride-deficient surface (E_{des} = 0.48 eV) such that H_2 can then adsorb above the V1 site (state 15) and dissociate (E_a = 0.80 eV, TS5). Path E has acetylene first being hydrogenated at the proximal carbon to form intermediate state 8E.

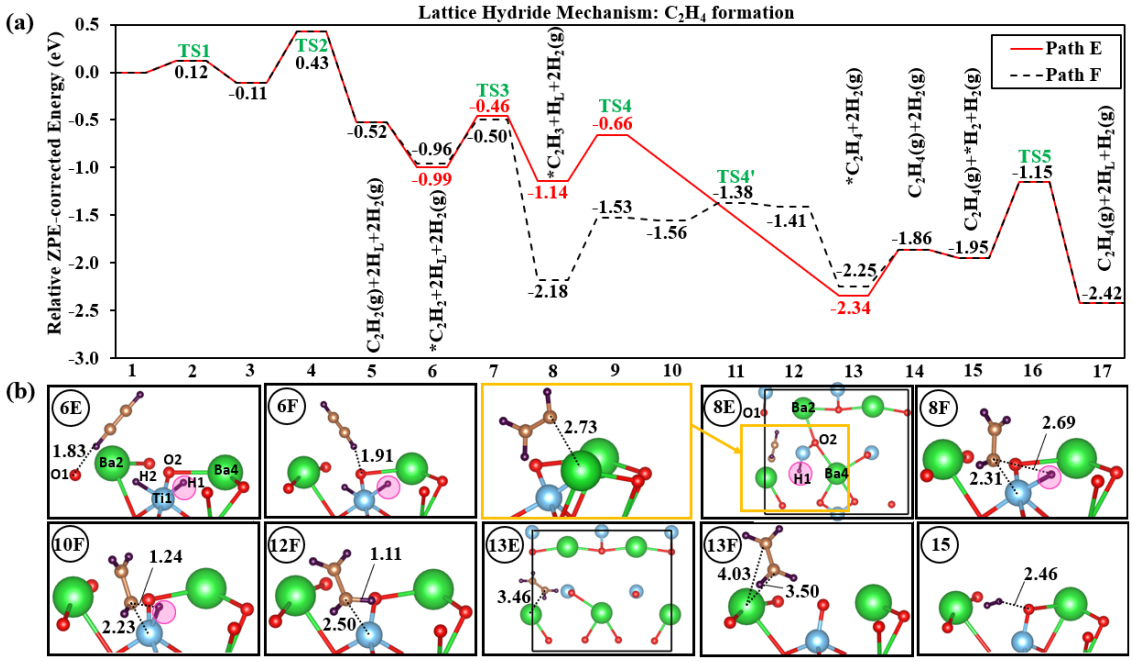

Figure 5.5 Semi-hydrogenation of C_2H_2 to C_2H_4 via the lattice hydride mechanism on BTOH (211)-Ba_2O_4H: (a) energy profiles for two paths; (b) key intermediate structures. In (b), E/F after state number indicates path E/F in (a); lattice hydride is highlighted in pink. All energies listed are ZPE corrected, and all atomic distances are reported in units of Å.

Alternatively, acetylene can be hydrogenated at the distal carbon (Path F) to form a very stable intermediate state 8F where the vinyl intermediate forms a bond with subsurface Ti1. Then, a barrier of 0.65 eV has to be overcome to bring the vinyl intermediate closer to the H1 lattice hydride. Next, the lattice hydride hydrogenates the vinyl intermediate at the V1 site (E_a = 0.18 eV, TS4') to form a metastable intermediate state 12F which further relaxes to a more stable intermediate state 13F where ethylene is adsorbed onto the Ba1 site.

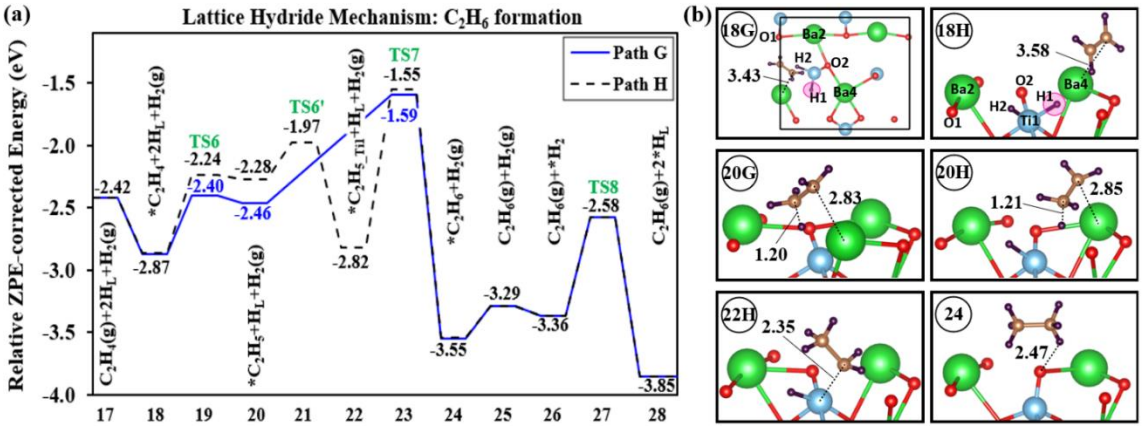

Figure 5.6 Hydrogenation of C_2H_4 to C_2H_6 via the lattice hydride mechanism on BTOH (211)-Ba_2O_4H: (a) energy profiles for two paths; (b) key intermediate structures. In (b), G/H after state number indicates path G/H in (a); lattice hydride is highlighted in pink. All energies listed are ZPE corrected, and all atomic distances are reported in units of Å.

The two adjacent lattice hydrides on the BTOH surface can also further hydrogenate ethylene to ethane as shown in Figure 5.6. In Path G, after ethylene adsorption (state 18), it takes 0.47 eV of energy to hydrogenate ethylene (TS6G) to the ethyl intermediate (state 20G). An additional 0.87 eV of energy is required to hydrogenate the ethyl intermediate (TS7G) to ethane (state 24). In Path H, a lattice hydride first hydrogenates (E_a = 0.63 eV, TS6H) adsorbed ethylene to the ethyl intermediate which is adsorbed onto the Ba4 site (state 20H). Then the ethyl intermediate rotates about the Ba4 site to form a bond with subsurface Ti1 (E_a = 0.31 eV; TS6'). Subsequent C-Ti1 bond cleavage and C-H bond formation requires 1.27 eV of energy to occur before finally yielding an ethane molecule adsorbed on the surface (state 24). Lastly, ethane is desorbed from the hydride-deficient surface (E_{des} = 0.26 eV) before the lattice hydrides are regenerated.

To compare Path E and F for ethylene formation and Path G and H for ethane formation, we again performed microkinetic modeling using the DFT energetics in Figures 5.5 and 5.6 under the same conditions. The results listed in Table 5.2 show that ethylene formation can occur through either Path E or F and this process is over four orders of magnitude faster than ethane formation. In other words, we predict that the BTOH(211)-Ba_2O_4H surface can also catalyze acetylene semi-hydrogenation with high selectivity via the lattice hydride mechanism. However, we see that the rates in Table 5.2 are significantly lower than the rates in Table 5.1.

Table 5.2 Rates of ethylene and ethane formation via the lattice hydride mechanism at a temperature of 523 K and pressure of 1.1 bar. Gas mixture: 1.76% H_2, 0.09% C_2H_2, 3.60% C_2H_4, He gas balance.

	C_2H_4 formation		C_2H_6 formation	
Path	**E**	**F**	**G**	**H**
Rate (mol s^{-1} unit $cell^{-1}$)	0.267	0.266	2.02E-05	6.50E-06

5.4.5 Comparison of the two mechanisms in terms of surface structure. Our results above show that both the Horiuti-Polanyi mechanism and the lattice hydride mechanism are predicted to be able to lead to selective semi-hydrogenation of acetylene to ethylene on the BTOH (211)-Ba_2O_4H surface. Comparing Tables 1 and 2, we conclude that the Horiuti-Polanyi channel is about 100 times faster than the lattice hydride channel. Figure 5.7 compares the surface structures prior to C_2H_2 adsorption. The main difference is the presence of a proton on a surface O atom in Figure 5.7a due to the heterolytic H_2 activation. The surface hydride in Figure 5.7a is more active in the first hydrogenation of

acetylene via the Horiuti-Polanyi mechanism (Figure 5.3, E_a=0.31 eV via Path B) than the H2 lattice hydride in Figure 5.7b involved in the lattice hydride mechanism (Figure 5.5, E_a=0.46 eV via Path F). This higher activity of surface hydride in Figure 5.7a than in Figure 5.7b is correlated with the larger Ba1-H distances in Figure 5.7a than in Figure 5.7b. In other words, more active hydrides are found in the Horiuti-Polanyi mechanism due to weaker interaction between Ba1 and H.

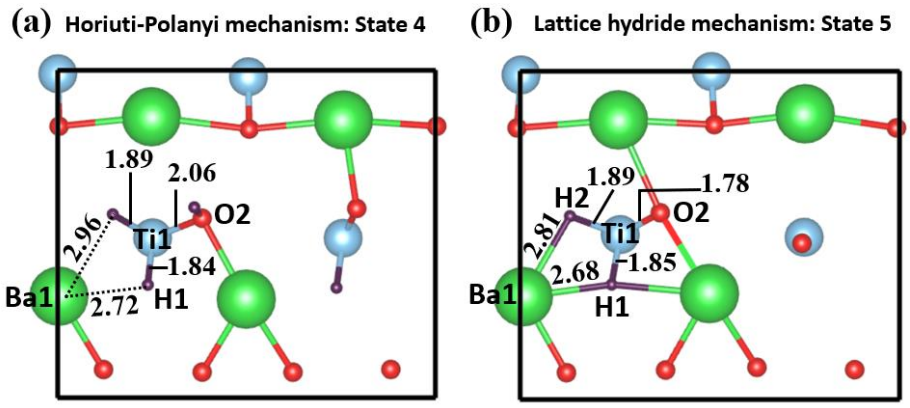

Figure 5.7 Comparison of surface structures prior to C_2H_2 adsorption: (a) in Horiuti-Polanyi mechanism; (b) in the lattice hydride mechanism. All atomic distances are reported in units of Å.

5.4.6 Further kinetic Analysis. To gain a deeper understanding as to which step(s) is the key factor in determining product selectivity of ethylene over ethane for the more active Horiuti-Polanyi mechanism, further microkinetic modeling was performed. A selectivity analysis for the temperature range of 373 – 673 K (Figure 5.8a) shows that the product observed is essentially only ethylene even when C_2H_4 is a substantial fraction of the feed. This is consistent with the total production plot in Figure 5.8b which shows the rate of ethylene production being faster than ethane production at all temperatures. Further

examination of the predominant surface species (Figure 5.8c) reveals that during steady-state, essentially only C_2H_3_Ti1 and H_O2 exist on the BTOH surface which can then combine to form ethylene. C_2H_3_Ti1 represents the vinyl intermediate bonded to subsurface Ti1 by occupying the surface vacancy anion site and H_O2 represents the proton adsorbed on the surface O2 site. The reason for the larger abundance of C_2H_3_Ti1 as compared to any other adsorbed species is two-fold. First, because the energy barrier for the first hydrogenation of acetylene (0.31 eV) is lower than that of the first hydrogenation of ethylene (0.50 eV), the formation of the vinyl intermediate (state 8B, Figure 5.3) is favored over the ethyl intermediate (state 20D, Figure 5.4). Second, the formation of the C-Ti1 bond in state 8B greatly stabilizes the vinyl intermediate which prevents the reformation of acetylene as indicated by the relatively high reverse energy barrier (1.67 eV). Thus, even though the second hydrogenation of ethylene has much lower barrier than the second hydrogenation of acetylene (0.01 eV vs 0.79 eV), the surface is dominated by coverage of the C_2H_3_Ti1 intermediate which leads to ethylene rather than ethane formation.

To better understand the importance of each elementary step to the overall BTOH activity, the DRC analysis as a function of temperature was also performed with respect to ethylene formation via Path B (Figure 5.3). We found that only the H_2 dissociation and the first and second hydrogenation of acetylene steps have DRCs greater than 0.01. As one can see from Figure 5.8d, the ethylene formation activity is mainly dependent on the first hydrogenation step when temperature is above 473 K. Below 473 K, H_2 dissociation becomes the most rate-controlling step.

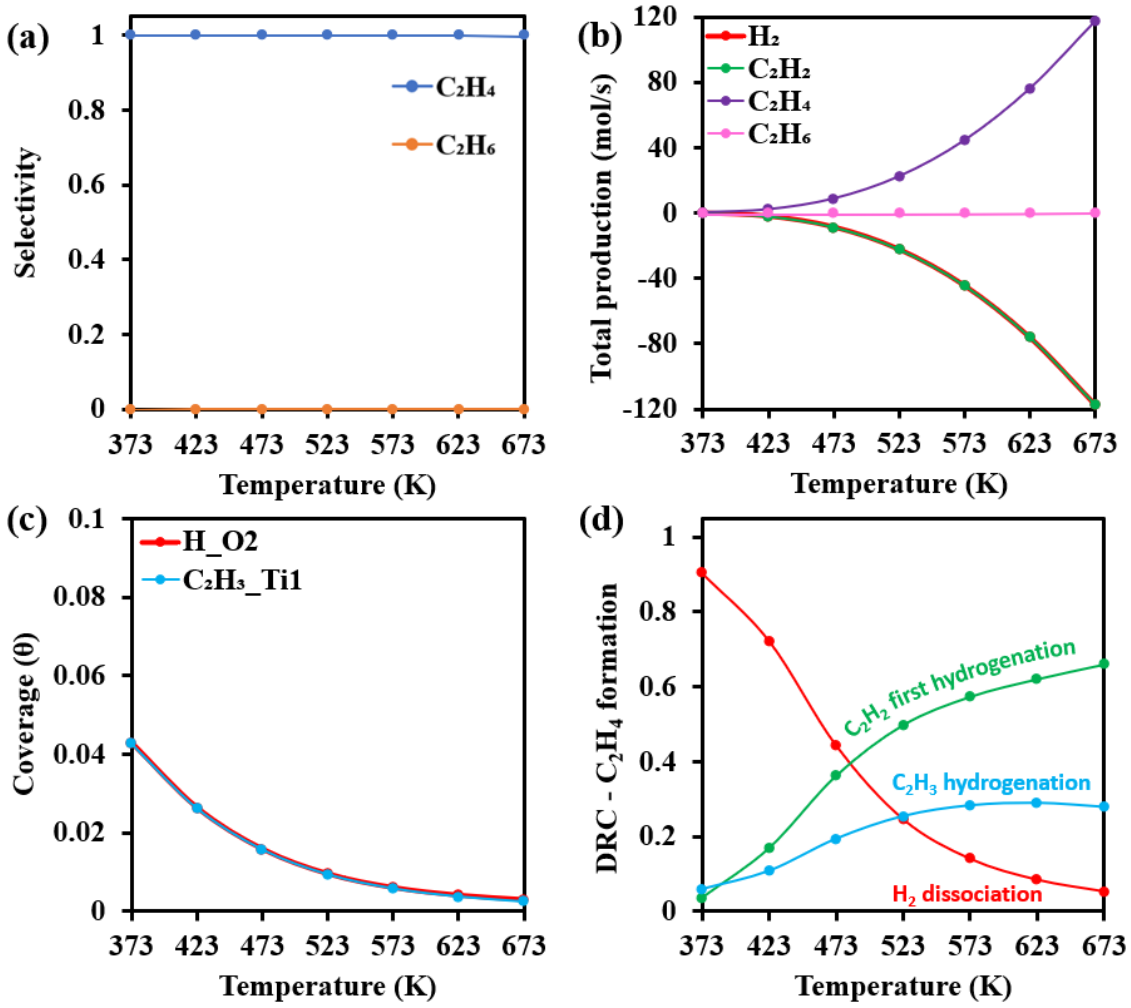

Figure 5.8 Detailed microkinetic analysis of temperature dependence of hydrogenation of C_2H_2 to C_2H_4 and C_2H_4 to C_2H_6 via the Horiuti-Polanyi mechanism on BTOH (211)-Ba_2O_4H: (a) selectivity; (b) total production; (c) surface coverages; (d) degree of rate control (DRC). Conditions used: T = 523 K, P_{total} = 1.1 bar, Gas mixture: 1.76% H_2, 0.09% C_2H_2, 3.60% C_2H_4, He gas balance. Only surface coverages and DRC values of magnitude greater than 0.01 were plotted in (c) and (d), respectively.

5.5 Conclusion

In this work, we have used first-principles density functional theory coupled with microkinetic modeling to investigate acetylene semi-hydrogenation on the BTOH(211)-Ba_2O_4H surface termination. In the Horiuti-Polanyi mechanism, H_2 first heterolytically

dissociates on the surface and the resulting surface H atoms are then sequentially added to acetylene. In the lattice hydride mechanism, two lattice hydrides from the BTOH surface hydrogenate acetylene first and are then regenerated from H_2 reacting with the two lattice-hydride vacancies. We have determined the minimum-energy pathways for the two mechanisms in acetylene hydrogenation to ethylene and then to ethane. Microkinetic modeling based on these DFT energies and barriers indicates that ethylene and ethane formation via the Horiuti-Polanyi mechanism is faster than via the lattice hydride mechanism and that for both mechanisms formation of ethylene occurs at a faster rate than that of ethane. Therefore, our simulations suggest that BTOH can selectively hydrogenate acetylene to ethylene with a high selectivity under the specified conditions. The presence of lattice hydrides in BTOH resulted in a surface containing vacancies under the given reaction conditions which in turn are of importance in the facile heterolytic cleavage of H_2 over BTOH as a means to provide active H species for hydrogenation in the Horiuti-Polanyi mechanism. In addition, the surface anion vacancies are crucial to stabilizing the vinyl intermediate and, therefore, drive the reaction selectivity towards ethylene. The findings in this work provide a deeper understanding on the role of surface anion vacancies in the BTOH catalyst for acetylene semi-hydrogenation selectivity and suggest the potential use of BTOH and other perovskite oxyhydride materials as catalysts for general alkyne semi-hydrogenation.

5.6 References

(1) Kobayashi, Y.; Hernandez, O. J.; Sakaguchi, T.; Yajima, T.; Roisnel, T.; Tsujimoto, Y.; Morita, M.; Noda, Y.; Mogami, Y.; Kitada, A.; Ohkura, M.; Hosokawa, S.; Li, Z.; Hayashi, K.; Kusano, Y.; Kim, J.; Tsuji, N.; Fujiwara, A.; Matsushita, Y.; Yoshimura, K.; Takegoshi, K.; Inoue, M.; Takano, M.; Kageyama, H. An oxyhydride of $BaTiO_3$ exhibiting hydride exchange and electronic conductivity. *Nat. Mater.* **2012**, 11, 507-511.

(2) Tang, Y.; Kobayashi, Y.; Shitara, K.; Konishi, A.; Kuwabara, A.; Nakashima, T.; Tassel, C.; Yamamoto, T.; Kageyama, H. On Hydride Diffusion in Transition Metal Perovskite Oxyhydrides Investigated via Deuterium Exchange. *Chem. Mater.* **2017**, 29, 8187-8194.

(3) Sakaguchi, T.; Kobayashi, Y.; Yajima, T.; Ohkura, M.; Tassel, C.; Takeiri, F.; Mitsuoka, S.; Ohkubo, H.; Yamamoto, T.; Kim, J.; Tsuji, N.; Fujihara, A.; Matsushita, Y.; Hester, J.; Avdeev, M.; Ohoyama, K.; Kageyama, H. Oxyhydrides of $(Ca,Sr,Ba)TiO_3$ Perovskite Solid Solutions. *Inorg. Chem.* **2012**, 51, 11371-11376.

(4) Yajima, T.; Takeiri, F.; Aidzu, K.; Akamatsu, H.; Fujita, K.; Yoshimune, W.; Ohkura, M.; Lei, S.; Gopalan, V.; Tanaka, K.; et al. A labile hydride strategy for the synthesis of heavily nitridized $BaTiO_3$. *Nat. Chem.* **2015**, 7, 1017-1023.

(5) Kobayashi, Y.; Hernandez, O.; Tassel, C.; Kageyama, H. New chemistry of transition metal oxyhydrides. *Sci. Technol. Adv. Mater.* **2017**, 18, 905-918.

(6) Masuda, N.; Kobayashi, Y.; Hernandez, O.; Bataille, T.; Paofai, S.; Suzuki, H.; Ritter, C.; Ichijo, N.; Noda, Y.; et al. Hydride in $BaTiO_{2.5}H_{0.5}$: A Labile Ligand in Solid State Chemistry. *J. Am. Chem. Soc.* **2015**, 137, 15315-15321.

(7) Zhang, J.; Gou, G.; Pan, B. Study of Phase Stability and Hydride Diffusion Mechanism of BaTiO3 Oxyhydride from First-Principles. *J. Phys. Chem. C* **2014**, 118, 17254−17259.

(8) Eklöf-Österberg, C.; Nedumkandathil, R.; Häussermann, U.; Jaworski, A.; Pell, A. J.; Tyagi, M.; Jalarvo, N. H.; Frick, B.; Faraone, A.; Karlsson, M. Dynamics of Hydride Ions in Metal Hydride-Reduced $BaTiO_3$ Samples Investigated with Quasielastic Neutron Scattering. *J. Phys. Chem. C* **2019**, 123, 2019−2030.

(9) Tang, Y.; Kobayashi, Y.; Tassel, C.; Yamamoto, T.; Kageyama, H. Hydride-Enhanced CO_2 Methanation: Water-Stable $BaTiO_{2.4}H_{0.6}$ as a New Support. *Adv. Energy Mater.* **2018**, 8, 1800800.

(10) Tang, Y.; Kobayashi, Y.; Masuda, N.; Uchida, Y.; Okamoto, H.; Kageyama, T.; Hosokawa, S.; Loyer, F.; Mitsuhara, K.; Yamanaka, K.; Tamenori, Y.; Tassel, C.; Yamamoto, T.; Tanaka, T.; Kageyama, H. Metal-Dependent Support Effects of Oxyhydride-Supported Ru, Fe, Co Catalysts for Ammonia Synthesis. *Adv. Energy Mater.* **2018**, 8, 1801772.

(11) Kobayashi, Y.; Tang, Y.; Kageyama, T.; Yamashita, H.; Masuda, N.; Hosokawa, S.; Kageyama, H. Titanium-Based Hydrides as Heterogeneous Catalysts for Ammonia Synthesis. *J. Am. Chem. Soc.* **2017**, 139, 18240-18246.

(12) M. Appl, Ammonia, 1. Introduction. In Ullmann's Encyclopedia of Industrial Chemistry (Wiley-VCH Verlag GmbH, 2012).
(13) Delgado, J. A.; Benkirane, O.; Claver, C.; Curulla-Ferre, D.; Godard, C. Advances in the preparation of highly selective nanocatalysts for the semi-hydrogenation of alkynes using colloidal approaches. *Dalton Trans.* **2017**, 46, 12381-12403.
(14) Pachulski, A.; Schödel, R.; Claus, P. Performance and regeneration studies of Pd-Ag/Al_2O_3 catalysts for the selective hydrogenation of acetylene. *Appl Catal A Gen* **2011**, 400, 14-24.
(15) Studt, F.; Abild-Pedersen, F.; Bligaard, T.; Sørensen, R. Z.; Christensen, C. H.; Nørskov, J. K. Identification of Non-Precious Metal Alloy Catalysts for Selective Hydrogenation of Acetylene. *Science* **2008**, 320, 1320-1322.
(16) Huang, F.; Deng, Y.; Chen, Y.; Cai, X.; Peng, M.; Jia, Z.; Xie, J.; Xiao, D.; Wen, X.; Wang, N.; Jiang, Z.; Liu, H.; Ma, D. Anchoring Cu_1 species over nanodiamond-graphene for semi-hydrogenation of acetylene. *Nat. Commun.* **2019**, 10, 4431.
(17) Wang, Y.; Liu, B.; Lan, X.; Wang, T. Subsurface Carbon as a Selectivity Promotor to Enhance Catalytic Performance in Acetylene Semihydrogenation. *ACS Catal.* **2021**, 11, 10257-10266.
(18) Liu, Y.; Liu, X.; Feng, Q.; He, D.; Zhang, L.; Lian, C.; Shen, R.; Zhao, G.; Ji, Y.; Wang, D.; Zhou, G.; Li, Y. Intermetallic Ni_xM_y (M = Ga and Sn) Nanocrystals: A Non-previous Metal Catalyst for Semi-Hydrogenation of Alkynes. *Adv. Mater.* **2016**, 28, 4747-4754.
(19) Tejeda-Serrano, M.; Cabrero-Antonino, J. R.; Mainar-Ruiz, V.; Lopez-Haro, M.; Hernandez-Garrido, J. C.; Calvino, J. J.; Leyva-Perez, A.; Corma, A. Synthesis of Supported Planar Iron Oxide Nanoparticles and Their Chemo- and Stereoselectivity for Hydrogenation of Alkynes. *ACS Catal.* **2017**, 7, 3721-3729.
(20) Vilé, G.; Bridier, B.; Wichert, J.; Pérez-Ramírez, J. Ceria in Hydrogenation Catalysis: High Selectivity in the Conversion of Alkynes to Olefins. *Angew. Chem.* **2012**, 124, 8748-8751.
(21) Albani, D.; Capdevila-Cortada, M.; Vilé, Mitchell, S.; Martin, O.; López, N.; Pérez-Ramírez, J. Semi-hydrogenation of Acetylene on Indium Oxide: Proposed Single-Ensemble Catalysis. *Angew. Chem.* **2017**, 129, 10895-10900.
(22) Moon, J.; Cheng, Y.; Daemen, L. L.; Li, M.; Polo-Garzon, F.; Ramirez-Cuesta, A. J.; Wu, Z. Discriminating the Role of Surface Hydride and Hydroxyl for Acetylene Semi-hydrogenation over Ceria through *In Situ* Neutron and Infrared Spectroscopy. *ACS Catal.* **2020**, 10, 5278-5287.
(23) Wang, Z.-Q.; Chu, D.-R.; Zhou, H.; Wu, X.-P.; Gong, X.-Q. Role of Low-Coordinated Ce in Hydride Formation and Selective Hydrogenation Reactions on CeO_2 Surfaces. *ACS Catal.* **2022**, 12, 624-632.
(24) Wang, K.; Fung, V.; Wu, Z.; Jiang, D.-E. Stable Surface Terminations of a Perovskite Oxyhydride from First Principles. *J. Phys. Chem. C* **2020**, 124, 18557-18563.

(25) Kresse, G.; Furthmüller, J. Efficiency of ab-initio total energy calculations for metals and semiconductors using a plane-wave basis set. *Comput. Mater. Sci.* **1996**, 6, 15-50.
(26) Kresse, G.; Furthmüller, J. Efficient Iterative Schemes for Ab Initio Total-Energy Calculations Using a Plane-Wave Basis Set. *Phys. Rev. B: Condens. Matter Mater. Phys.* **1996**, 54, 11169-11186.
(27) Perdew, J. P.; Burke, K.; Ernzerhof, M. Generalized Gradient Approximation Made Simple. *Phys. Rev. Lett.* **1996**, 77, 3865.
(28) Blöchl, P. E. Projector Augmented-Wave Method. *Phys. Rev. B: Condens. Matter Mater. Phys.* **1994**, 50, 17953-17979.
(29) Grimme, S.; Antony, J.; Ehrlich, S.; Krieg, H. A consistent and accurate *ab initio* parametrization of density functional dispersion correction (DFT-D) for the 94 elements H-Pu. *J. Chem. Phys.* **2010**, 132, 154104.
(30) Tang, W.; Sanville, E.; Henkelman, G. A grid-based Bader analysis algorithm without lattice bias. *J. Phys.: Condens. Matter* **2009**, 21, 084204.
(31) Monkhorst, H. J.; Pack, J. D. Special points for Brillouin-zone integrations. *Phys. Rev. B: Solid State* **1976**, 13, 5188-5192.
(32) Neugebauer, J.; Scheffler, M. Adsorbate-substrate and adsorbate-adsorbate interactions of Na and K adlayers on Al(111). *Phys. Rev. B* **1992**, 46, 16067-16080.
(33) Henkelman, G.; Jónsson, H. Improved tangent estimate in the nudged elastic band method for finding minimum energy paths and saddle points. *J. Chem. Phys.* **2000**, 113, 9978-9985.
(34) Henkelman, G.; Jónsson, H. A dimer method for finding saddle points on high dimensional potential surfaces using only first derivatives. *J. Chem. Phys.* **1999**, 111, 7010-7022.
(35) Filot, I. A. W.; Zijlstra, B.; Hensen, E. J. M. MKMCXX, a C++ Program for Constructing Microkinetic Models. http://www.mkmcxx.nl (accessed Jul 27, 2021).
(36) Filot, I. A. W.; van Santen, R. A.; Hensen, E. J. M. The optimally performing Fischer−Tropsch catalyst. *Angew. Chem., Int. Ed.* **2014**, 53, 12746−12750.
(37) Filot, I. A. W.; Broos, R. J. P.; van Rijn, J. P. M.; van Heugten, G. J. H.; van Santen, R. A.; Hensen, E. J. M. First-principles based microkinetics simulations of synthesis gas conversion on a stepped rhodium surface. *ACS Catal.* **2015**, 5, 5453−5467.
(38) Matera, S.; Schneider, W. F.; Heyden, A.; Savara, A. Progress in Accurate Chemical Kinetic Modeling, Simulations, and Parameter Estimation for Heterogeneous Catalysis. *ACS Catal.* **2019**, 9, 6624-6647.
(39) Zijlstra, B.; Broos, R. J. P.; Chen, W.; Filot, I. A. W.; Hensen, E. J. M. First-principles based microkinetic modeling of transient kinetics of CO hydrogenation on cobalt catalysts. *Catal. Today* **2020**, 342, 131-141.
(40) JANAF thermochemical tables, 1982 supplement, J. Phys. Chem. Ref. Data 11 (1982) 695–940.

(41) Shomate, C. H. A method for evaluating and correlating thermodynamic data. *J. Phys. Chem.* **1954**, 58, 368–372.
(42) Savara, A. Standard States for Adsorption on Solid Surfaces: 2D Gases, Surface Liquids, and Langmuir Adsorbates. *J. Phys. Chem. C* **2013**, 117, 15710-15715.
(43) Sprowl, L. H.; Campbell, C. T.; Árnadóttir, L. Hindered Translator and Hindered Rotor Models for Adsorbates: Partition Functions and Entropies. *J. Phys. Chem. C* **2016**, 120, 9719-9731.
(44) Campbell, C. T. Finding the rate-determining step in a mechanism: comparing DeDonder relations with the "Degree of Rate Control". *J. Catal.* **2001**, 204, 520−524.
(45) Stegelmann, C.; Andreasen, A.; Campbell, C. T. Degree of rate control: How much the energies of intermediates and transition states control rates. *J. Am. Chem. Soc.* **2009**, 131, 8077−8082.
(46) García-Melchor, M.; López, N. Homolytic Products from Heterolytic Paths in H_2 Dissociation on Metal Oxides: The Example of CeO_2. *J. Phys. Chem. C* **2014**, 118, 10921-10926.
(47) Hu, G.; Wu, Z.; Jiang, D.E. First Principles Insight into H_2 Activation and Hydride Species on TiO_2 Surfaces. *J. Phys. Chem. C* **2018**, 122, 20323-20328.
(48) Horiuti, J.; Polanyi, M. Exchange reactions of hydrogen on metallic catalysts. *Trans. Faraday Soc.* **1934**, 163, 1164.
(49) Pei, G. X.; Liu, X. Y.; Wang, A.; Lee, A. F.; Isaacs, M. A.; Li, L.; Pan, X.; Yang, X.; Wang, X.; Tai, Z.; Wilson, K.; Zhang, T. Ag Alloyed Pd Single-Atom Catalysts for Efficient Selective Hydrogenation of Acetylene to Ethylene in Excess Ethylene. *ACS Catal.* **2015**, 5, 3717-3725.
(50) Tiedtke, D. B.; Cheung, T. T. P.; Leger, J.; Zisman, S. A.; Bergmeister, J. J.; Delzer, G. A. In: 13th Ethylene Producers Conference, 2001, 10: 1– 21.
(51) McCue, A. J.; Anderson, J. A. Recent advances in selective acetylene hydrogenation using palladium containing catalysts. *Front. Chem. Sci. Eng.* **2015**, 9, 142-153.

5.7 Appendix

5.A1 Hindered translational and rotational motion of adsorbates.

The hindered translational and rotational partition functions of adsorbates were approximated according to equations 5.A1 and 5.A3, respectively (see Sprowl, L. H.; Campbell, C. T.; Árnadóttir, L. *J. Phys. Chem. C* **2016**, 120, 9719-9731.)

In Equation 5.A1,

$$q_{trans} = \frac{M\left(\frac{\pi r_x}{T_x}\right) exp\left[-\frac{r_x}{T_x}\right] \exp\left[-\frac{1}{T_x}\right] I_0^2\left[\frac{r_x}{2T_x}\right]}{(1-\exp\left[-\frac{1}{T_x}\right])^2} \exp\left[\frac{2}{(2+16r_x)T_x}\right] \quad (5.A1)$$

where M is the number of surface sites; r_x is the ratio of the energy barrier height to the vibrational frequency times Planck's constant (i.e. $r_x = W_x/h\nu_x$), the dimensionless temperature T_x is $T_x = kT/h\nu_x$, and $I_0\left[\frac{r_x}{2T_x}\right]$ is the zero-order modified Bessel function of the first kind as a function of $\frac{r_x}{2T_x}$. Assuming that the translational energy barrier heights are the same in the x and y direction, then the corresponding frequencies can be calculated as

$$\nu_x = \nu_y = \left(\frac{W_x}{2mb^2}\right)^{\frac{1}{2}} \quad (5.A2)$$

where m is the adsorbate mass and b is the nearest-neighbor distance between surface atoms.

In Equation 5.A3,

$$q_{rot} = \frac{\left(\frac{\pi r_r}{T_r}\right)^{\frac{1}{2}} exp\left[-\frac{r_r}{2T_r}\right] \exp\left[-\frac{1}{2T_r}\right] I_0\left[\frac{r_r}{2T_r}\right]}{(1-\exp\left[-\frac{1}{T_r}\right])} \exp\left[\frac{1}{(2+16r_r)T_r}\right] \quad (5.A3)$$

where $r_r = W_r/h\nu_r$, $T_r = kT/h\nu_r$, and $\nu_r = \frac{1}{2\pi}\left(\frac{n^2 W_r}{2I}\right)^{\frac{1}{2}}$ given that I is the reduced moment of inertia which is equal to $I = \sum_i m_i d_i^2$. When calculating for I, m_i is the mass of each adsorbate atom and d_i is the distance between each adsorbate atom to the axis about which the adsorbate is being rotated. Tables 5.A1 and 5.A2 give the values used to calculate for q_{trans} and q_{rot} for each adsorbate molecule listed.

Table 5.A1 Summary of DFT calculations of energy barriers (W_x), vibrational frequencies (ν_x), and their ratios (r_x) for the hindered translation of H_2, C_2H_2, C_2H_4, and C_2H_6 on a BTOH surface.

Adsorbate	Energy Barrier W_x (eV)	Mass m (amu)	Frequency ν_x (s^{-1})	$r_x = W_x/(h\nu_x)$
H_2	0.060	2	4.51×10^{12}	3.2
C_2H_2	0.209	26	1.61×10^{12}	31.4
C_2H_4	0.154	28	1.77×10^{12}	21.1
C_2H_6	0.136	30	1.14×10^{12}	28.8

Table 5.A2 Summary of DFT calculations of energy barriers (W_r), vibrational frequencies (ν_r), and their ratios (r_r) for the hindered rotation of H_2, C_2H_2, C_2H_4, and C_2H_6 on a BTOH surface.

Adsorbate	Energy Barrier W_r (eV)	Reduced moment of inertia I (amu*Å^2)	Frequency ν_r (s^{-1})	$r_r = W_r/(h\nu_r)$
H_2	0.106	0.294	1.33×10^{13}	1.9
C_2H_2	0.309	14.6	3.21×10^{12}	23.3
C_2H_4	0.126	20.6	1.73×10^{12}	17.6
C_2H_6	0.059	6.42	3.17×10^{12}	4.48

5.A2 Results and Discussion

5.A2.1 Energy barriers of Horiuti-Polanyi and lattice hydride mechanisms.

Tables 5.A3 and 5.A4 list the elementary reaction steps for acetylene hydrogenation via the Horitui-Polanyi and lattice hydride mechanisms, respectively, along with the corresponding forward and reverse barriers between the intermediate states. Both the elementary reaction steps and the DFT-calculated energy barriers are used as input parameters in the MKMCXX software for microkinetic modeling.

Table 5.A3 The elementary reaction steps and corresponding forward and reverse barriers between the intermediate states in paths A-D via the Horiuti-Polanyi mechanism. Paths A and B are two different ethylene formation pathways while paths C and D are two different ethane formation pathways.

Path	Elementary reaction	Forward E_{act} (eV)	Backward E_{act} (eV)
A	H_2 (g) + _O2 ⇄ H_2_O2	-	0.0724
	H_2_O2 + _Ti1 ⇄ H_Ti1 + H_O2	0.5323	0.5578
	C_2H_2 (g) + _O1 ⇄ C_2H_2_O1	-	0.5047
	C_2H_2_O1 + H_Ti1 + _Ba1 ⇄ C_2H_3_Ba1 + _O1 + _Ti1	0.3224	0.1806
	C_2H_3_Ba1 + H_O2 ⇄ C_2H_4_Ba1 + _O2	0.0779	2.0820
	C_2H_4_Ba1 ⇄ C_2H_4 (g) + _Ba1	0.5436	-
B	H_2 (g) + _O2 ⇄ H_2_O2	-	0.0724
	H_2_O2 + _Ti1 ⇄ H_Ti1 + H_O2	0.5323	0.5578
	C_2H_2 (g) + _O1 ⇄ C_2H_2_O1	-	0.4909
	C_2H_2_O1 + H_Ti1 + _Ba1 ⇄ C_2H_3_Ba1 + _O1 + _Ti1	0.2985	0.2554
	C_2H_3_Ba1 + _Ti1 ⇄ C_2H_3_Ti + _Ba1	-	1.4146
	C_2H_3_Ti1 + H_O2 + _Ba2 ⇄ C_2H_4_Ba2 + _O2 + _Ti1	0.7925	1.0581
	C_2H_4_Ba2 ⇄ C_2H_4 + _Ba2	0.3243	-
C	H_2 (g) + _O2 ⇄ H_2_O2	-	0.0724
	H_2_O2 + _Ti1 ⇄ H_Ti1 + H_O2	0.5323	0.5578
	C_2H_4 (g) + _Ba2 ⇄ C_2H_4_Ba2	-	0.4995
	C_2H_4_Ba2 + H_Ti1 ⇄ C_2H_5_Ba2 + _Ti1	0.5033	0.0219
	C_2H_5_Ba2 + H_O2 ⇄ C_2H_6_Ba2 + _O2	0.0119	1.6607
	C_2H_6_Ba2 ⇄ C_2H_6 (g) + _Ba2	0.3400	-
D	H_2 (g) + _O2 ⇄ H_2_O2	-	0.0724
	H_2_O2 + _Ti1 ⇄ H_Ti1 + H_O2	0.5323	0.5578
	C_2H_4 (g) + _Ba2 ⇄ C_2H_4_Ba2	-	0.4995
	C_2H_4_Ba2 + H_Ti1 ⇄ C_2H_5_Ba2 + _Ti1	0.5033	0.0219
	C_2H_5_Ba2 + _Ti1 ⇄ C_2H_5_Ti1 + _Ba2	0.3913	1.1318
	C_2H_5_Ti1 + H_O2 + _Ba2 ⇄ C_2H_6_Ba2 + _O2 + _Ti1	0.5857	1.4567
	C_2H_6_Ba2 ⇄ C_2H_6 (g) + _Ba2	0.3025	-

Table 5.A4 The elementary reaction steps and corresponding forward and reverse barriers between the intermediate states in paths E-H via the lattice hydride mechanism. Paths E and F are two different ethylene formation pathways while paths G and H are two different ethane formation pathways.

Path	Elementary reaction	Forward E_{act} (eV)	Backward E_{act} (eV)
E	C_2H_2 (g) + _O1 ⇄ C_2H_2_O1	-	0.4714
	C_2H_2_O1 + H_Ti1 + _Ba1 ⇄ C_2H_3_Ba1 + _Ti1 + _O1	0.5338	0.6804
	C_2H_3_Ba1 + H_Ti1' ⇄ C_2H_4_Ba1 + _Ti1'	0.4784	1.6813
	C_2H_4_Ba1 ⇄ C_2H_4 (g) + _Ba1	0.4785	-
	H_2 (g) + _O2 ⇄ H_2_O2	-	0.0868
	H_2_O2 + _Ti1 + _Ti1' ⇄ H_Ti1 + H_Ti1' + _O2	0.7969	1.2693
F	C_2H_2 (g) + _O1 ⇄ C_2H_2_O1	-	0.4371
	C_2H_2_O1 + H_Ti1 ⇄ C_2H_3_Ti1 + _O1	0.4593	1.6836
	C_2H_3_Ti1 + H_Ti1' ⇄ C_2H_3--H_Ti1 + _Ti1'	0.6538	0.0294
	C_2H_3--H_Ti1 ⇄ C_2H_3-H_Ti1	0.1828	0.0345
	C_2H_3-H_Ti1 + _Ba2 ⇄ C_2H_4_Ba2 + _Ti1	-	0.8351
	C_2H_4_Ba2 ⇄ C_2H_4 (g) + _Ba2	0.3814	-
	H_2 (g) + _O2 ⇄ H_2_O2	-	0.0868
	H_2_O2 + _Ti1 + _Ti1' ⇄ H_Ti1 + H_Ti1' + _O2	0.7969	1.2693
G	C_2H_4 (g) + _Ba1 ⇄ C_2H_4_Ba1	-	0.4510
	C_2H_4_Ba1 + H_Ti1 ⇄ C_2H_5_Ba1 + _Ti1	0.4760	0.0613
	C_2H_5_Ba1 + H_Ti1' ⇄ C_2H_6_Ba1 + _Ti1'	0.8677	1.9605
	C_2H_6_Ba1 ⇄ C_2H_6 (g) + _Ba1	0.2633	-
	H_2 (g) + _O2 ⇄ H_2_O2	-	0.0868
	H_2_O2 + _Ti1 + _Ti1' ⇄ H_Ti1 + H_Ti1' + _O2	0.7969	1.2693
H	C_2H_4 (g) + _Ba4 ⇄ C_2H_4_Ba4	-	0.4419
	C_2H_4_Ba4 + H_Ti1' ⇄ C_2H_5_Ba4 + _Ti1'	0.6295	0.0400
	C_2H_5_Ba4 + _Ti1' ⇄ C_2H_5_Ti1' + _Ba4	0.3030	0.8491
	C_2H_5_Ti1' + H_Ti + _Ba1 ⇄ C_2H_6_Ba1 + _Ti1 + _Ti1'	1.2727	1.9917
	C_2H_6_Ba1 ⇄ C_2H_6 (g) + _Ba1	0.2518	-
	H_2 (g) + _O2 ⇄ H_2_O2	-	0.0868
	H_2_O2 + _Ti1 + _Ti1' ⇄ H_Ti1 + H_Ti1' + _O2	0.7969	1.2693

5.A2.2 A reasoning for the absence of H1 lattice hydride involvement in acetylene semi-hydrogenation. Information found in Figures 5.A1 and 5.A2 are used to explain why lattice hydrides are most likely not incorporated into the acetylene semi-hydrogenation reaction. Figure 5.A1 shows the energy profiles for acetylene semi-hydrogenation to ethylene via the Horiuti-Polanyi mechanism. Path B (from the main text) describes the hydrogenation of acetylene by a surface hydride and proton and was deemed as the pathway that forms ethylene at the fastest rate.

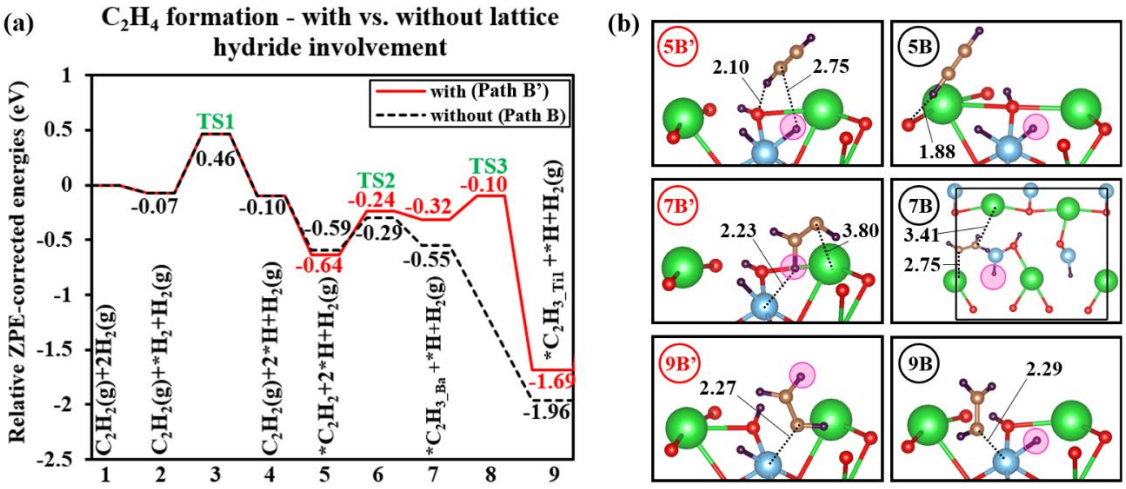

Figure 5.A1 Energy profile of the two possible pathways for ethylene formation via the Horiuti-Polanyi mechanism with (red line) and without (black dashed line) the involvement of the H1 lattice hydride (a) and the key intermediate structures (b). In Figure 5.A1b, the lattice hydride is highlighted in pink. Additionally, in Figure 5.A1b, states 5B, 7B, and 9B represent intermediate states of Path B which do not include the lattice hydride in the reaction. All energies listed are ZPE corrected, and all atomic distances are reported in units of Å.

We also investigated a Path B' in which the H1 lattice hydride is involved in the first acetylene hydrogenation instead of the surface hydride, as shown in Path B. Our findings reveal that the first acetylene hydrogenation barrier is higher in Path B' (E_a = 0.40 eV; TS2B') than in Path B (E_a = 0.30 eV; TS2B). Additionally, rotating the vinyl

intermediate about the surface Ba atom to form the C-Ti1 bond requires 0.22 eV of energy in Path B' whereas in Path B, it is a barrierless process. Therefore, it is more favorable for the lattice hydride to remain on the surface and for the surface hydride to be utilized in the hydrogenation reaction.

Moreover, Figure 5.A2 shows that 1.95 eV of energy is required for the lattice hydride to switch positions with the surface hydride. Because this energy barrier is too high to cross over under the conditions we are studying, this further shows how the lattice hydride could not have interchanged positions with the adjacent surface hydride and, as a result, could not have been involved in the acetylene semi-hydrogenation reaction.

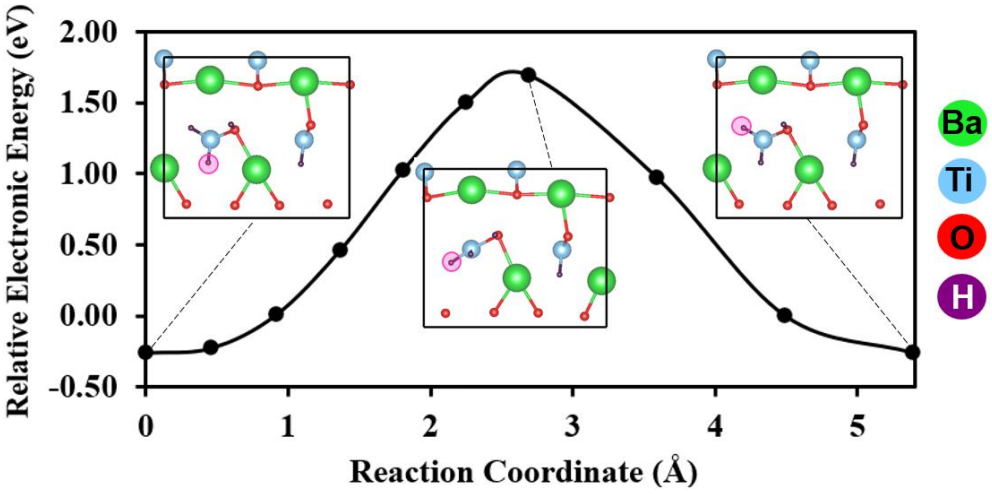

Figure 5.A2 Minimum energy path of the H1 lattice hydride switching positions with a surface hydride and the structures for the initial, transition, and final states. The lattice hydride is highlighted in pink.

5.A2.3 Explanation of C_2H_4 formation path selectivity

Table 5.A5 The C_2H_4 production rate via Path A and Path B across a temperature range of 373 – 673 K. The C_2H_4 production rates that are faster in one path as compared to the other are highlighted in yellow.

	C_2H_4 production rate (mol s^{-1} unit $cell^{-1}$)	
Temperature (K)	**Path A**	**Path B**
373	0.30	0.28
423	1.67	2.20
473	2.57	8.79
523	2.42	22.43
573	2.17	44.56
623	1.99	76.26
673	1.88	117.54

Table 5.A5 shows that at a lower temperature (373 K), the C_2H_4 production rate is slightly faster via Path A than B. Towards higher temperatures (423 – 673 K), the C_2H_4 production rate is faster via Path B than A. To understand the temperature dependence of path selectivity for C_2H_4 formation, the DRCs and the forward/reverse rates of key elementary reaction steps in Path A and B are analyzed. Upon initial surveying of the C_2H_4 formation via Path A and B (Figures 5.A3a-b), one can see that the main difference between the two paths are the energy barriers corresponding to the 1st and 2nd hydrogenation steps and also the C_2H_4 desorption step. In Path A, the 1st and 2nd hydrogenation steps have relatively low forward barriers ($\leq$ 0.34 eV) and a C_2H_4 desorption barrier of 0.55 eV. On the other hand, the 1st hydrogenation step in Path B has a relatively low forward barrier (0.31 eV), a higher 2nd hydrogenation barrier (0.79 eV), and a lower C_2H_4 desorption barrier of 0.33 eV. If the reaction were to only proceed in the forward direction, then one could say that Path A would be the most favorable pathway for C_2H_4 formation because the 1st and 2nd hydrogenation barriers in Path A are lower than in Path B. However, reaction

coordinates can be traversed in both the forward and reverse direction, and therefore, it is also important to account for the reverse rates of elementary steps.

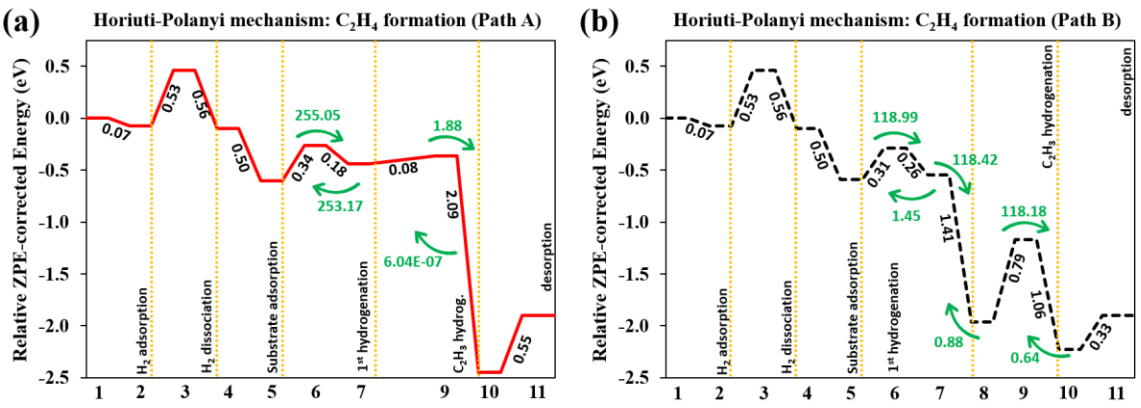

Figure 5.A3 Semi-hydrogenation of C_2H_2 to C_2H_4 via the Horiuti-Polanyi mechanism on BTOH (211)-Ba_2O_4H via (a) Path A (b) Path B. The forward and reverse rates of certain key steps at 673 K are labeled in green on both energy profiles and have units of mol s^{-1} unit $cell^{-1}$. The energy differences between two states are listed in black below the energy profile.

The forward and reverse rates of the 1st and 2nd hydrogenation steps in Path A and B are shown in Figures 5.A3a-b. One can see that at 673 K, the forward rate for the 1st hydrogenation step in Path A (states 5→7) is 255.05 mol s^{-1} unit $cell^{-1}$. However, because the reverse energy barrier is also relatively low (0.18 eV), the reverse rate (i.e., the conversion of adsorbed C_2H_3 back to adsorbed C_2H_2, 253.17 mol s^{-1} unit $cell^{-1}$) is almost the same as the forward rate. This implies that a majority of the C_2H_3 being formed on the surface is being converted back to C_2H_2. Now, the remaining C_2H_3 on the surface that was not converted back to C_2H_2 could then continue on forward and be converted to product at a rate of 1.88 mol s^{-1} unit $cell^{-1}$ (states 7→10). Since the reverse barrier corresponding to the conversion of C_2H_4 back to C_2H_3 (states 10→7) is relatively high (2.09 eV), the rate

for this process to occur is essentially zero and the C_2H_3 that is hydrogenated is an irreversible process.

For Path B, the forward rate for the 1st hydrogenation step (states 5→7) is 118.99 mol s^{-1} unit $cell^{-1}$ but the reverse rate is only 1.45 mol s^{-1} unit $cell^{-1}$. This is because the next step (states 7→8), which corresponds to the re-orientation of C_2H_3 on the surface, is a barrierless process. Therefore, a majority of the C_2H_3 formed on the surface in state 7 will proceed to state 8 at a rate of 118.42 mol s^{-1} unit $cell^{-1}$. Because the reverse barrier (state 8→7) is relatively high (1.41 eV), the reverse rate (0.88 mol s^{-1} unit $cell^{-1}$) is much lower than the forward rate of 118.18 mol s^{-1} unit $cell^{-1}$ to hydrogenate C_2H_3 to form C_2H_4.

It is important to note that because there is a greater net rate of C_2H_3 formation on the surface in Path B than in A, the steady-state surface coverage of C_2H_3 in Path B is 2.46E-03 which is larger than the steady-state C_2H_3 surface coverage of 4.07E-10 in Path A. Therefore, there is more C_2H_3 available in Path B than in A to form C_2H_4 and, hence, a greater C_2H_4 production rate via Path B at higher temperatures. Further details on determining rate-limiting steps of a multistep reaction can be found in Murdoch, J. R. *J. Chem. Educ.* **1981**, 58, 32-36.

The DRCs of certain elementary reaction steps in Path A and B further show the influence of these steps on the overall rate of C_2H_4 formation (Figure 5.A4). Even though the forward energy barrier for the 2nd hydrogenation (i.e. C_2H_3 hydrogenation) is much higher in Path B than in Path A (0.79 eV vs. 0.08 eV, respectively), this step is not the most rate-controlling step at higher temperatures (> ~473 K) for either paths. The most rate-controlling steps are actually the C_2H_3 hydrogenation step in Path A and the 1st

hydrogenation step in Path B, which explains why Path B is faster than A at higher temperatures. At a lower temperature of 373 K, one can see that the most rate-controlling step in Path A and B is only the H_2 dissociation step. Because the 2nd hydrogenation step no longer has a large influence on the overall C_2H_4 formation rate at 373 K for both paths and the DRC for H_2 dissociation is higher in Path A than B, this explains why the rate of C_2H_4 formation is faster via Path A than B.

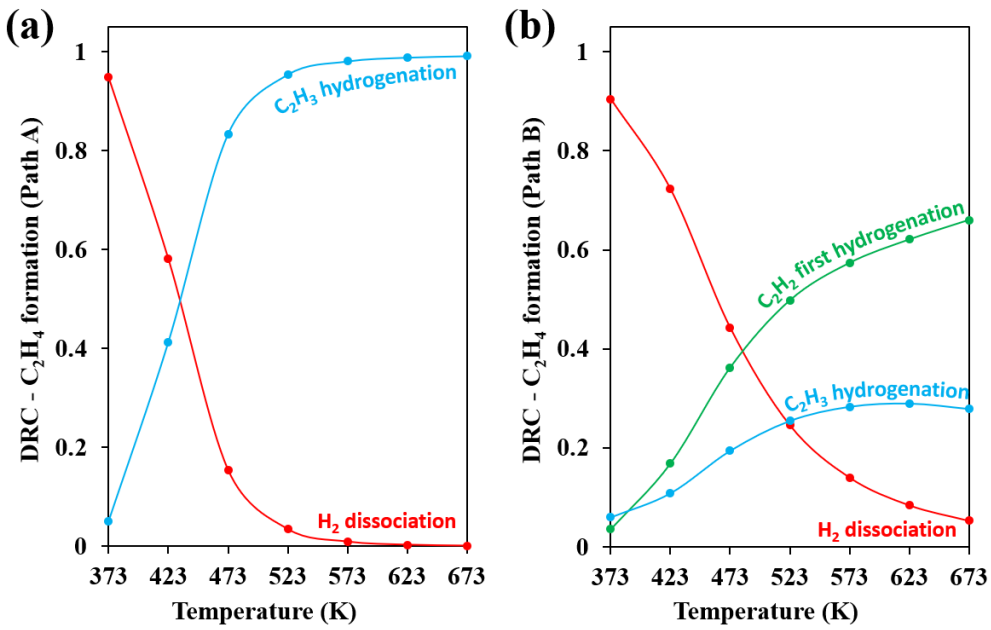

Figure 5.A4 The degree of rate control (DRC) of key elementary reaction steps in Path A (a) and Path B (b).

CHAPTER 6
First principles investigation of the selective hydrogenation of C=O in crotonaldehyde over a stable perovskite oxyhydride surface

6.1 Abstract

A new class of mixed-anion system, called perovskite oxyhydrides (POHs), has been shown to be an effective support for hydrogenation reactions and also exhibit activity for ammonia synthesis. However, their activity and selectivity in the selective hydrogenation of α,β-unsaturated aldehydes remain unclear. Here, the selective hydrogenation of crotonaldehyde, via the Horiuti-Polanyi mechanism, was investigated on the (211)-Ba_2O_4H surface termination of the prototypical $BaTiO_{2.5}H_{0.5}$ (BTOH) perovskite oxyhydride. Using first principles density functional theory, possible minimum-energy pathways for crotonaldehyde hydrogenation to form either crotyl alcohol or butanal have been identified. It was determined that when the C=O bond of crotonaldehyde is aligned with dissociated H_2 on the BTOH surface, crotyl alcohol formation is the most favorable pathway and would be the expected major product to form. This is because the surface vacancies provide an avenue to form a proton and hydride from H_2 dissociation at the surface which are conducive for crotyl alcohol formation due to the favorable charge interactions between 1) the surface hydride and carbonyl carbon in crotonaldehyde and 2) between the proton and partially negative O atom in crotonaldehyde. The charge interactions between the H species and carbon atoms in crotonaldehyde's C=C bond are not as favorable and, therefore, butanal formation is not preferred. The present findings provide insights on the role BTOH lattice hydrides and surface anion vacancies play in general selective hydrogenation of α,β-unsaturated aldehydes.

6.2 Introduction

The $BaTiO_{3-x}H_x$ perovskite oxyhydride is an anion-tuned $BaTiO_3$ material where lattice O^{2-} are randomly replaced by H^- upon reduction.[1,2,3] This material is not only a more efficient catalyst support for CO_2 methanation and ammonia synthesis than $BaTiO_3$, but $BaTiO_{3-x}H_x$ (with x = 0.5) is itself active for ammonia synthesis.[4,5,6] These findings show the potential of the $BaTiO_{3-x}H_x$ perovskite oxyhydride as a catalyst for hydrogenation reactions and have since led to a greater interest in studying the role of the material's lattice hydrides in different types of hydrogenation reactions. From our previous studies, we found that the hydride vacancies on the surface of a prototypical perovskite oxyhydride, $BaTiO_{2.5}H_{0.5}$ (BTOH), play a significant role in ammonia synthesis and the semi-hydrogenation of acetylene. In ammonia synthesis, the hydride vacancy in the BTOH (210) surface sublayer is crucial for N-N cleavage.[7] On the other hand, in acetylene semi-hydrogenation, the vacancy is necessary to stabilize the C_2H_3 intermediate which is key to selectively produce C_2H_4 instead of C_2H_6 over the BTOH (211)-Ba_2O_4H surface termination. In this work, we aim to understand the role BTOH lattice hydrides and hydride vacancies play in the selective hydrogenation of α,β-unsaturated aldehydes, specifically of crotonaldehyde as a probe reaction.

The selective hydrogenation of α,β-unsaturated aldehydes is an important industrial process to produce unsaturated alcohols that have applications in the food, pharmaceuticals, and fragrance industries.[8,9,10,11] The challenge is producing the unsaturated alcohol over the saturated aldehyde since hydrogenation of the C=C bond is thermodynamically more favorable than the C=O bond by 35 kJ/mol.[12] Industrially, α,β-

unsaturated aldehydes are selectively hydrogenated to its corresponding unsaturated alcohol using the $NaBH_4$ or $LiAlH_4$ reagents.[13,14] However, the reducing agents must be used in stoichiometric amounts and require careful handling under anhydrous conditions. Therefore, there have been an abundance of research focused on designing active and selective heterogeneous catalysts for this reaction by taking advantage of the following effects: the electronic, synergetic, and confinement/steric effects.[15] These effects are exemplified by catalysts such as $Pt_3Co/Co(OH)_2$,[16] Pt/TiO_2,[17] and Rh_1/MoS_2,[18] respectively.

Although metal oxides are commonly used as catalyst supports for this type of reaction,[19,20,21,22] a recent study has shown metal-free ceria nanorods exhibiting high selectivity towards the hydrogenation of crotonaldehyde to crotyl alcohol under ambient conditions.[23] The key characteristic causing this selectivity and activity on ceria nanorods is the high density of surface oxygen vacancies that: 1) allow for facile heterolytic H_2 dissociation and 2) provide a site for crotonaldehyde adsorption via the C=O bond which is then subsequently hydrogenated. This investigation shows how surface vacancies on a metal oxide can improve the activity and selectivity of the material for selective hydrogenation without having to use expensive noble metals. This leads to the question: what other key metal oxide features may be important for selective hydrogenation reactions?

The BTOH perovskite oxyhydride is a unique metal oxide material as its surface terminations expose hydrides or hydride vacancies which have been proposed to partake in hydrogenation reactions.[5,7] Our aim, in this work, is to investigate the role of lattice

hydrides and surface hydride vacancies in the selective hydrogenation of crotonaldehyde. Under the typical conditions for selective hydrogenation of crotonaldehyde, the (211)-Ba_2O_4H surface termination of BTOH was determined to be the most stable[24] and, therefore, used as our surface model in this work. Below, we introduce the computational methods used followed by a description of our surface model.

6.3 Computational Methods

All spin-polarized density functional theory (DFT) calculations were performed using the Vienna *ab initio* Simulation Package (VASP).[25,26] The electron exchange and correlation energies were treated using the general-gradient approximation (GGA) functional, Perdew-Burke-Ernzerhof (PBE),[27] and the electron-core interactions were described by the projector augmented-wave (PAW) potentials.[28] A kinetic energy cutoff of 450 eV was used for the plane waves and the DFT-D3 method was used to account for the van der Waals interactions.[29] The force convergence criterion is 0.02 eV/Å and the energy convergence criterion is 10^{-5} eV. The partial atomic charges were obtained using Bader charge analysis.[30]

The Ba_2O_4H termination of the BTOH(211) surface was used as the surface model for mechanistic studies as it was determined to be the most stable termination[24] under crotonaldehyde selective hydrogenation conditions (323 K, 1 bar).[23] The slab model for the (211)-Ba_2O_4H BTOH surface termination is a 2×2 supercell containing eight layers with the top four layers allowed to relax in the calculations. Along the z direction of the surface slab is a vacuum layer of 15 Å. We employed a 3×3×1 Monkhorst-Pack scheme[31] to sample

the Brillouin zone. In order to compensate the net dipole moment along the surface normal due to slab asymmetry, a dipole correction[32] was included within the vacuum region.

Adsorption energies were calculated with Equation (6.1)

$$E_{ads} = E_{surface+adsorbate} - (E_{surface} + E_{adsorbate}) \quad (6.1)$$

where $E_{surface+adsorbate}$ is the energy of the adsorbate-slab system in which the adsorbates are either a reactant, intermediate, or product; $E_{surface}$ is the energy of the clean surface; and $E_{adsorbate}$ is the energy of isolated adsorbate molecules (H_2, crotonaldehyde, crotyl alcohol, butanal). $E_{adsorbate}$ was computed by placing each isolated adsorbate molecule in a 15×15×15 $Å^3$ cubic cell. Transition state search was accomplished by using both the climbing-image nudged elastic band (CI-NEB)[33] and the dimer method[34] as implemented in the VASP-VTST package by Henkelman and Jónsson. The force convergence criterion for transition state search was set to 0.05 eV/ Å. Transition states were verified by vibrational frequency analysis.

The Gibbs free energy of crotyl alcohol or butanal desorption from the surface can be approximated with Equation (6.2)

$$\Delta G_{des} = \Delta H_{des} - T\Delta S_{des} \approx (\Delta E_{elec} + \Delta E_{vib}) - T\Delta S_{des} \quad (6.2)$$

where ΔE_{elec} is the change in electronic energy, ΔE_{vib} is the change in vibrational energy and includes the zero-point energy, T is the reaction temperature at 323 K, and ΔS_{des} is the change in entropy between the adsorbed state (initial state) and the desorbed state (final state). The vibrational frequencies of the isolated products (i.e., either crotyl alochol or butanal) and the adsorbed products were computed using the finite-difference method as implemented in VASP. By approximating the rotational and vibrational entropic

contributions to be less than the translational entropic contribution, ΔS_{des} can be calculated with Equation (6.3)

$$\Delta S_{des} = S_{prod} - S_{prod^*} = S_{prod} - \left(S_{prod} - S_{prod,trans}\right) = S_{prod,trans} \qquad (6.3)$$

where S_{prod} is the total entropy of the gaseous products, S_{prod*} is the total entropy of the adsorbed products, and $S_{prod,trans}$ is the translational entropy of the gaseous products. The Sackur-Tetrode equation was used to calculate the translational entropy of NH_3 in the gaseous state.[35]

6.4 Results and Discussion

Crotonaldehyde (CRAL) contains two types of double bonds (i.e., C=O and C=C) and can be selectively hydrogenated to form either crotyl alcohol (CROL) or butanal. By comparing the energy profiles corresponding to the formation of either product over a stable BTOH surface, we can determine the selective product over the catalytic surface. We start with a description of the BTOH surface structure that is stable under the conditions for selective hydrogenation of CRAL.

6.4.1 Surface structure of BTOH (211)-Ba2O4H termination. Previously, we identified stable surface terminations of BTOH under catalytically relevant temperatures and pressures.[24] From these results, it can be deduced that under typical conditions for the selective hydrogenation of CRAL,[23] the most stable BTOH surface termination is (211)-Ba_2O_4H. Figure 6.1 depicts the side and top views of the 2×2 slab model for this nonstoichiometric termination. The slab model contains surface Ba, O, and H atoms as well as hydride vacancies that each expose one subsurface Ti. The surface vacancies are hypothesized to be involved in H_2 heterolytic dissociation as this process over metal oxides

is typically more kinetically favored than H_2 homolytic dissociation.[36,37] Therefore, in this work, the source of H species will be generated via H_2 heterolytic dissociation to form one surface hydride occupying the V1 vacancy (and bonded to subsurface Ti1) and one proton bonded to surface O2.

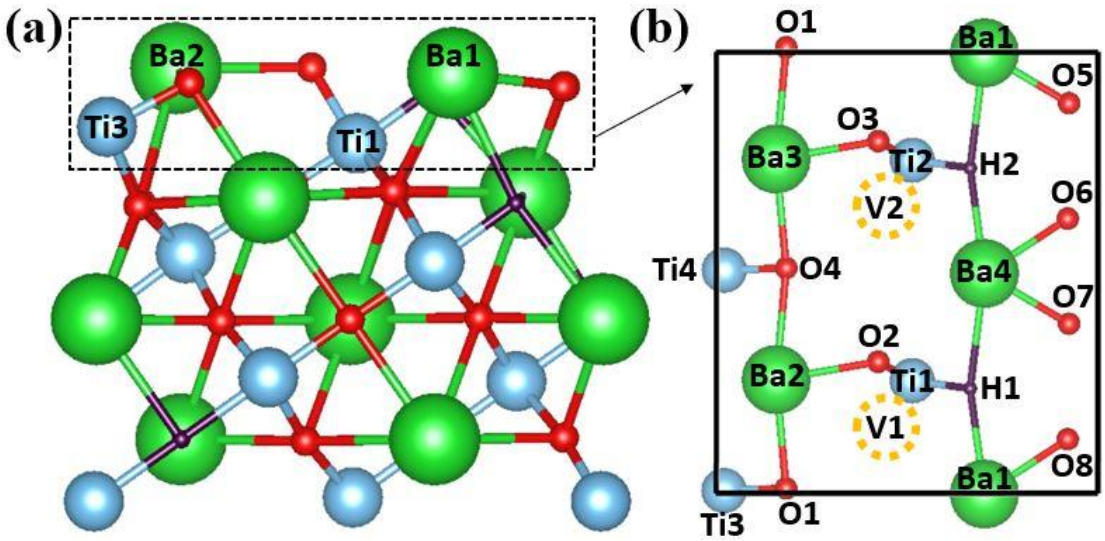

Figure 6.1 The structure model of the $BaTiO_{2.5}H_{0.5}$ (211)-Ba_2O_4H surface termination: (a) side view of the slab; (b) top view of the slab's top two layers. The surface hydride vacancies are represented by yellow dotted circles labeled as V1 or V2.

6.4.2 Overview of the selective hydrogenation of CRAL on BTOH (211)-Ba2O4H. The Horiuti-Polanyi mechanism has long been established as the common route for hydrogenation reactions over heterogeneous catalysts. In this mechanism, H species that are formed from initial H_2 dissociation, are sequentially added to unsaturated compounds.[38] In the selective hydrogenation of CRAL, there are four possible routes that lead to the formation of either butanal or CROL as shown in Figure 6.2 Routes 1 and 2 follow the path to butanal formation in which a H atom is initially added to either C^1 or C^2,

respectively, while routes 3 and 4 follow the path to CROL formation in which a H atom is initially added to either C^3 or O^4, respectively.

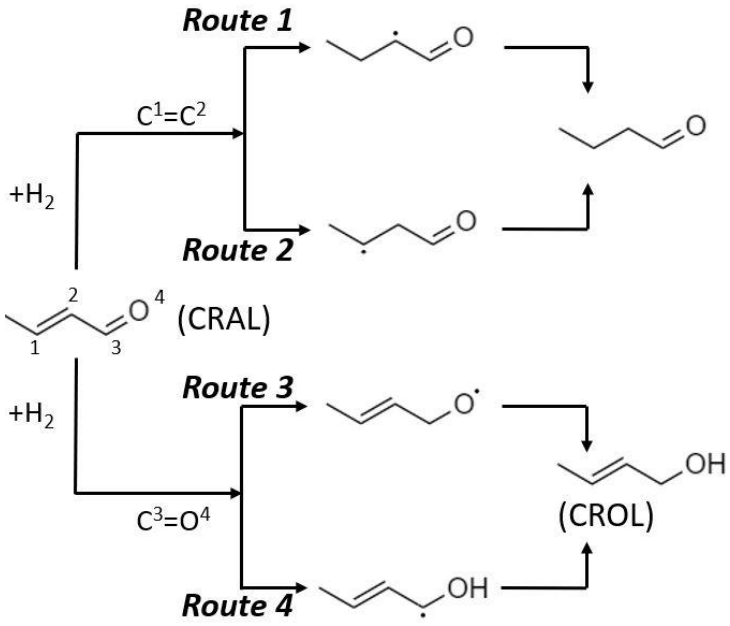

Figure 6.2 The four hydrogenation routes to convert CRAL to either butanal (routes 1 and 2) or CROL (routes 3 and 4). In each route, the H atom is added to different positions of CRAL.

6.4.3 CRAL adsorption over the hydrogenated BTOH surface. The adsorption configurations of CRAL over the hydrogenated BTOH surface were investigated prior to exploring the selective hydrogenation routes. The most relevant configurations are those in which the unsaturated bonds of CRAL are close enough to dissociated H_2 for subsequent hydrogenation. Figure 6.3 shows that in the CRAL_adsorption_1 orientation, the C=O bond of CRAL is in close proximity (i.e. < 3.2 Å) to either the surface proton or surface hydride that was formed from H_2 dissociation whereas in the CRAL_adsorption_2 orientation, the C=C bond is closer. Hence, CRAL_adsorption_1 is the most suitable for

C=O hydrogenation to form CROL and CRAL_adsorption_2 is the most suitable for C=C hydrogenation to form butanal. While it is possible to form CROL from the CRAL_adsorption_2 position (see section 6.A1 of Appendix [section 6.7]), our AIMD calculations show that the intermediate and surface atoms must shift and migrate until the intermediate's O atom is in close enough proximity to dissociated H_2 for H addition.

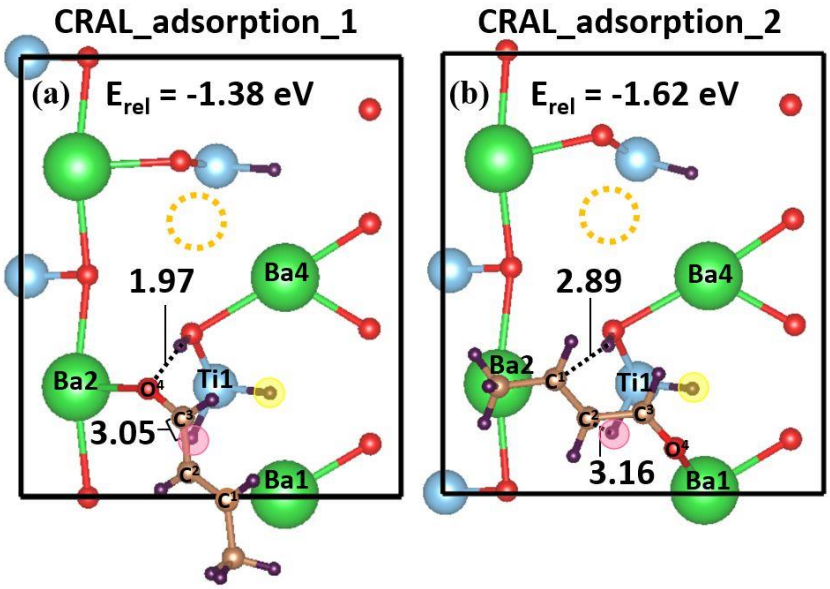

Figure 6.3 The two relevant adsorption orientations of CRAL over hydrogenated BTOH: (a) the C=O bond and (b) the C=C bond in close proximity to dissociated H_2. The relative energies of each structure are shown at the top of (a) and (b). The hydride highlighted in yellow represents the lattice hydride (i.e., the hydride that is part of the BTOH catalyst) and the hydride highlighted in pink represents the surface hydride (i.e., the hydride formed after H_2 heterolytic dissociation). All atomic distances are reported in units of Å.

Investigating different possible migration pathways of CRAL or its corresponding hydrogenated intermediate over the surface would be important when finding the most favorable pathway for CRAL hydrogenation. However, in this work, we are most interested in comparing the energy barriers of C=C and C=O hydrogenation to determine product

selectivity over BTOH. Therefore, we only explored CROL formation pathways from the CRAL_adsorption_1 orientation and butanal formation pathways from CRAL_adsorption_2.

6.4.4 Forming CROL from CRAL_adsorption_1. Figure 6.4a shows the energy profiles of only the intermediate states involved in the formation of CROL from C=O hydrogenation in CRAL.

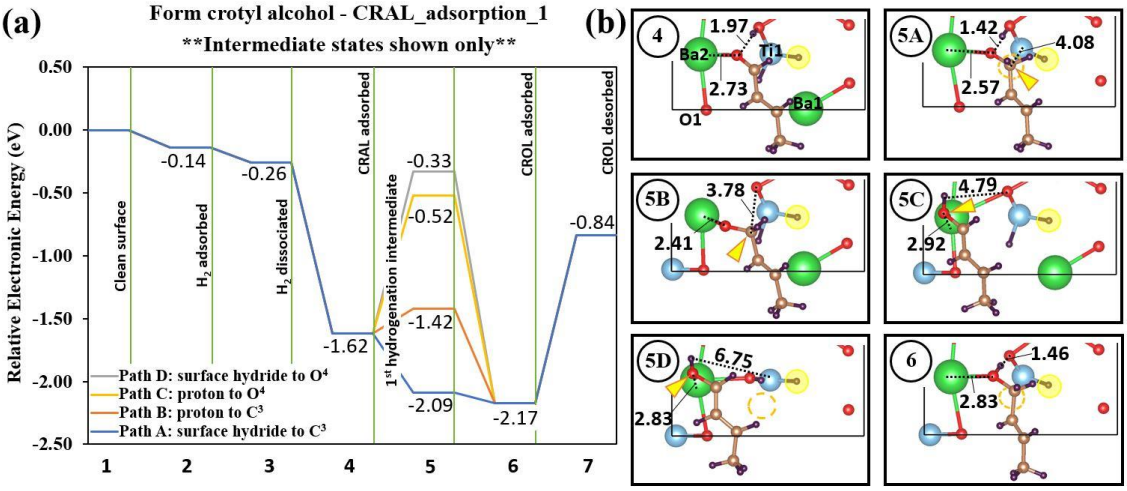

Figure 6.4 Energy profile of the four possible pathways for CROL formation from CRAL adsorbed in the CRAL_adsorption_1 orientation (a) and the key intermediate structures (b). For reference, the lattice hydride is highlighted in yellow and the CRAL atom being hydrogenated is indicated by the yellow-orange arrow in Figure 6.4b. All atomic distances are reported in units of Å.

The mechanism begins with H_2 adsorption (state 2) and H_2 heterolytic dissociation (state 3) over the clean surface. From there, CRAL adsorbs onto the hydrogenated surface in the CRAL_adsorption_1 orientation (state 4, see structure in Figure 6.4b) and undergoes hydrogenation to form states 5A-D. Afterwards, the state 5 intermediate is hydrogenated to form CROL (state 6) which is desorbed to regenerate the catalytic surface in state 7.

There are various structures for state 5 depending on which H species is added to CRAL first and at which atom position. State 5A has the lowest relative energy and is formed when the surface hydride (from heterolytic H_2 dissociation) hydrogenates CRAL at the carbonyl carbon, C^3. State 5D has the highest relative energy and is formed when the surface hydride hydrogenates CRAL at the oxygen atom, O^4.

Since the energy differences between states 4 and 5C/5D are greater than 1 eV, it implies that the energy barrier between these states would also be greater than 1 eV which is relatively high. Hence, we were only concerned with calculating the energy barriers corresponding to the transition from states 4 to 5A/5B as these barriers would potentially be lower than 1 eV. Figure 6.5a compares the energy barriers of pathways A and B while Figure 6.5b shows the corresponding key intermediate structures. In both pathways, initial barrierless H_2 adsorption (state 2) is followed by heterolytic H_2 dissociation (states 2-3, E_a = 0.53 eV) and barrierless CRAL adsorption (state 4). In Pathway A, the surface hydride is added to CRAL at C^3 (states 4-5A, E_a = 0.25 eV) followed by the proton at O^4 (states 5A-6A, barrierless). Alternatively, in Pathway B, the proton first hydrogenates CRAL at C^3 (states 4-5B, E_a = 1.32 eV). Since the first hydrogenation barrier of CRAL via Pathway B is much higher than in Pathway A, the second hydrogenation barrier of pathway B was not investigated further. Therefore, when CRAL is initially adsorbed in the CRAL_adsorption_1 orientation, the most likely pathway for CROL formation is via Pathway A.

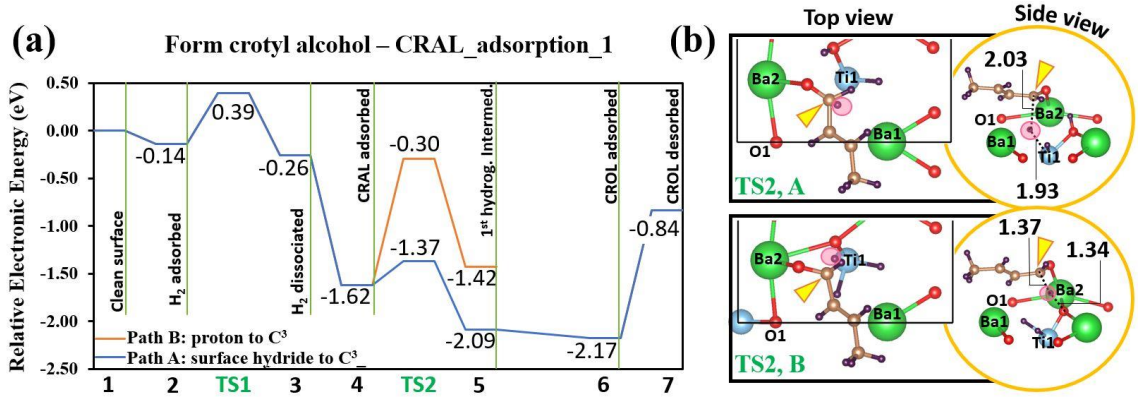

Figure 6.5 A comparison of the energy barriers in pathways A and B. Figure 5b shows the TS2 structures for pathways A (top) and B (bottom). The H atom being added to CRAL is highlighted in pink and the atom in CRAL that is being hydrogenated is indicated by the yellow-orange arrow in Figure 5b. All atomic distances are reported in units of Å.

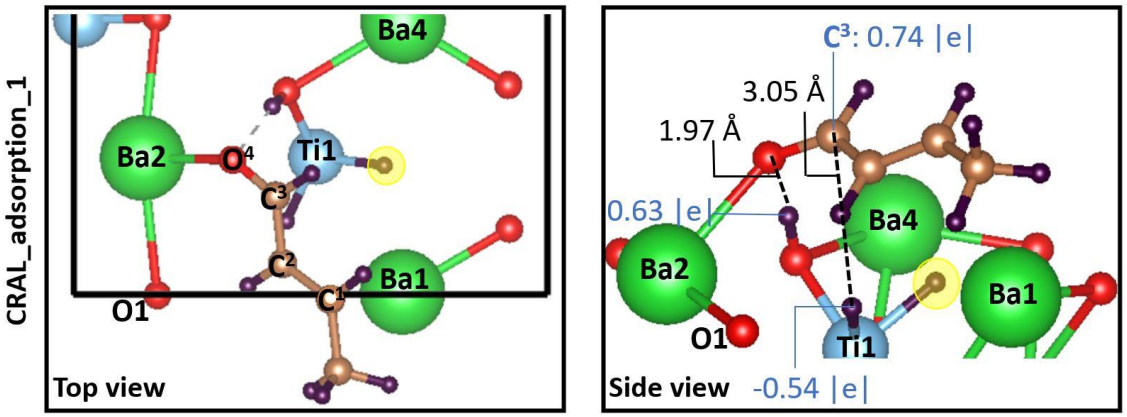

Figure 6.6 The top and side views of CRAL_adsorption_1. The atoms are labeled in the top view panel and the Bader charges and atomic distances are shown in the side view panel. The lattice hydride is highlighted in yellow.

A reason for why TS2 of Pathway A is much lower in relative energy than that of pathway B can be explained by analyzing the Bader charges of the atoms in the CRAL_adsorption_1 structure (state 4, Figure 6.4b) as shown in Figure 6.6. In Pathway A, the first hydrogenation of CRAL involves a negatively charged surface hydride (-0.54 |e|) forming a bond with positively charged C^3 (+0.74 |e|). In Pathway B, the first

hydrogenation of CRAL involves a positively charged proton (+0.63 |e|) forming a bond with C^3. Hence, this unfavorable interaction between the positively charged proton and positively charged C^3 can explain the higher TS2 relative energy in Pathway B.

6.4.5 Forming butanal from CRAL_adsorption_2. Figure 6.7a shows the energy profile of only the intermediate states involved in the formation of butanal while Figure 6.7b shows the key intermediate structures.

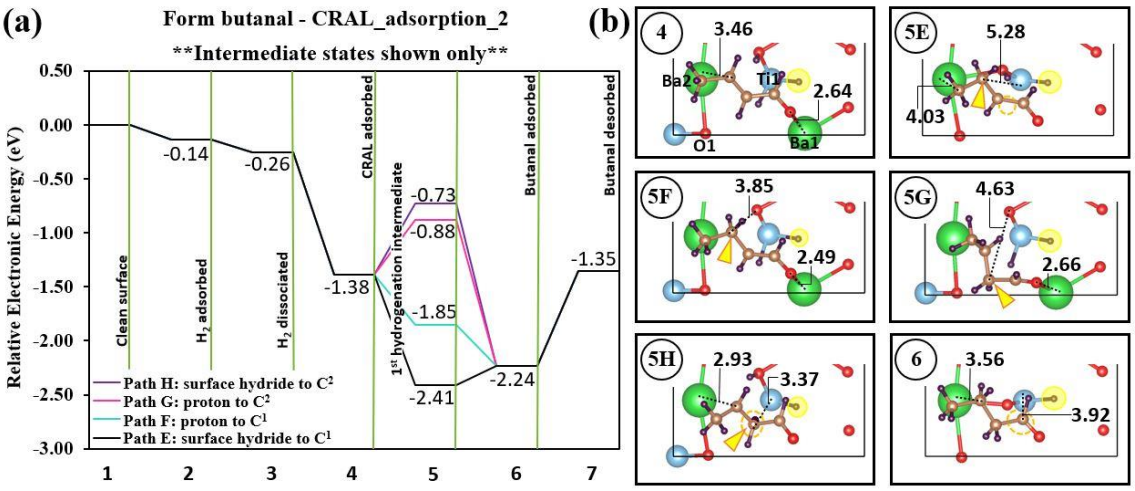

Figure 6.7 Energy profile of the four possible pathways for butanal formation from CRAL adsorbed in the CRAL_adsorption_2 orientation (a) and the key intermediate structures (b). For reference, the lattice hydride is highlighted in yellow and the atom in CRAL being hydrogenated is indicated by the yellow-orange arrow in Figure 7b. All atomic distances are reported in units of Å.

States 1-4 are the same for pathways E-H and correspond to H_2 adsorption, H_2 dissociation, and CRAL adsorption on the hydrogenated BTOH surface via the CRAL_adsorption_2 orientation. State 5 is where we begin to see differences. As described previously, the various state 5 structures can be formed depending on which H species is

added to CRAL first and at which C position. State 5E has the lowest relative energy and is formed when the surface hydride hydrogenates CRAL at C^1. State 5H has the highest relative energy and is formed when the surface hydride hydrogenates CRAL at C^2. Only the energy barriers between states 4 and 5E/F were investigated since the energy difference between states 4 and 5G/H are already greater than the first hydrogenation barrier of CROL in Pathway A (0.25 eV).

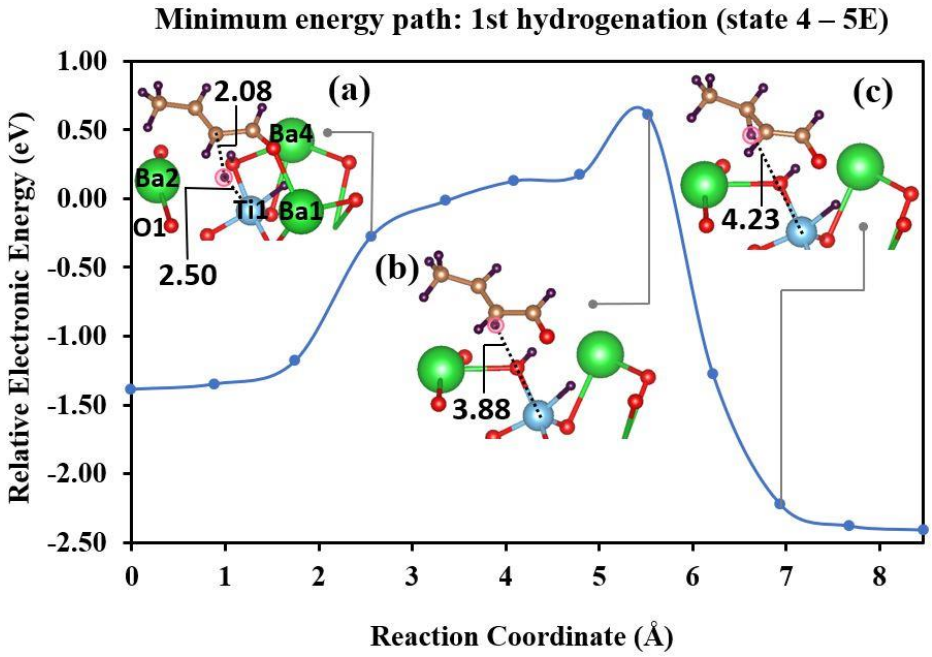

Figure 6.8 The minimum energy path (determined by crude NEB calculations) of the surface hydride hydrogenating CRAL at the C^1 atom to form state 5E. The structures of different NEB images are shown in (a)-(c). The H atom being added to CRAL is highlighted in pink.

In the transition from state 4 to 5E, the long reaction coordinate (> 8 Å) is due to the great distance between the surface hydride and C^1. Figure 6.8 shows that the hydrogenation of C^1 by the surface hydride occurs after initial bond formation between the

surface hydride and C^2 (see Figure 6.8b for structure). This is because the distance between the surface hydride and C^2 is much closer than between the surface hydride and C^1. In order for C^1 to then be hydrogenated, the C^2-H bond must first be broken in order to form the C^1-H bond (see Figure 6.8c for structure). However, this overall process requires a very large energy barrier of ~2 eV and, therefore, the hydrogenation of C^1 by the surface hydride will most likely not occur.

The transition from state 4 to 5F is more favorable than the transition from state 4 to 5E because of the lower energy barrier (0.69 eV). Further calculations show that the energy barrier of the second hydrogenation of CRAL in Pathway F is 0.96 eV and the desorption energy of butanal from the surface is 0.89 eV. These results suggest that of the butanal formation pathways examined, Pathway F is the most favorable because of the lower hydrogenation barriers. A more in-depth comparison between butanal formation via Pathway F and CROL formation via Pathway A is discussed in the next section.

6.4.6 Comparing butanal and CROL formation over BTOH. The energy profile of Pathway F is shown in Figure 6.9a along with Pathway A as a comparison. The key intermediate structures of Pathway F are shown in Figure 6.9b. In Pathway F, the barriers corresponding to the first and second hydrogenation of CRAL are both larger than in Pathway A. Accordingly, we can conclude from these results that Pathway A is the overall most favorable pathway out of all pathways considered (A-H) and CROL would be the expected major product to form over the BTOH(211)-Ba_2O_4H surface termination. Although relatively high CROL and butanal desorption energies are required (i.e., 1.33 eV and 0.89 eV, respectively), the free energy of CROL and butanal desorption is much lower

at 0.67 eV and 0.19 eV, respectively. This value was calculated after adding the favorable entropy contribution due to the formation of a gaseous CROL or butanal molecule (state 7) at the reaction temperature.

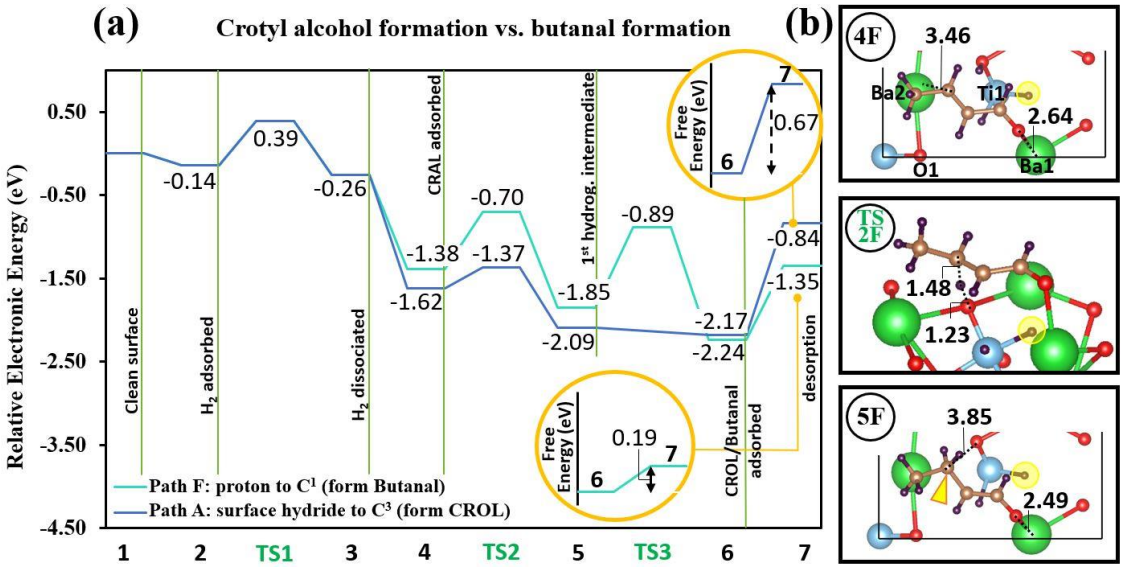

Figure 6.9 (a) Energy profiles of the most favorable pathways for CROL formation (Pathway A, blue line) and butanal formation (Pathway F, turquoise line). (b) The key intermediate structures of Pathway F. For reference, the lattice hydride is highlighted in yellow and the atom in CRAL being hydrogenated is indicated by the yellow-orange arrow in Figure 6.9b. All atomic distances are reported in units of Å. The free energy of desorption of CROL is shown in the orange bubble.

To understand why the first hydrogenation barrier in Pathway A is lower than in Pathway F, we again look into the Bader charges of certain atoms in states 4A and 4F as shown in Figure 6.10. Recall in section 6.4.4, we found that the first hydrogenation of CRAL in Pathway A involves the favorable bond formation between a negatively charged surface hydride and positively charged C^3. Likewise, the first hydrogenation of CRAL in Pathway F also involves the favorable bond formation between oppositely charged species.

However, this time it is between the positively charged proton (+0.57 |e|) and negatively charged C^1 (-0.18 |e|). Even though the H species in state 4A (or 4F) interact favorably with C^3 (or C^1), the first hydrogenation barrier is still lower in Pathway A than in Pathway F.

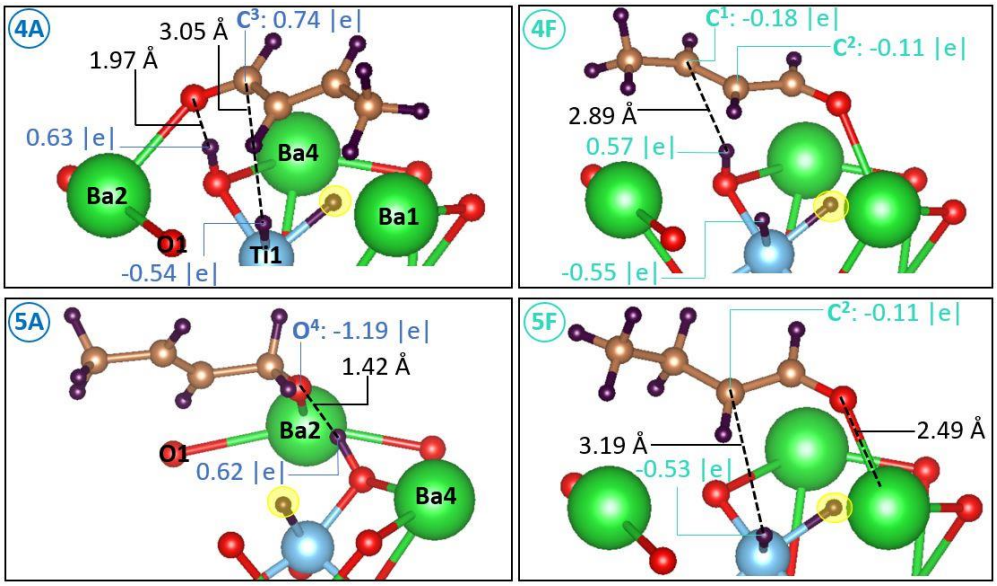

Figure 6.10 The Bader charges and atomic distances in state 4 and 5 of pathways A and F. The lattice hydride is highlighted in yellow, and all atomic distances are reported in units of Å.

This may be due to the magnitude of charge for C^1 being less than that of C^3 which leads to a weaker interaction between the proton and C^1 in Pathway F than between the surface hydride and C^3 interaction in Pathway A. In the second hydrogenation, the favorable interaction between the proton (+0.62 |e|) and O^4 atom (-1.19 |e|) as well as the relatively shorter distance between the proton and O^4 in state 5A of Figure 6.10 explains why the second hydrogenation in Pathway A is so favorable. In Pathway F, the second hydrogenation barrier is much higher at 0.96 eV because of the unfavorable interaction

between the surface hydride (-0.53 |e|) and the C^2 atom (-0.11 |e|). Thus, Bader charges on the surface atoms and substrate may play an important role in determining product selectivity.

6.4.7 Experimental implications. The selective hydrogenation of α,β-unsaturated aldehydes can occur either in the gas[39,40,41,42] or liquid[43,44,45,46] phase. Common solvents used for liquid-phase hydrogenation include ethanol, isopropyl alcohol, water, an alcohol-water mixture, and others. Typically, solvent is used to dissolve reactants and keep products in solution, however, it has also been shown to influence reaction activity and selectivity. For example, in the reaction to form the hydroxybutyl intermediate from 2-butanone hydrogenation, DFT results show that water molecules can hydrogen bond with the transition state's hydrogen and oxygen atoms.[47] Hence, the transition state becomes stabilized, and the activation barrier decreases from 0.66 eV in the gas phase to 0.21 eV in the liquid phase. In other studies, protic solvent molecules are shown to assist in H_2 dissociation.[48,49]

Currently, there have been no experimental work on the selective hydrogenation of CRAL over BTOH in the liquid phase. Therefore, the goal of this study is to understand the gas-phase reaction mechanism over BTOH to provide general insights on how the reactant, intermediate, and product molecules interact with the catalytic surface. Future experimental investigations would be necessary in order to determine an optimal solvent for selectivity to the CROL product. From there, further DFT calculations can help understand the potential solvent effects in the reaction over BTOH. It would be intriguing to see how the solvent interacts with surface atoms, specifically the lattice hydride.

6.5 Conclusion

In this work, first principles density functional theory was used to investigate the selective hydrogenation of crotonaldehyde (CRAL) on the BTOH(211)-Ba_2O_4H surface termination via the Horiuti-Polanyi mechanism. Given that CRAL has two types of double bonds, C=O and C=C, it can be hydrogenated to form either crotyl alcohol (CROL) or butanal, respectively. Furthermore, after heterolytic cleavage of H_2 over a surface hydride vacancy and O atom, there are two relevant adsorption configurations of CRAL on the hydrogenated surface that were considered. In the CRAL_adsorption_1 configuration, the C=O bond of CRAL is in close proximity with dissociated H_2 whereas in CRAL_adsorption_2, the C=C bond is closer. Using DFT, possible minimum-energy pathways for CROL and butanal formation have been identified from these CRAL adsorption configurations. It was determined that CROL formation starting from the CRAL_adsorption_1 configuration is the overall most favorable pathway studied and, therefore, CROL would be the expected major product to form over the BTOH(211)-Ba_2O_4H surface termination. This is because the surface vacancies provide an avenue for H_2 heterolytic cleavage to form a proton and surface hydride which are conducive for CROL formation due to the favorable charge interactions between the surface hydride and partially positive carbonyl carbon in CRAL as well as between the proton and O atom in CRAL. The charge interactions between the H species and carbon atoms in CRAL's C=C bond are not as favorable and, thus, butanal formation is not as preferred. Although, the selective hydrogenation of CRAL is commonly done in the liquid phase, in this work, we first investigate the gas-phase reaction mechanism over BTOH to understand how reactant,

intermediate, and product molecules of CRAL selective hydrogenation interact with the catalytic surface. Our findings provide insights on the role BTOH lattice hydrides and surface hydride vacancies play in general selective hydrogenation of α,β-unsaturated aldehydes.

6.6 References

(1) Kobayashi, Y.; Hernandez, O. J.; Sakaguchi, T.; Yajima, T.; Roisnel, T.; Tsujimoto, Y.; Morita, M.; Noda, Y.; Mogami, Y.; Kitada, A.; Ohkura, M.; Hosokawa, S.; Li, Z.; Hayashi, K.; Kusano, Y.; Kim, J.; Tsuji, N.; Fujiwara, A.; Matsushita, Y.; Yoshimura, K.; Takegoshi, K.; Inoue, M.; Takano, M.; Kageyama, H. An oxyhydride of $BaTiO_3$ exhibiting hydride exchange and electronic conductivity. *Nat. Mater.* **2012**, 11, 507-511.

(2) Tang, Y.; Kobayashi, Y.; Shitara, K.; Konishi, A.; Kuwabara, A.; Nakashima, T.; Tassel, C.; Yamamoto, T.; Kageyama, H. On Hydride Diffusion in Transition Metal Perovskite Oxyhydrides Investigated via Deuterium Exchange. *Chem. Mater.* **2017**, 29, 8187-8194.

(3) Sakaguchi, T.; Kobayashi, Y.; Yajima, T.; Ohkura, M.; Tassel, C.; Takeiri, F.; Mitsuoka, S.; Ohkubo, H.; Yamamoto, T.; Kim, J.; Tsuji, N.; Fujihara, A.; Matsushita, Y.; Hester, J.; Avdeev, M.; Ohoyama, K.; Kageyama, H. Oxyhydrides of $(Ca,Sr,Ba)TiO_3$ Perovskite Solid Solutions. *Inorg. Chem.* **2012**, 51, 11371-11376.

(4) Tang, Y.; Kobayashi, Y.; Tassel, C.; Yamamoto, T.; Kageyama, H. Hydride-Enhanced CO_2 Methanation: Water-Stable $BaTiO_{2.4}H_{0.6}$ as a New Support. *Adv. Energy Mater.* **2018**, 8, 1800800.

(5) Tang, Y.; Kobayashi, Y.; Masuda, N.; Uchida, Y.; Okamoto, H.; Kageyama, T.; Hosokawa, S.; Loyer, F.; Mitsuhara, K.; Yamanaka, K.; Tamenori, Y.; Tassel, C.; Yamamoto, T.; Tanaka, T.; Kageyama, H. Metal-Dependent Support Effects of Oxyhydride-Supported Ru, Fe, Co Catalysts for Ammonia Synthesis. *Adv. Energy Mater.* **2018**, 8, 1801772.

(6) Kobayashi, Y.; Tang, Y.; Kageyama, T.; Yamashita, H.; Masuda, N.; Hosokawa, S.; Kageyama, H. Titanium-Based Hydrides as Heterogeneous Catalysts for Ammonia Synthesis. *J. Am. Chem. Soc.* **2017**, 139, 18240-18246.

(7) Wang, K.; Wu, Z.; Jiang, D. Ammonia synthesis on $BaTiO_{2.5}H_{0.5}$: computational insights into the role of hydrides. *Phys. Chem. Chem. Phys.* **2022**, 24, 1496-1502.

(8) Smith, M. B.; March, J. *March's advanced organic chemistry: reactions, mechanisms, and structure;* John Wiley & Sons, 2007.

(9) Augustine, R. L. *Catalytic Hydrogenation: Techniques and Applications in Organic Synthesis;* Marcel Dekker, Inc., 1965.
(10) Gallezot, P.; Richard, D. Selective Hydrogenation of α,β-Unsaturated Aldehydes. *Catal. Rev.: Sci. Eng.* **1998**, 40, 81-126.
(11) Mäki-Arvela, P.; Hájek, J.; Salmi, T.; Murzin, D. Y. Chemoselective Hydrogenation of Carbonyl Compounds over Heterogeneous Catalysts. *Appl. Catal., A* **2005**, 292, 1-49.
(12) Mohr, C.; Claus, P. Hydrogenation properties of supported nanosized gold particles. *Sci. Prog.* **2001**, 84, 311-334.
(13) Meyer, G. R. Conjugate and Nonconjugate Reduction with $LiAlH_4$ and $NaBH_4$. *J. Chem. Educ.* **1981**, 58, 628-630.
(14) Siddqui, N.; Sarkar, B.; Pendem, C.; Khatun, R.; Sivakumar Konthala, L. N.; Sasaki, T.; Bordoloi, A.; Bal, R. Highly selective transfer hydrogenation of α,β-unsaturated carbonyl compounds using Cu-based nanocatalysts. *Catal. Sci. Technol.* **2017**, 7, 2828-2837.
(15) Lan, X.; Wang, T. Highly Selective Catalysts for the Hydrogenation of Unsaturated Aldehydes: A Review. *ACS Catal.* **2020**, 10, 2764-2790.
(16) Wang, H.; Bai, S.; Pi, Y.; Shao, Q.; Tan, Y.; Huang, X. A Strongly Coupled Ultrasmall Pt_3Co Nanoparticle-Ultrathin $Co(OH)_2$ Nanosheet Architecture Enhances Selective Hydrogenation of α,β-Unsaturated Aldehydes. *ACS Catal.* **2019**, 9, 154-159.
(17) Kennedy, G.; Baker, L. R.; Somorjai, G. A. Selective Amplification of C=O Bond Hydrogenation on Pt/TiO_2: Catalytic Reaction and Sum-Frequency Generation Vibrational Spectroscopy Studies of Crotonaldehyde Hydrogenation. *Angew. Chem.* **2014**, 126, 3473-3476.
(18) Lou, Y.; Zheng, Y.; Li, X.; Ta, N.; Xu, J.; Nie, Y.; Cho, K.; Liu, J. Pocketlike Active Site of Rh_1/MoS_2 Single-Atom Catalyst for Selective Crotonaldehyde Hydrogenation. *J. Am. Chem. Soc.* **2019**, 141, 19289-19295.
(19) Bhogeswararao, S.; Pavan Kumar, V.; Chary, K. V. R.; Srinivas, D. Noble Metal Promoted CeO2-ZrO2-Supported Ni Catalysts for LiquidPhase Hydrogenation of Cinnamaldehyde. Catal. Lett. **2013**, 143, 1266−1276.
(20) Zhang, Y.; Zhang, S.; Pan, X.; Bao, M.; Huang, J.; Shen, W. Selective Hydrogenation of Cinnamaldehyde to Cinnamyl Alcohol over Au Catalysts: Influence of the Oxide-Supports. Catal. Lett. **2017**, 147, 102−109.
(21) Milone, C.; Ingoglia, R.; Schipilliti, L.; Crisafulli, C.; Neri, G.; Galvagno, S. Selective hydrogenation of α,β-unsaturated ketone to α,β-unsaturated alcohol on gold-supported iron oxide catalysts: Role of the support. *J. Catal.* **2005**, 236, 80-90.
(22) Xin, H.; Xue, Y.; Zhang, W.; Wu, P.; Li, X. CoxFe1-xAl2O4+δ Composite Oxides Supported Pt Nanoparticles as Efficient and Recyclable Catalysts for the Liquid-Phase Selective Hydrogenation of Cinnamaldehyde. J. Catal. **2019**, 380, 254−266.
(23) Zhang, Z.; Wang, Z.-Q.; Li, Z.; Zheng, W.-B.; Fan, L.; Zhang, J.; Hu, Y.-M.; Luo, M.-F.; Wu, X.-P.; Gong, X.-Q.; Huang, W.; Lu, J.-Q. Metal-Free Ceria Catalysis

for Selective Hydrogenation of Crotonaldehyde. *ACS. Catal.* **2020**, 10, 14560-14566.
(24) Wang, K.; Fung, V.; Wu, Z.; Jiang, D.-E. Stable Surface Terminations of a Perovskite Oxyhydride from First Principles. *J. Phys. Chem. C* **2020**, 124, 18557-18563.
(25) Kresse, G.; Furthmüller, J. Efficiency of ab-initio total energy calculations for metals and semiconductors using a plane-wave basis set. *Comput. Mater. Sci.* **1996**, 6, 15-50.
(26) Kresse, G.; Furthmüller, J. Efficient Iterative Schemes for Ab Initio Total-Energy Calculations Using a Plane-Wave Basis Set. *Phys. Rev. B: Condens. Matter Mater. Phys.* **1996**, 54, 11169-11186.
(27) Perdew, J. P.; Burke, K.; Ernzerhof, M. Generalized Gradient Approximation Made Simple. *Phys. Rev. Lett.* **1996**, 77, 3865.
(28) Blöchl, P. E. Projector Augmented-Wave Method. *Phys. Rev. B: Condens. Matter Mater. Phys.* **1994**, 50, 17953-17979.
(29) Grimme, S.; Antony, J.; Ehrlich, S.; Krieg, H. A consistent and accurate *ab initio* parametrization of density functional dispersion correction (DFT-D) for the 94 elements H-Pu. *J. Chem. Phys.* **2010**, 132, 154104.
(30) Tang, W.; Sanville, E.; Henkelman, G. A grid-based Bader analysis algorithm without lattice bias. *J. Phys.: Condens. Matter* **2009**, 21, 084204.
(31) Monkhorst, H. J.; Pack, J. D. Special points for Brillouin-zone integrations. *Phys. Rev. B: Solid State* **1976**, 13, 5188-5192.
(32) Neugebauer, J.; Scheffler, M. Adsorbate-substrate and adsorbate-adsorbate interactions of Na and K adlayers on Al(111). *Phys. Rev. B* **1992**, 46, 16067-16080.
(33) Henkelman, G.; Jónsson, H. Improved tangent estimate in the nudged elastic band method for finding minimum energy paths and saddle points. *J. Chem. Phys.* **2000**, 113, 9978-9985.
(34) Henkelman, G.; Jónsson, H. A dimer method for finding saddle points on high dimensional potential surfaces using only first derivatives. *J. Chem. Phys.* **1999**, 111, 7010-7022.
(35) Savara, A. Standard States for Adsorption on Solid Surfaces: 2D Gases, Surface Liquids, and Langmuir Adsorbates. *J. Phys. Chem. C* **2013**, 117, 15710 – 15715.
(36) García-Melchor, M.; López, N. Homolytic Products from Heterolytic Paths in H_2 Dissociation on Metal Oxides: The Example of CeO_2. *J. Phys. Chem. C* **2014**, 118, 10921-10926.
(37) Hu, G.; Wu, Z.; Jiang, D.E. First Principles Insight into H_2 Activation and Hydride Species on TiO_2 Surfaces. *J. Phys. Chem. C* **2018**, 122, 20323-20328.
(38) Horiuti, J.; Polanyi, M. Exchange reactions of hydrogen on metallic catalysts. *Trans. Faraday Soc.* **1934**, 163, 1164.
(39) Gebauerhenke, E.; Grams, J.; Szubiakiewicz, E.; Farbotko, J.; Touroude, R.; Rynkowski, J. Pt/Ga2O3 Catalysts of Selective Hydrogenation of Crotonaldehyde. J. Catal. 2007, 250, 195−208.

(40) Yuan, J.-F.; Luo, C.-Q.; Yu, Q.; Jia, A.-P.; Hu, G.-S.; Lu, J.-Q.; Luo, M.-F. Great Improvement on the Selective Hydrogenation of Crotonaldehyde over CrOx- and FeOx-promoted Ir/SiO2 Catalysts. Catal. Sci. Technol. 2016, 6, 4294−4305.
(41) Ruiz-Martínez, J.; Fukui, Y.; Komatsu, T.; Sepúlveda-Escribano, A. Ru−Ti Intermetallic Catalysts for the Selective Hydrogenation of Crotonaldehyde. J. Catal. 2008, 260, 150−156.
(42) Concepción, P.; Corma, A.; Silvestre-Albero, J. CeO2-doped Nanostructured Materials as a Support of Pt Catalysts: Chemoselective Hydrogenation of Crotonaldehyde. Top. Catal. 2007, 46, 31−38.
(43) Li, Y.; Zhou, R. X.; Lai, G. H. Effect of Transition Metals (Cr, Mn, Fe, Co, Ni and Cu) on selective Hydrogenation of Cinnamaldehyde over Pt/CNTs Catalyst. React. Kinet. Catal. Lett. 2006, 88, 105−110.
(44) Bhogeswararao, S.; Srinivas, D. Intramolecular Selective Hydrogenation of Cinnamaldehyde over CeO2−ZrO2-supported Pt Catalysts. J. Catal. 2012, 285, 31−40.
(45) Zheng, R.; Porosoff, M. D.; Weiner, J. L.; Lu, S.; Zhu, Y.; Chen, J. G. Controlling Hydrogenation of C=O and C=C bonds in Cinnamaldehyde using Silica Supported Co-Pt and Cu-Pt Bimetallic Catalysts. Appl. Catal., A 2012, 419−420, 126−132.
(46) Tamura, M.; Tokonami, K.; Nakagawa, Y.; Tomishige, K. Selective Hydrogenation of Crotonaldehyde to Crotyl Alcohol over Metal Oxide Modified Ir Catalysts and Mechanistic Insight. ACS Catal. 2016, 6, 3600−3609.
(47) Akpa, B. S.; D'Agostino, C.; Gladden, L. F.; Hindle, K.; Manyar, H.; McGregor, J.; Li, R.; Neurock, M.; Sinha, N.; Stitt, E. H.; Weber, D.; Zeitler, J. A.; Rooney, D. W. Solvent effects in the hydrogenation of 2-butanone. *J. Catal.* **2012**, 289, 30-41.
(48) Manyar, H. G.; Yang, B.; Daly, H.; Moor, H.; McMonagle, S.; Tao, Y.; Yadav, G. D.; Goguet, A.; Hu, P.; Hardacre, C. Selective Hydrogenation of α,β-Unsaturated Aldehydes and Ketones using Novel Manganese Oxide and Platinum Supported on Manganese Oxide Octahedral Molecular Sieves as Catalysts. *Chem. Cat. Chem.* **2013**, 5, 506-512.
(49) Ouyang, R.; Jiang, D. Understanding Selective Hydrogenation of α,β-Unsaturated Ketones to Unsaturated Alcohols on the $Au_{25}(SR)_{18}$ Cluster. *ACS Catal.* **2015**, 5, 6624-6629.

6.7 Appendix

6.A1 CROL formation from CRAL_adsorption_2

In the main text, we only discuss CROL formation starting from CRAL_adsorption_1 because the C=O bond of CRAL is already aligned and in close

proximity to dissociated H_2 in this orientation. Here, we also explored a CROL formation pathway from CRAL_adsorption_2. From our NEB calculations in Figure 6.A1, we show that the surface hydride addition to the CRAL carbonyl carbon, C^3, requires an energy barrier of only 0.12 eV, which is 0.13 eV lower than the first hydrogenation barrier in Pathway A. Then, to test the mobility of the resulting intermediate over the catalytic surface, an *ab initio* molecular dynamics (AIMD) simulation was performed in canonical ensemble (NVT) with Nosé-Hoover thermostat at 500 K for 1.5 ps with a timestep of 0.5 fs. Figure 6.A2 shows the structure of the system before the AIMD simulation, after 0.5 ps, and CROL formation in the final structure after a total AIMD simulation run of 1.5 ps. Our AIMD calculations show that the intermediate and surface atoms must shift and migrate until the intermediate's O atom is in close enough proximity to dissociated H_2 for H addition. Investigating different possible migration pathways of CRAL or its corresponding hydrogenated intermediate over the surface would be important when finding the most favorable pathway for CRAL hydrogenation. However, in this work, we are most interested in comparing the energy barriers of C=C and C=O hydrogenation to determine product selectivity over BTOH. Therefore, we only explored CROL formation pathways from the CRAL_adsorption_1 orientation and butanal formation pathways from CRAL_adsorption_2.

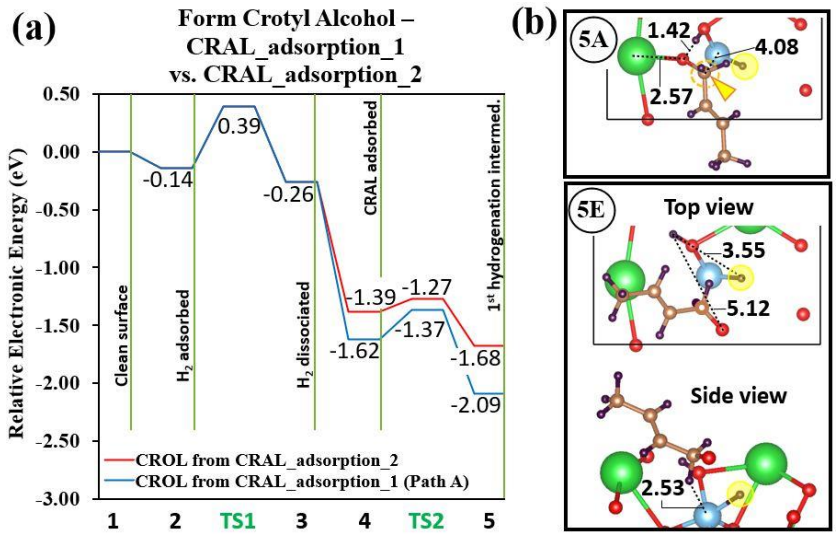

Figure 6.A1 Energy profiles of CROL formation from CRAL adsorbed in the CRAL_adsorption_1 (blue line) and CRAL_adsorption_2 (red line) orientation (a) and the corresponding state 5 structures (b). For reference, the lattice hydride is highlighted in yellow and the atom in CRAL being hydrogenated is indicated by the yellow-orange arrow in Figure S1b. All atomic distances are reported in units of Å.

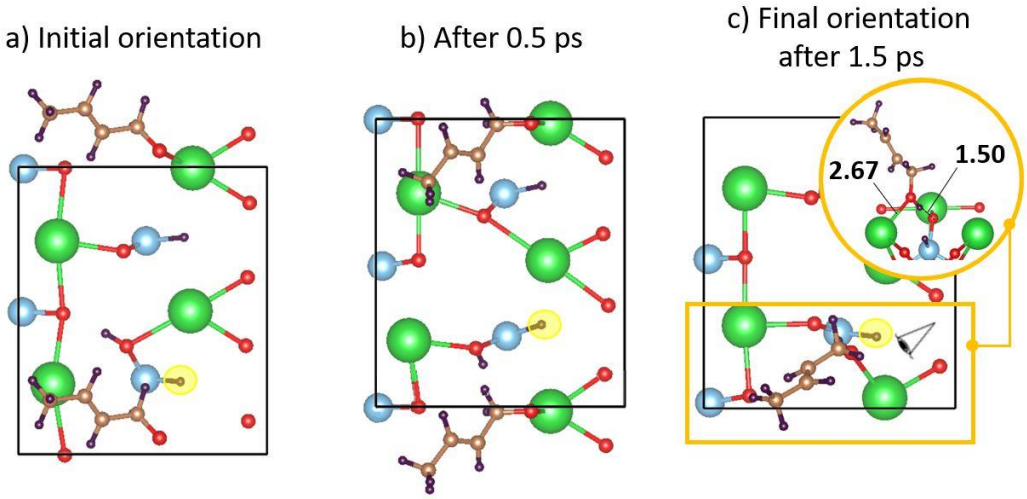

Figure 6.A2 The structure of the system before the AIMD simulation (a), after 0.5 ps (b), and CROL formation in the final structure after a total AIMD simulation run of 1.5 ps (c). For reference, the lattice hydride is highlighted in yellow. All atomic distances are reported in units of Å.

CHAPTER 7
Conclusions and future outlooks

7.1 Conclusions

Recently, the $BaTiO_{3-x}H_x$ perovskite oxyhydride has shown to be more active and a more effective catalyst support in hydrogenation reactions than its parent oxide, $BaTiO_3$.[1,2,3] Hence, in this thesis, we aimed to explore the role of $BaTiO_{2.5}H_{0.5}$ (BTOH) lattice hydrides in hydrogenation reactions including ammonia synthesis, acetylene semi-hydrogenation, and crotonaldehyde selective hydrogenation. Because a catalyst's activity and selectivity properties are dependent on its surface structure,[4] in Chapter 3, we aimed to identify stable terminations of BTOH that are the most probable to form under the typical reaction conditions of the above hydrogenation reactions.[5] We compared the surface grand potentials of 47 different $BaTiO_{2.5}H_{0.5}$ (BTOH) terminations belonging to five different facets: (100), (010), (210), (011), and (211). We then constructed surface phase diagrams at catalytically relevant temperature and pressure conditions (300 – 700 K, $10^{-15} \leq P_{O2} \leq 1$ atm, $10^{-15} \leq P_{H2} \leq 100$ atm). The diagrams showed that the (010)-Ba_2O_2, (210)-Ti_2O_2, and (211)-Ba_2O_4H are the most stable BTOH surface terminations at 700 and 500 K. Only the (010)-Ba_2O_2 and (211)-Ba_2O_4H are the most stable at 300 K. The importance of our first work is to lay a foundation to further explore surface chemistry and catalysis on the surfaces of the $BaTiO_{2.5}H_{0.5}$ perovskite oxyhydride.

In Chapter 4, we began our investigation of the role BTOH lattice hydrides play in hydrogenation reactions, specifically in the synthesis of ammonia.[6] From the phase diagrams constructed in Chapter 3, we can see that the (210)-Ti_2O_2 surface termination of

BTOH is the most stable under ammonia synthesis conditions.[5] This surface is vicinal in structure and exposes subsurface hydride which can potentially be important in the hydrogenation reaction. Our results showed that N_2 prefers to adsorb on the more reduced surface Ti atom, which is bonded to a subsurface lattice hydride, while heterolytically dissociative H_2 adsorption is also facile on the surface. In order to understand the BTOH surface chemistry in ammonia synthesis, two pathways for the hydrogenation of adsorbed N_2 have been examined: the distal and alternating pathways. In the distal pathway, the subsurface hydride vacancy from reaction of $*N_2$ with the lattice hydride was found to be key to breaking the $*N–NH_3$ bond and leading to surface nitride formation. In the alternating pathway, the neighboring surface Ti sites are key to bridging and stabilizing the *NNH intermediate. Overall, the alternating pathway is a more favorable pathway, especially when lattice hydrides are abundant on the surface. Chapter 4 sheds light on the role of surface lattice hydrides and their vacancies in hydrogenation of N_2 over BTOH and was useful in understanding other hydrogenation reactions over BTOH as seen in Chapters 5 and 6.

In Chapter 5, we continued our investigation of the role BTOH lattice hydrides play in alkyne semi-hydrogenation reactions. Specifically, we studied acetylene semi-hydrogenation over BTOH as a probe reaction. From the phase diagrams constructed in Chapter 3, we can see that the (211)-Ba_2O_4H surface termination of BTOH is the most stable under acetylene semi-hydrogenation conditions.[5] This surface is flat in structure and exposes surface hydride and vacancies which can potentially be active in hydrogenation reactions. In acetylene semi-hydrogenation, the desired product is the semi-hydrogenated

product (i.e., ethylene), rather than the fully hydrogenated product (i.e., ethane). Our results showed that of the Horiuti-Polanyi and lattice hydride mechanisms considered, the former mechanism was shown to form ethylene and ethane at a faster rate than the latter according to microkinetic modeling based on the DFT energies and barriers. Furthermore, the microkinetic simulations show that the rate of ethylene formation via the Horiuti-Polanyi mechanism is faster than ethane formation by one order of magnitude at a temperature of 523 K. Therefore, it is suggested that BTOH can selectively hydrogenate acetylene to ethylene with a high selectivity under the specified conditions. A reason behind this selectivity may be due to the presence of lattice hydrides in BTOH which favors a surface containing vacancies under the given reaction conditions. In turn, these surface vacancies are important in the facile heterolytic cleavage of H_2 over BTOH as a means to provide active H species for hydrogenation in the Horiuti-Polanyi mechanism. Additionally, the surface anion vacancies are crucial to stabilizing the vinyl intermediate and, therefore, drive the reaction selectivity towards ethylene. The findings from this work provided a deeper understanding on the role of lattice hydrides and surface anion vacancies in the BTOH catalyst for acetylene semi-hydrogenation selectivity and suggest the potential use of BTOH as catalysts for general alkyne semi-hydrogenation.

Lastly in Chapter 6, we investigated the role of BTOH lattice hydrides in the selective hydrogenation of crotonaldehyde (CRAL) to gain an understanding of the BTOH surface chemistry for the selective hydrogenation of α,β-unsaturated aldehydes. From the phase diagrams constructed in Chapter 3, we can see that the (211)-Ba_2O_4H surface termination of BTOH is also the most stable under the conditions for selective

hydrogenation of crotonaldehyde.[5] Our findings showed that the surface vacancies provide an avenue for H_2 heterolytic cleavage to form a proton and surface hydride which are conducive for CROL formation due to the favorable charge interactions between the surface hydride and partially positive carbonyl carbon in CRAL as well as between the proton and O atom in CRAL. The charge interactions between the H species and carbon atoms in CRAL's C=C bond are not as favorable and, thus, butanal formation is not as preferred. Our findings from this work further add on to our working knowledge of the BTOH structure-selectivity relationship towards hydrogenation reactions.

7.2 Future directions

In this thesis, we merely scratched the surface on the surface chemistry of $BaTiO_{2.5}H_{0.5}$ (BTOH). There is still more work to be done in order to have a more comprehensive understanding of the $BaTiO_{3-x}H_x$ material as a whole.

First off, as mentioned previously, a catalyst's activity and selectivity properties are dependent on its surface structure.[4] Surfaces are cleaved from a bulk crystal structure of a particular morphology. Therefore, a different $BaTiO_{3-x}H_x$ bulk morphology can lead to different surfaces and configurations of exposed atoms. Given that the $BaTiO_3$ bulk varies in crystalline structures depending on the external temperature,[10] it would be crucial to identify the equilibrium crystal shape of $BaTiO_{3-x}H_x$ by applying the Gibbs-Wulff theorem.[11]

Second, it would be interesting to compare the surface chemistry of a $BaTiO_{3-x}H_x$ surface cleaved from different bulk morphology. A recent study showed that hexagonal $BaTiO_{3-x}H_x$ can be synthesized from the reaction of BaH_2 with TiO_2 at 800°C.[12] Besides

structure, what makes the hexagonal form of $BaTiO_{3-x}H_x$ different than the cubic form is that hexagonal $BaTiO_{3-x}H_x$ can hold a higher hydride content (i.e. $x \approx 1$) than its cubic form ($x \leq 0.60$). Catalytic studies have shown that Pd loaded on hexagonal $BaTiO_{3-x}H_x$ has a higher turnover frequency in the semi-hydrogenation of Phenylacetylene than when Pd is loaded on cubic $BaTiO_{3-x}H_x$. This could be due to the fact that hexagonal $BaTiO_{3-x}H_x$ contains a higher hydride content than cubic $BaTiO_{3-x}H_x$. It would then be beneficial to test the $BaTiO_{3-x}H_x$ activity at a constant hydride content but with surfaces cleaved from varying bulk crystal morphology to further understand $BaTiO_{3-x}H_x$ structure-activity relationship.

Third, there have been a couple reports that discuss the effectiveness of cubic $BaTiO_{3-x}H_x$ as a metal catalyst support for hydrogenation reactions including CO_2 methanation and ammonia synthesis.[2,3] The metal catalysts studied included Ni and Ru for CO_2 methanation and Ru, Fe, and Co for ammonia synthesis. However, no theoretical investigations have been performed to determine the optimal metal catalyst for a specific hydrogenation reaction. It would particularly be interesting to investigate the compatibility of $BaTiO_{3-x}H_x$ as a single atom catalyst (SAC) support since SACs have lately become of interest due to its enhanced performance in industrially important reactions and decrease in precious metal usage.[7-9]

Pursuing these future directions only marks the beginning of understanding the catalytic potential of anion-tuned metal oxides, such as $BaTiO_{3-x}H_x$, for hydrogenation reactions. Currently, experimental studies on $BaTiO_{3-x}H_x$ in catalytic reactions are lacking. However, these studies are warranted in order to verify future computational results

regarding the surface structure and activity of these materials. There is so much to be learned about these materials and only time will tell the impact these materials will have in our society.

7.3 References

(1) Kobayashi, Y.; Tang, Y.; Kageyama, T.; Yamashita, H.; Masuda, N.; Hosokawa, S.; Kageyama, H. Titanium-Based Hydrides as Heterogeneous Catalysts for Ammonia Synthesis. *J. Am. Chem. Soc.* **2017**, 139, 18240-18246.

(2) Tang, Y.; Kobayashi, Y.; Masuda, N.; Uchida, Y.; Okamoto, H.; Kageyama, T.; Hosokawa, S.; Loyer, F.; Mitsuhara, K.; Yamanaka, K.; Tamenori, Y.; Tassel, C.; Yamamoto, T.; Tanaka, T.; Kageyama, H. Metal-Dependent Support Effects of Oxyhydride-Supported Ru, Fe, Co Catalysts for Ammonia Synthesis. *Adv. Energy Mater.* **2018**, 8, 1801772.

(3) Tang, Y.; Kobayashi, Y.; Tassel, C.; Yamamoto, T.; Kageyama, H. Hydride-Enhanced CO_2 Methanation: Water-Stable $BaTiO_{2.4}H_{0.6}$ as a New Support. *Adv. Energy Mater.* **2018**, 8, 1800800.

(4) Chee, Z. W.; Arce-Ramos, J. M.; Li, W.; Genest, A.; Mirsaidov, U. Structural changes in noble metal nanoparticles during CO oxidation and their impact on catalyst activity. *Nat. Commun.* **2020**, 11, 2133.

(5) Wang, K.; Fung, V.; Wu, Z.; Jiang, D.-E. Stable Surface Terminations of a Perovskite Oxyhydride from First-Principles. *J. Phys. Chem. C*, **2020**, 124, 18557–18563.

(6) Wang, K.; Wu, Z.; Jiang, D.-E. Ammonia synthesis on $BaTiO_{2.5}H_{0.5}$:computational insights into the role of hydrides. *Phys. Chem. Chem. Phys.* **2022**, 24, 1496-1502.

(7) Wang, A.; Li, J.; Zhang, T. Heterogeneous single-atom catalysis. *Nat. Rev. Chem.* **2018**, 2, 65-81.

(8) Liu, J. Catalysis by Supported Single Metal Atoms. *ACS Catal.* **2017**, 7, 34-59.

(9) Cheng, N.; Zhang, L.; Doyle-Davis, K.; Sun, X. Single-Atom Catalysts: From Design to Application. *EER* **2019**, 2, 539-573.

(10) Lacerda, L. H. S.; Ribeiro, R. A. P.; de Andrade, A. M.; de Lazaro, S. R. Zn-doped $BaTiO_3$ Materials: A DFT Investigation for Optoelectronic and Ferroelectric Properties Improvement. *Revista Processos Quimicos*. **2015**, 18, 274-280.

(11) Kim, J.-S.; Kim, Y.-C. Equilibrium crystal shape of $BaZrO_3$ and space charge formation in the (011) surface by using *ab-initio* thermodynamics. *J Korean Phys Soc* **2017**, 70, 75-80.

(12) Miyazaki, M.; Ogasawara, K.; Nakao, T.; Sasase, M.; Kitano, M.; Hosono, H. Hexagonal $BaTiO_{(3-x)}H_x$ Oxyhydride as a Water-Durable Catalyst Support for Chemoselective Hydrogenation. *J. Am. Chem. Soc.* **2022**, 144, 6453-6464.